



Instituto Universitario de Investigación
en Ingeniería de Aragón
Universidad Zaragoza

Ph.D. Thesis

Intracardiac Signal Processing for Mapping and Characterising Cardiac Arrhythmias

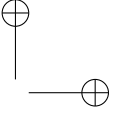
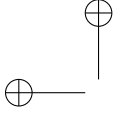
Procesado de Señal Intracardiaca para el
Mapeo y Caracterización de Arritmias Cardíacas

Alejandro Alcaine Otín

SUPERVISORS:
Juan Pablo Martínez Cortés
Pablo Laguna Lasaosa

Ph.D. in Biomedical Engineering

Zaragoza, December 2016

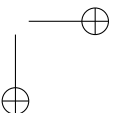
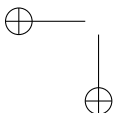


Alejandro Alcaine Otín, 2016
Intracardiac Signal Processing for Mapping and Characterising Cardiac Arrhythmias

Date of current version: Thursday 24th November, 2016

This thesis was supported by a F.P.I. grant from Ministerio de Economía y Competitividad (MINECO, Spain) Ref.: BES-2011-046644. The research stays were also supported by MINECO (Spain) Refs.: EEBB-I-13-06613, EEBB-I-14-08406 and EEBB-I-15-09466. The research presented in this thesis was also supported by projects: TEC2010-21703-C03-02 (MINECO and FEDER) and TEC2013-42140-R (MINECO). Also by Aragón Government (Spain) and European Social Found (Europe) through Grupo Consolidado BSICoS Ref.: T96 and by Centro de Investigación Biomédica en Red de Bioingeniería, Biomateriales y Nanomedicina (CIBER-BBN) through Instituto de Salud Carlos III. The computations of some parts of this thesis were performed by the ICTS “NANBIOSIS”, more specifically by the High Performance Computing Unit of the CIBER-BBN at the University of Zaragoza.

This thesis was printed thanks to the financial support of BSICoS Group at University of Zaragoza.





Abstract

Cardiovascular diseases are the principal cause of death worldwide, especially in the US and Europe. Some of these diseases manifest as arrhythmic events, i.e., alterations of the normal sinus rhythm of the heart.

Arrhythmia treatment varies depending on the type of arrhythmia and patient characteristics. Anti-arrhythmic drug therapy is often the first choice for arrhythmia management, although catheter ablation is becoming a first line therapy specially in those cases when the disease is on its first states, anti-arrhythmic drug therapy is ineffective or the arrhythmia focus is identifiable. Catheter ablation is a minimally invasive clinical procedure that deploys small catheters in the cardiac chambers. Those catheters are equipped with electrodes that sense the local electrical activity of the heart, known as electrograms (EGM), during arrhythmia or sinus rhythm. Based on the characteristics of this electrical activity, radio frequency energy is delivered at those sites responsible of the clinical arrhythmia.

The aim of this thesis is to investigate signal processing techniques of invasive EGM signals in order to provide useful tools for helping in the decision process during ablation procedures and electrophysiological studies.

In chapter 2, an automatic EGM delineator based on the wavelet transform of the bipolar electrogram (b-EGM) signal envelope is introduced and validated. It is motivated by the need of an operator-independent algorithm to measure local activation times (LATs) and to build ventricular activation maps in electroanatomical mapping (EAM) systems. The accuracy of the method is first validated against manual annotations performed by two experts, showing errors in the same order as the annotations performed manually during the interventions in the electrophysiology lab. A second study assesses the ability of the method to generate activation maps in order to identify the area of interest for ablation and to determine the site of origin (SOO) in patients with idiopathic outflow tract ventricular arrhythmias (OTVAs). Automatic activation maps were compared with manual maps created during the procedure, showing similar accuracy in identifying the earliest activation area for ablation purposes and a slightly superior performance in the SOO identification of idiopathic OTVAs. Therefore, these results suggest that the proposed automatic b-EGM delineator may potentially help to reduce mapping acquisition time, especially when multi-electrode catheters are used, to reduce operator variability and to increase ablation outcomes.

In chapter 3, a novel spatiotemporal approach to resolve high-density cardiac activation during atrial fibrillation (AF) using multi-electrode array (MEA) sensors is

introduced and evaluated. Classic activation detection approaches from unipolar electrogram (u-EGM) signals simplifies the signal information to just a time-occurrence signal, rejecting the remaining spatiotemporal information embedded in the shape of u-EGMs. The method was evaluated against audited annotations from an expert electrophysiologist of recordings using a MEA sensor from a single patient ongoing open chest surgery during sinus rhythm and AF. The method provides smooth and accurate activation maps compared with the expert annotations and also provides “*loci maps*” that allow to visualize information regarding the number of concomitant wavefronts underpassing the MEA sensor and substrate properties. These results open the possibility of robust analysis of high-density activations maps and the development of minimally invasive high-density mapping.

In chapter 4, a predictability framework for analysis of AF activity, based on the concept of the Granger causality (GC), is introduced and evaluated. It is motivated by the fact that some EGM-based quantitative approaches for AF analysis rely on activation detection outcomes and/or do not take into consideration the spatiotemporal relation existing between close electrodes. The framework is evaluated in seven different simulation scenarios, which cover a wide range of propagation patterns, and in mapping data from patients showing different spatiotemporal patterns of AF. The proposed GC-based indices are able to differentiate the stability of the activation and can be combined for obtaining activity maps showing, in a single graph, the propagation of the activation and the stability of the cardiac substrate. Therefore, the proposed GC-based predictability framework is able to characterize and identify areas of AF instability and to track propagation, thus being able to guide the ablation procedure; it does not require activation detection or post-processing algorithms and it is applicable to any multi-electrode catheter.

In conclusion, a set of tools based on signal processing of intracardiac EGM signals for mapping and characterising cardiac arrhythmias has been proposed and validated in this thesis. Each contribution is oriented within a spatiotemporal approach, providing solutions that take into consideration both the specific problem as well as the complexity of cardiac arrhythmias.

Keywords: Atrial fibrillation, cardiac arrhythmias, catheter ablation, electrophysiology, intracardiac electrograms, signal processing, ventricular tachycardia.



Resumen y Conclusiones

Las enfermedades cardiovasculares representan la principal causa de muerte a nivel mundial, especialmente en los Estados Unidos y Europa. Algunas de estas enfermedades se manifiestan como eventos arrítmicos, es decir, como alteraciones del ritmo sinusal normal del corazón.

El tratamiento de las arritmias cardíacas depende del paciente y del tipo de arritmia que éste padezca. Los fármacos antiarrítmicos son el principal tratamiento de dichas arritmias, sin embargo, la ablación por catéter se postula como la principal terapia de elección sobre todo cuando la enfermedad se encuentra en sus primeros estadios, los fármacos antiarrítmicos no son efectivos o se puede identificar el foco de la arritmia. La ablación por catéter es una técnica quirúrgica mínimamente invasiva que introduce pequeños catéteres en las cavidades cardíacas. Estos catéteres disponen de electrodos que permiten medir la actividad eléctrica local del corazón, conocida como señal electrograma (EGM), tanto en ritmo sinusal como durante la arritmia. Basándose en las características de dicha actividad eléctrica, se aplica energía de radiofrecuencia para lesionar o ablacinar los lugares responsables de la arritmia clínica.

Esta tesis doctoral tiene como objetivo investigar técnicas de procesamiento de señales invasivas EGM para proveer de herramientas útiles que ayuden a los procesos de decisión durante los procedimientos de ablación por catéter o estudios electrofisiológicos.

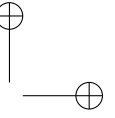
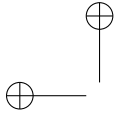
En el capítulo 2, se introduce y evalúa un delineador automático de señales EGM basado en la transformada wavelet de la envolvente compleja de la señal electrograma bipolar (b-EGM). Este algoritmo viene motivado por la necesidad de un sistema para medir los tiempos de activación locales (LATs) para la reconstrucción de los mapas de activación ventriculares usando sistemas de mapeo electroanatómico (EAM) de forma independiente del observador u operador del sistema. En un primer estudio, se evalúa la precisión del método usando como referencia anotaciones manuales de los LATs realizadas por dos expertos, mostrando un error de magnitud similar al obtenido por las anotaciones manuales de los LATs realizadas durante la intervención en el laboratorio de electrofisiología. En un segundo estudio, se evalúa la capacidad del método para generar mapas de activación automáticos que permitan identificar el área de interés para realizar la ablación y determinar el lugar de origen (SOO) de la arritmia. Con este objetivo se han utilizado datos de pacientes con arritmias ventriculares idiopáticas del tracto de salida de los cuales se ha comparado los mapas de activación generados automáticamente con mapas de activación obtenidos manualmente durante la intervención, obteniendo una precisión similar entre ambos conjuntos de mapas de activación

en la identificación del área de activación precoz para la ablación y un rendimiento ligeramente superior en la identificación del SOO de las arritmias ventriculares idiopáticas del tracto de salida de los mapas de activación generados automáticamente. Por lo tanto, estos resultados sugieren que el delineador automático de b-EGMs propuesto puede contribuir a reducir el tiempo de adquisición de los mapas electroanatómicos, especialmente en combinación con catéteres multi-electrodo; reduciendo asimismo la variabilidad en la identificación de los LATs por parte de diferentes operadores, y mejorando los resultados de la ablación.

En el capítulo 3, se introduce y evalúa una estrategia espaciotemporal para la obtención de mapas de activación de alta densidad durante fibrilación auricular (AF) usando sensores de agrupaciones multi-electrodo (MEA). Esta estrategia de detección espaciotemporal se motiva en que las estrategias clásicas para la detección de las activaciones en la señal electrograma unipolar (u-EGM) simplifican la información de la señal a solo una señal de tiempos de ocurrencia, eliminando en este proceso la información espaciotemporal restante que está contenida en la forma de la señal u-EGM. El método propuesto se evalúa frente a anotaciones auditadas por un experto electrofisiólogo en registros usando sensores MEA, durante ritmo sinusal y AF, de un paciente al que se le ha practicado cirugía abierta de tórax. El método obtiene mapas de activación suavizados y precisos comparados con las anotaciones del experto electrofisiólogo y también obtiene “*mapas de lugares focales*” que permiten visualizar información adicional a los mapas de activación relativa al número de frentes de onda simultáneos que atraviesan el sensor MEA y a las propiedades del sustrato cardíaco observado. Estos resultados abren la posibilidad de estudiar mapas de activación de alta densidad de forma robusta y el desarrollo de catéteres de mapeo intracavitario de alta densidad mínimamente invasivos.

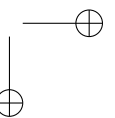
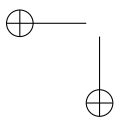
En el capítulo 4, se introduce y evalúa un marco de trabajo para el análisis de la predictibilidad de la AF basado en el concepto de la causalidad de Granger (GC). Este marco de trabajo se motiva en el hecho de que algunas estrategias cuantitativas para el análisis de la AF basadas en el procesado de la señal EGM dependen del rendimiento y resultados de un detector de activaciones y/o no tienen en consideración las relaciones espaciotemporales existentes en la actividad eléctrica medida por electrodos cercanos del catéter de mapeo. El marco de trabajo propuesto se evalúa en siete escenarios de simulación cardíaca que cubren un gran abanico de patrones de propagación, y también en datos de mapeo obtenidos de pacientes que muestran diferentes patrones espaciotemporales de AF. Los índices propuestos basados en la GC son capaces de diferenciar la estabilidad de la activación y se pueden combinar para obtener mapas de actividad que muestran, en una sola imagen, la propagación de la activación a través del catéter y la estabilidad del sustrato medido. Por lo tanto, el marco de trabajo propuesto basado en la GC es capaz de caracterizar e identificar áreas de inestabilidad de la AF y seguir la propagación de dicha actividad, de forma que puede servir para guiar el proceso de ablación; además, no requiere de la detección de activaciones o de algoritmos de post-procesado y se puede aplicar para analizar cualquier catéter de mapeo multi-electrodo.

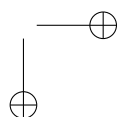
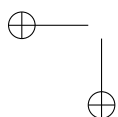
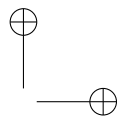
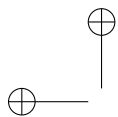
En conclusión, en esta tesis doctoral se proponen y validan un conjunto de herramientas basadas en el procesado de señales intracardíacas EGM con el objetivo de



mapear y caracterizar las arritmias cardíacas para ayudar en la toma de decisiones durante procedimientos de ablación con catéter o estudios electrofisiológicos. Cada una de las contribuciones expuestas en esta tesis propone una solución desde un punto de vista espaciotemporal de forma que se toman en consideración tanto el problema específico a tratar así como la complejidad de las arritmias cardíacas.

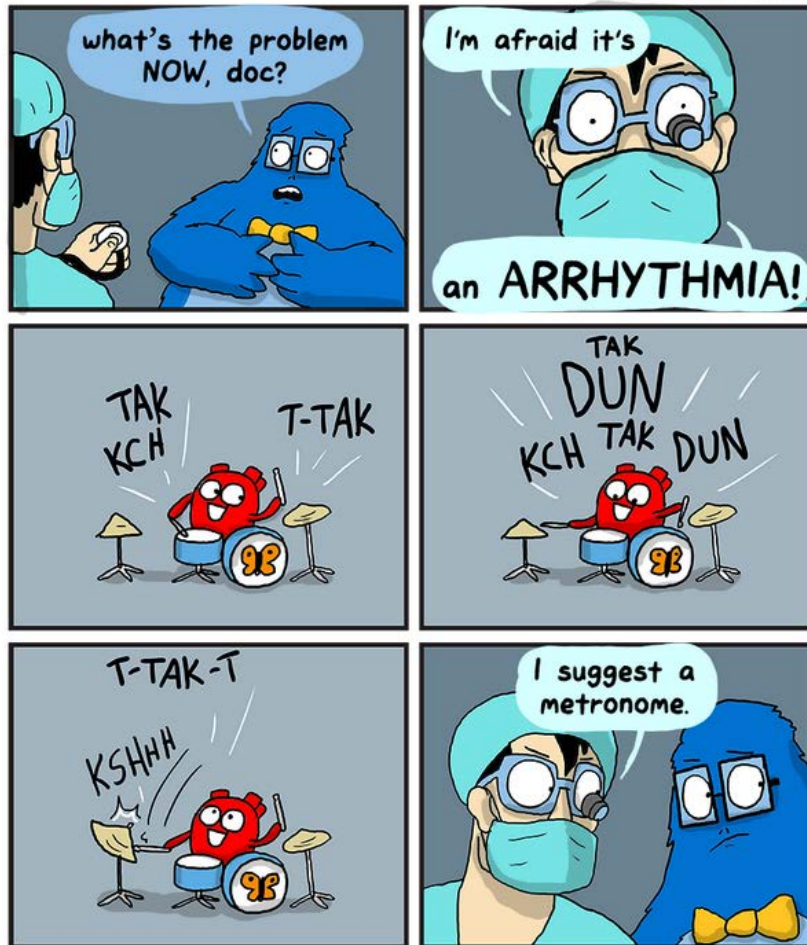
Palabras clave: Ablación por catéter, arritmias cardíacas, electrofisiología, electrograma, fibrilación auricular, taquicardia ventricular, procesado de señales.

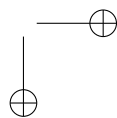
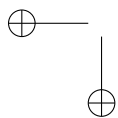
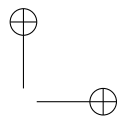
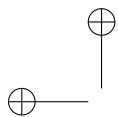


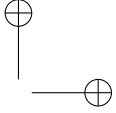
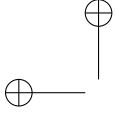


Intracardiac Signal Processing for Mapping and Characterising Cardiac Arrhythmias

THE
AWKWARD YETI







“The only way to do great work is to love what you do. If you haven’t found it yet, keep looking. Don’t settle. As with all matters of the heart, you’ll know when you find it.”

Steven P. Jobs

Acknowledgements

At the beginning of the writing process of this thesis, I promised myself not to start writing this section until finishing the last dot of the entire document. Now, I am in front of my computer, looking to myself writing this sentences and, it is hard to believe that this time arrives.

A Ph.D. thesis is a document that includes (almost) the complete research of the author during a time period, and if one reads the cover, it has an author and a supervisor (two in this case). But the cover is a liar. There are so many people that can be considered author of this thesis as well, because, in a good or bad sense, they contributed to this moment and to the person I am right now. People that know me, already acknowledge my, let say, “bad memory”; thus, I first apologize if you are reading this lines and do not find your name in. Be sure that, if you are reading this, you are part of this thesis as well.

First of all, I would like to thank to the person that mainly contributed to the “scientist” I am right now, my supervisor Juan Pablo Martínez. I know that I am starting to walk this path, but without your firm hands that supported me, I also know that this could had not happened. You are the person who gave me the opportunity (and even encouraged me!) to apply to the grant that introduced me in this vortex (or rotor?) that it is the research process and the hard work needed to make this thesis possible. Thanks to your trust, your encouragement, your stoic patience in each meeting, each paper writing, each English grammar correction or each AVE travel, your wise advices and your support, this work arrived to (I hope) a good end. Second, but not least important, to my co-supervisor Pablo Laguna, from whom I learnt the foundations of my critical thinking and who always has the right word for the right moment. The discussions with you, in the good scientific meaning of the word, always gave me a piece of your wisdom, which I think, is one of the most important marks that can be left in a person.

I would also like to thank the people that guided me before entering into the Ph.D. vortex, to Raquel and Pepo, who fired the “research” flame on me...and here I am. I hope you can see a part of this work as yours as mine, because the first steps walked with you, put me in the right direction.

In general, I would like to thank all the amazing people I had the opportunity to meet (in the present and in the past) and who form the BSICoS Group (former GTC-BIO Group) at the University of Zaragoza: Esther, Edu, Violeta, Michele, Rute, Arantxa, Anita.... But especially, to my great lab colleagues that daily make this

research path more easy to walk, or at least, more fun to walk: To Juan, Lord of the lab and better friend, thank you for all the discussions, laughs and stupidities during this years. To Carlos, the master of the stupidities of the woorld, $\pi\delta\rho$, laugh is a small word at your side, thank you for being such a great guy. To David, the young padawan arrived to the lab in the last years of my work, thanks to make all days interesting. To Daniel and Mariano whose always put up with my random stuff and Apple-fanboyism. And finally, to Fer, I must recognise that I always carried you in my mind during this research...You must be sure that this thesis is also yours.

I cannot left apart my “wavefront” Ph.D. mates whom I shared conferences, coffee times, hotel rooms and the research path: To Julia for always having a time to talk and discuss. To Jesús for being a goal to reach. To Alba for your kindness and always smiling face; and finally, but not least, to David...you know, words are not needed, thank you!

This thesis was also possible thanks to great scientific collaborations that often turn into more than that. The biggest one is with Hospital Clinic and Universitat Pompeu Fabra (Barcelona, Spain). I would like to thank Dr. Oscar Camara and your incredible network weaving abilities. I am aware that if I had not been in that dinner, a big part of our scientific collaboration and of myself could not exist. Thank you for receiving me at UPF in my last research stay and for always behave with me as a colleague and as a friend. I would also like to thank Dr. David Soto for being a friend in the personal and in the scientific side, for being “the guy at the other side in the pipeline (a.k.a. email)”, for all the discussions, developments, interpolations, coffee breaks at UPF, CEK or Clinic, manual editions until the cleaning lady expelled us from the electrophysiology lab.... But most important, thank you for complementing the image side of our developments which highly contributes to this thesis. Also to Dr. Antonio Berruezo, who put the clinical view on the developments of this thesis and who taught me everything I know about electrophysiology and ablation procedures. Thank you for always receiving me in your electrophysiology lab as part of your team and for complement and contribute to our “engineering madness”. The work with all of you is the biggest collaboration that contributes to this thesis and I truly hope it will last many years.

Other important scientific collaborations went out of the Spain borders. First, I had the opportunity to work with Dr. Richard Houben at Applied Biomedical Systems B.V. in Maastricht, The Netherlands. It was my first (and longest) research stay and also it was in a corporation environment. I thank you very much the opportunity of working with you, of knowing what is a corporation environment, and for teaching me everything about mapping of AF. Second, I had the opportunity to work with Dr. Luca Faes at BIOtech centre, Università degli studi di Trento, in Trento, Italy. It was a short period but intense. Work with you, Luca, is like having fun. You treated me as a friend all the time, you helped me with every problem I had and I appreciate (from the personal and scientific side) the kind of person you are. Thank you so much for giving me the opportunity to work and learn with you in Trento. Also I cannot forget to thank Dr. Flavia Ravelli and Dr. Michela Masè for contribute in a very important way to the developments with Luca and me.

In all my stays, I met amazing people that helped me to retain my “mental health”

out of the work and thus contributing to this thesis in a very important way. To my “Spanish family” I had in Maastricht: Anna, Andrés and Anita. To the amazing people I met in Trento: Marco, Lucia, Mara, Christian and Joe. To all the guys at the Ph.D. students lab of UPF whose make me feel like being at home, especially to: Marta, Carlos, Sergio and Rubén. And to the people at Clinic who always supported me with data or clinical interpretations: David Andreu and Juan Acosta.

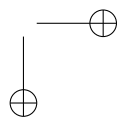
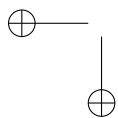
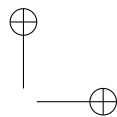
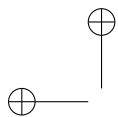
Pero más cerca de mi, hay personas que han estado ahí desde que tengo memoria, y que efectivamente han contribuido de una manera muy personal a la finalización de esta tesis. A mis amigos de toda la vida: Raúl, Iván y Rubén; con los cuales no importa el tiempo y espacio que nos separe, que siempre parece que nos acabemos de ver el día de antes. Gracias por ser vosotros y no cambiéis nunca, para mí sois un tesoro aunque a veces no lo exprese.

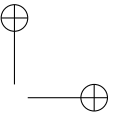
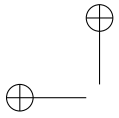
Aunque sin duda alguna, las personas que me han brindado su mayor apoyo, de forma incondicional, sin importar si mis decisiones eran o no las más correctas desde su punto de vista y con una paciencia que rebasa los límites del universo, son mis padres: Sagrario y Sergio. Gracias a vuestra ayuda entre bambalinas, por darme todas las oportunidades habidas y por haber, por estar en cada momento ahí incluso cuando nos separaban cientos de kilómetros y por soportar todo este camino desde las gradas...espero que os sintáis orgullosos del resultado de todo este trabajo, que es tan vuestro como mío.

And finally, to the reader. I hope you find this work interesting and motivational. No matter who you are and why you are reading this text, your sincere interest in my work is a prize for me.



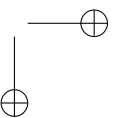
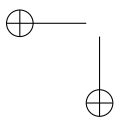
Alejandro Alcaine Otín





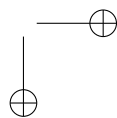
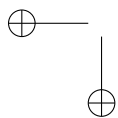
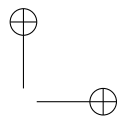
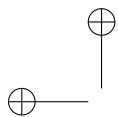
Contents

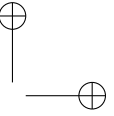
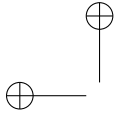
Abstract	i
Resumen y Conclusiones	iii
Acknowledgements	ix
List of Figures	xvii
List of Tables	xix
List of Acronyms	xxi
1 Introduction	1
1.1 Motivation	1
1.2 The Cardiovascular System	1
1.2.1 Anatomy of the Heart	2
1.2.2 Electrical Activity of the Heart	3
1.3 Electrophysiological Mechanisms of Arrhythmias	7
1.3.1 Cardiac Impulse Formation Disorders	7
1.3.2 Cardiac Impulse Propagation Disorders: Reentry	9
1.4 Types of Arrhythmias	13
1.4.1 Bradycardias	13
1.4.2 Tachycardias	13
1.5 Electrophysiological Study of Arrhythmias	15
1.5.1 Catheters	15
1.5.2 Intracardiac Signals	16
1.5.3 Approaches for Cardiac Mapping	18
1.5.4 Non-fluoroscopy Systems	19
1.5.5 Ablation Energy Delivery	21
1.6 Scope and Objectives of the Thesis	23
1.7 Document Organization	24



2	Electroanatomical Ventricular Activation Mapping	27
2.1	Introduction	27
2.1.1	Sequential Electroanatomical Activation Mapping	27
2.1.2	Methods for Sequential Activation Mapping	29
2.1.3	Motivation	30
2.2	The Wavelet-Envelope Detector and Delineator	30
2.2.1	Electrogram Signal Pre-processing: the Hilbert Transform	30
2.2.2	The Wavelet Transform	31
2.2.3	Delineating the Electrogram	35
2.2.4	Including Spatial Information	39
2.3	Delineation Accuracy	40
2.3.1	Testing Database	41
2.3.2	Evaluation Protocol	42
2.3.3	Results	43
2.4	Mapping Performance	46
2.4.1	Idiopathic Outflow Tract Ventricular Arrhythmias	47
2.4.2	Map Descriptors	47
2.4.3	Patient Sample	48
2.4.4	Evaluation Protocol	49
2.4.5	Results	49
2.5	Discussion	52
2.5.1	Algorithm Performance	54
2.5.2	Clinical Application	55
2.5.3	Comparison with Other Methods	59
2.5.4	Limitations	59
2.6	Conclusion	60
3	Spatiotemporal High-Density Atrial Activation Mapping	61
3.1	Introduction	61
3.1.1	Atrial Fibrillation	61
3.1.2	Activation Mapping of Atrial Fibrillation	62
3.1.3	Motivation	63
3.2	Spatiotemporal Activation Mapping Algorithm	63
3.2.1	Algorithm Overview	63
3.2.2	Activation Propagation Pattern and Tissue Model	64
3.2.3	Modelling Unipolar Electrogram Signals	64
3.2.4	Estimation of Tissue Conduction Velocity	65
3.2.5	Focus Initialisation	66
3.2.6	Iterative Model Optimization Algorithm	67
3.2.7	Reconstruction of Activation Maps	69
3.3	Estimation of High-Density Activation Maps	70
3.3.1	Testing Database	70
3.3.2	Evaluation Protocol	71
3.3.3	Results	73
3.4	Discussion	77

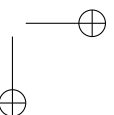
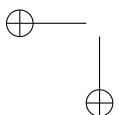
3.4.1	Detection Performance	78
3.4.2	Spatiotemporal Mapping Approach	79
3.4.3	Limitations	79
3.5	Conclusion	80
4	Causal Characterisation of Atrial Activity	81
4.1	Introduction	81
4.1.1	Classification and Treatment of Atrial Fibrillation	81
4.1.2	Quantitative Methods for Atrial Fibrillation Analysis	83
4.1.3	Motivation	83
4.2	The Predictability Framework	84
4.2.1	Multi-Variate Auto-Regressive Modelling	84
4.2.2	Signal Pre-processing	85
4.2.3	The Granger Causality and Predictability	86
4.2.4	Measurement Framework	87
4.3	Predictability Analysis of Atrial Fibrillation	89
4.3.1	Testing Databases	89
4.3.2	Application of the Predictability Framework on Basket Catheter Data	91
4.3.3	Statistical Analysis	92
4.3.4	Results	92
4.4	Discussion	99
4.4.1	Quantification of the Regularity of Simulated Atrial Activity ...	99
4.4.2	Activity Tracking Capability	100
4.4.3	Comparison with Other Methods	101
4.4.4	Limitations	102
4.4.5	Clinical Relevance	102
4.5	Conclusion	102
5	Final Discussion and Conclusion	103
5.1	Summary and Discussion	103
5.1.1	Electroanatomical Activation Mapping of Focal Ventricular Ar- rhythmias	103
5.1.2	Spatiotemporal High-Density Activation Mapping during Atrial Fibrillation	105
5.1.3	Analysis of Causal Interactions during Atrial Fibrillation	105
5.2	Main Limitations	106
5.3	Conclusion	107
5.4	Clinical Implications	107
5.5	Future Work	108
	Bibliography	109
	List of Publications	125



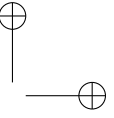
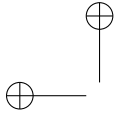


List of Figures

1.1	The cardiovascular system.	2
1.2	Phases of the action potential.	4
1.3	Electrophysiology of the normal heart during sinus rhythm.	5
1.4	Electrode location of the 12-lead electrocardiogram system.	6
1.5	Disorders of the cardiac impulse formation.	8
1.6	Disorders of the cardiac impulse propagation.	10
1.7	Functional reentrant mechanisms.	12
1.8	Examples of mapping and ablation catheters.	16
1.9	Examples of unipolar and bipolar electrogram recordings.	17
1.10	Catheter location technologies of the principal electroanatomical mapping systems.	20
1.11	Illustration of lesion formation of different catheter tip sizes.	22
2.1	Right ventricle activation map in posterior-anterior view.	28
2.2	Local activation time measurement surrogates.	29
2.3	Example of an algorithmic method for local activation time estimation proposed in the bibliography.	30
2.4	Envelope of different electrogram morphologies.	32
2.5	Filter-bank implementation of the diadic discrete wavelet transform.	33
2.6	Implemented wavelet transform.	35
2.7	Block diagram of the wavelet-envelope detector and delineator.	36
2.8	Local activation time detection in representative bipolar electrogram morphologies.	37
2.9	Decision diagram of the spatial consistency algorithm.	39
2.10	Application example of the spatial consistency algorithm.	41
2.11	Lin's concordance correlation factor and Bland-Altman analysis of local activation times using a double expert reference.	44
2.12	Schematic of the right ventricle showing the studied map descriptors.	47
2.13	Map descriptors site of origin identification.	53
2.14	Examples of automatic activation maps compared with different manual annotation sets.	56

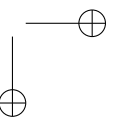
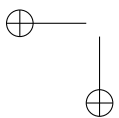


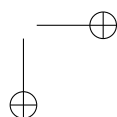
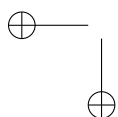
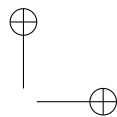
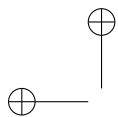
2.15	Examples of manual and automatic activation maps from patients with idiopathic outflow tract ventricular arrhythmia and different arrhythmia origins.	58
3.1	Example of an electrocardiogram recording during atrial fibrillation.	62
3.2	Schematic of the solid angle between an electrode and the activation wavefront.	65
3.3	R-to-S wave ratio evolution with distance to the activation focus.	67
3.4	Schematic of the model optimization algorithm.	68
3.5	Schematic of the mapping procedure in posterior view.	71
3.6	Representative examples of the proposed atrial activity complexity classes.	72
3.7	Agreement evaluation of the estimated local activation times during sinus rhythm.	74
3.8	Agreement evaluation of the estimated local activation times during atrial fibrillation at different complexity levels.	76
3.9	Examples of <i>loci map</i> merged with the estimated activation map.	77
4.1	Classification and treatment of atrial fibrillation.	82
4.2	Examples of quantitative electrogram-based methods for atrial fibrillation analysis.	84
4.3	<i>Botteron</i> and <i>Smith</i> pre-processing chain of bipolar electrogram signals.	85
4.4	Schematic of application of the proposed three-electrode analysis scheme.	88
4.5	Snapshots of different simulated patterns.	90
4.6	Results of the regularity measurements obtained by analysing each simulated scenario from all the possible linear and circular electrode configurations.	93
4.7	Examples of causality analysis maps using the introduced framework from different simulation scenarios.	95
4.8	Activity maps of the simulated basket catheter obtained at different simulation scenarios.	96
4.9	Application of the proposed framework on right atrium basket mapping data in two patients with different spatiotemporal patterns of atrial fibrillation.	98

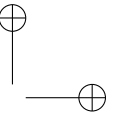
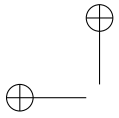


List of Tables

1.1	Intracellular and extracellular ion concentration in cardiac myocytes and its resting potentials.....	3
2.1	Details of the studied database for delineation accuracy assessment.....	42
2.2	Assessment of local activation times using a double expert reference. . . .	44
2.3	Accuracy classification of local activation times using a double expert reference.....	45
2.4	Assessment of local activation times using a double expert reference classified by electrogram voltage amplitude.....	45
2.5	Assessment of local activation times using the single expert reference. . .	46
2.6	Baseline clinical characteristics of the studied patient sample.	50
2.7	Earliest activation site area accuracy assessment.	50
2.8	Map descriptors measurement.	51
2.9	Site of origin identification performance.....	52
3.1	Detection error and performance obtained from the analysis of sinus rhythm recordings.	74
3.2	Detection error and performance obtained from the analysis of atrial fibrillation recordings.....	75
4.1	Regularity measurements obtained from each simulated scenario.	92

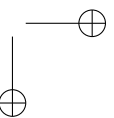
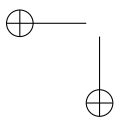




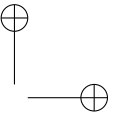
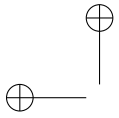


List of Acronyms

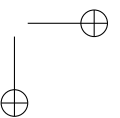
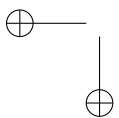
AF	atrial fibrillation	14
AP	action potential	3
AM	activation mapping	18
AOI	area of interest	39
AT	atrial tachycardia	14
AUC	area under the curve	52
AVN	atrioventricular node	5
b-EGM	bipolar electrogram	17
BIC	Bayesian information criterion	85
BSPM	body surface potential mapping	21
BZ	border-zone	43
CAD	coronary artery disease	70
CFAE	complex fractionated atrial electrogram	83
CL	cycle length	10
CS	coronary sinus	15
CT	computed tomography	19
CVD	cardiovascular disease	1
CWT	continuous wavelet transform	31
CZ	core-zone	43
DAD	delayed afterdepolarization	8
DF	dominant frequency	83
DWT	discrete wavelet transform	33
EAS	earliest activation site	28
EAD	early afterdepolarization	8
EAM	electroanatomical mapping	19
ECG	electrocardiogram	4

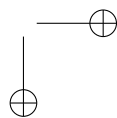
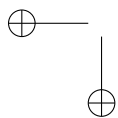
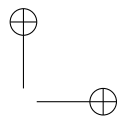
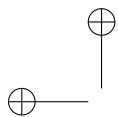


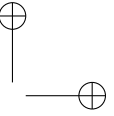
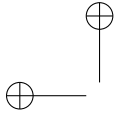
EGM	electrogram.....	16
FIR	finite impulse response.....	33
GC	Granger causality.....	83
HB	His bundle.....	5
HPS	His-Purkinje system.....	5
IIR	infinite impulse response.....	85
LA	left atrium.....	2
LAT	local activation time.....	17
LBB	left bundle branch.....	5
LMM	local maximum-minimum.....	38
LV	left ventricle.....	7
LVOT	left ventricle outflow tract.....	47
MEA	multi-electrode array.....	21
MML	maximum modulus lines.....	36
MVAR	multi-variate auto-regressive.....	84
MRI	magnetic resonance imaging.....	19
MI	myocardial infarction.....	18
OT	outflow tract.....	47
OTVA	outflow tract ventricular arrhythmia.....	47
PDC	partial directed coherence.....	101
PVC	premature ventricular contraction.....	14
PV	pulmonary vein.....	83
PVI	pulmonary vein isolation.....	83
RA	right atrium.....	2
RBB	right bundle branch.....	5
RF	radiofrequency.....	21
RV	right ventricle.....	7
RMS	root mean square.....	91
RMSE	root mean square error.....	66
RVOT	right ventricle outflow tract.....	47
SAN	sinoatrial node.....	5
SD	standard deviation.....	43
SHD	structural heart disease.....	14
SOO	site of origin.....	18



SR	sinus rhythm	4
u-EGM	unipolar electrogram	16
UDL	uniform double layer	64
v-MEA	virtual multi-electrode array	64
VA	ventricular arrhythmia	14
VT	ventricular tachycardia	14







“Each beat of your heart is a small miracle, you know, so don’t get carried away.”

*La Mécanique du Coeur
by Mathias Malzieu*

Chapter 1

Introduction

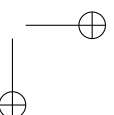
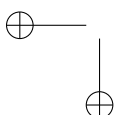
1.1 Motivation	1.4.2 Tachycardias
1.2 The Cardiovascular System	1.5 Electrophysiological Study of Arrhythmias
1.2.1 Anatomy of the Heart	1.5.1 Catheters
1.2.2 Electrical Activity of the Heart	1.5.2 Intracardiac Signals
1.3 Electrophysiological Mechanisms of Arrhythmias	1.5.3 Approaches for Cardiac Mapping
1.3.1 Cardiac Impulse Formation Disorders	1.5.4 Non-fluoroscopy Systems
1.3.2 Cardiac Impulse Propagation Disorders: Reentry	1.5.5 Ablation Energy Delivery
1.4 Types of Arrhythmias	1.6 Scope and Objectives of the Thesis
1.4.1 Bradycardias	1.7 Document Organization

1.1 Motivation

The most common cause of death at global level is cardiovascular disease (CVD) [1]. Particularly, 2016 mortality rate data attributable to CVD ranges from 30.8 % in the US to 45 % in Europe [2, 3]. This supposes an extremely important public health problem with big impact in financial costs, which are predicted to continuously grow over next decades [2].

1.2 The Cardiovascular System

The main function of the cardiovascular system is to serve the needs of the entire body, either by transporting nutrients or waste products. It is composed of two main circuits



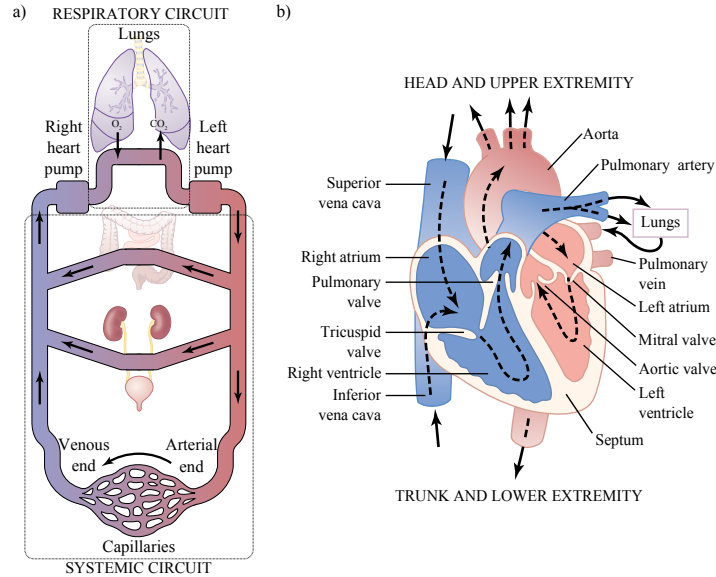


Figure 1.1: The cardiovascular system: a) general organization of the circulatory system and b) anatomy of the heart and blood flow. Reproduced, adapted and modified from [4].

depicted in Fig. 1.1(a): The *systemic* and the *pulmonary* circuits. The systemic (or peripheral) circuit serves oxygen-rich blood to the entire body and carries out carbon dioxide-rich blood. The pulmonary circuit takes this carbon dioxide-rich blood and transforms it into oxygen-rich blood within the lungs. The heart is the organ that maintains these two circuits flowing [4].

1.2.1 Anatomy of the Heart

The heart is a muscular organ of the size of a large fist formed by specialized muscular cells called *myocytes*, which are responsible of both electrical impulse conduction and mechanical contraction [5]. The heart is anatomically divided into two “*mirrored*” pumps, left and right, which support different circulatory systems as shown in Fig. 1.1(a). The right pump takes carbon-dioxide-rich blood from the vein system and pumps it to the respiratory circuit in order to oxygenise the blood in the lungs. Oxygenised blood from the lungs flows to the left side of the heart and then is pumped through the systemic circuit to the peripheral organs [4].

The *septum* separates these two pumps which are additionally divided into two main cavities. One is the *atrium*, which collects blood from the systemic (right atrium (RA)) or the pulmonary (left atrium (LA)) circulatory system circuit; the other cavity is the *ventricle*, which collects blood from the atrium and pumps it out of the heart (see Fig. 1.1(b)). *Systole* is the state when the heart contracts and *diastole* when the heart relaxes.

Table 1.1: Intracellular and extracellular ion concentration in cardiac myocytes and its resting potentials.

Ion	Extracellular concentration (mM)	Intracellular concentration (mM)	Nerst potential (mV)
Na ⁺	135 - 145	10	+70
K ⁺	3.5 - 5.0	155	-94
Ca ²⁺	2	10 ⁻⁴	+132

1.2.2 Electrical Activity of the Heart

Cardiac myocytes have an hydrophobic lipid bilayer that isolate them from all water-soluble substances such as ions. This membrane has transmembrane proteins that allow ions to move across the membrane (called ion channels). The major charge carrier ions present at intra and extracellular media are: sodium (Na⁺), potassium (K⁺), calcium (Ca²⁺) and chloride (Cl⁻) [4, 6].

The Ion movement is driven by two forces: the electrical gradient and the chemical gradient. The chemical gradient force ion movement towards a medium with lesser concentration and the electrical gradient forces ion movement towards a medium with opposite electrical charge [6]. The interplay of these electrochemical gradients ends when the net transmembrane flux of charge (current) is compensated, known as resting potential or *Nerst* potential, which in case of cardiac myocytes is around -90 mV [4–6]. Table 1.1 summarizes the equilibrium ion concentration and each ion's Nerst potential [6].

The Cardiac Action Potential

The action potential (AP) is the electrical result of ion electrochemical interactions between the inner and outer media of special cells, as the myocytes, having the property of *excitability* [7]. Therefore, the AP represents the time variations of the transmembrane potential mediated by the ion flux across the ion channel opening and closing dynamics that yield in mechanical contraction of the myocyte. *Depolarization* is when the transmembrane potential rises over the resting potential and *repolarization* is when it comes back to the resting potential [4, 6]. The cardiac AP has five phases illustrated in Fig. 1.2:

- Phase 4 - Resting: The transmembrane potential remains constant during the diastolic period. During rest, the membrane is permeable to K⁺ and relatively impermeable to other ions. When the transmembrane potential increases over the threshold potential (approximately -65 mV) the cell starts to depolarize [6].
- Phase 0 - Rapid depolarization: Inflow of Na⁺ and Ca²⁺ ions quickly raises the transmembrane potential over the threshold, starting the AP [5]. Rapid Na⁺ currents are the main responsive of Phase 0 onset and mediates Ca²⁺ inwards currents [5, 6].

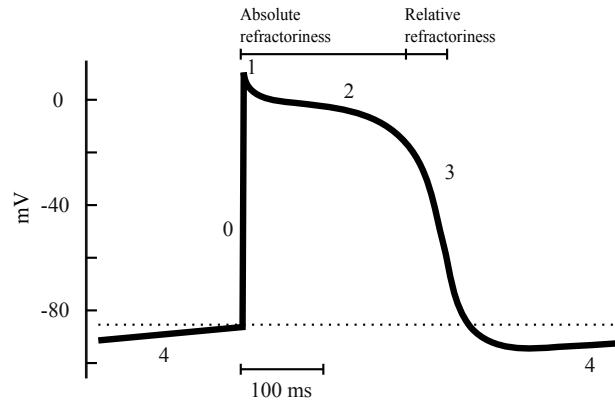


Figure 1.2: Illustration of the phases of the AP on a His-Purkinje cell AP including the refractory periods. Dashed line indicates the threshold potential. Reproduced, adapted and modified from [6].

- Phase 1 - Early repolarization: The Na^+ currents rapidly inactivate, hence yielding to a early repolarization phase with the transmembrane potential falling to approximately 0 mV [5, 6]. This phase is mainly mediated by K^+ outward currents and the Na^+ - Ca^{2+} exchanger [6].
- Phase 2 - Plateau: The plateau phase is unique among excitable cells and represents a balance between Ca^{2+} inward currents, Na^+ currents and repolarizing outward K^+ currents [6].
- Phase 3 - Final rapid repolarization: Resting potential is restored due to dominant outward K^+ currents and deactivation of inward Ca^{2+} currents [6].

Once the AP has been started during a cardiac circle, myocytes become unexcitable to stimulation during a certain amount of time, known as *refractory period* [5, 6]. This time period is physiologically necessary for allowing a correct recovery of the cardiac cells and preventing multiple and compounded APs [6]. Cardiac myocytes present two levels of refractoriness whose time intervals are depicted in Fig. 1.2. The *absolute refractory period* extends 250-300 ms from the AP onset and no stimulus can excite the cell regardless of its strength. The *relative refractory period* lasts round 50 ms and only larger-than normal stimuli can propagate an AP [4-6].

Electrocardiography of the Normal Beating Heart

The heart has a specialized electrical conduction system that delivers the contraction electrical impulse to all cardiac myocytes in order to get a synchronized and rhythmic contraction of the heart, known as sinus rhythm (SR) (see Fig. 1.3(a)-(b)) [4].

The electrocardiogram (ECG) is the representation of the electrical cardiac activity during a heartbeat recorded by different electrodes located on the torso. The specific

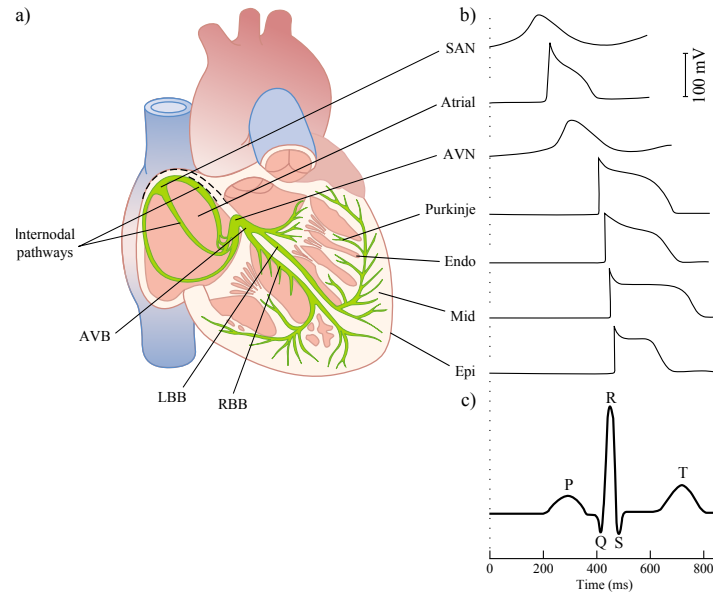


Figure 1.3: Electrophysiology of the normal heart during SR: a) the electrical conducting system of the heart, b) normal beat AP sequence of the different involved structures and c) surface electrocardiographic representation of the normal beat with the different waveforms. Reproduced, adapted and modified from [4,6]. AVB: atrioventricular bundle, AVN: atrioventricular node, LBB: left bundle branch, RBB: right bundle branch, SAN: sinoatrial node.

location of these electrode is known as *lead*. The ECG shows a set of waveforms that represent the different phases of the cardiac cycle (see Fig. 1.3(c)) [7].

During normal SR, the electrical impulse starts in the sinoatrial node (SAN), a cluster of specialized muscular cells located in the superior posterolateral wall of the RA immediately below and slightly lateral to the opening of the superior vena cava [4]. The impulse is directed through internodal pathways to the atrioventricular node (AVN) whereas depolarizing the atrium. The P wave (see Fig. 1.3(c)) in the electrical representation of the atrial depolarization (systole) in the surface ECG.

The AVN holds the impulse to allow the atrium mechanical contraction and ventricle blood filling; represented as the electrically silent period after P wave shown in Fig. 1.3(c). Then, the impulse rapidly spreads through the His bundle (HB) (divided on the left bundle branch (LBB) and right bundle branch (LBB) which serve each ventricle, respectively) and the His-Purkinje system (HPS) reaching each part of the ventricles, causing its depolarization (systole). Ventricular depolarization is represented in the surface ECG by the Q, R and S waves known as QRS complex (see Fig. 1.3(c)). During ventricle depolarization, the atrium repolarizes in order to reach a relaxation state (diastole).

Finally, ventricles repolarize in order to reach the relaxation state (diastole) and prepare for a new beat, represented in the surface ECG as the T wave (see Fig. 1.3(c)).

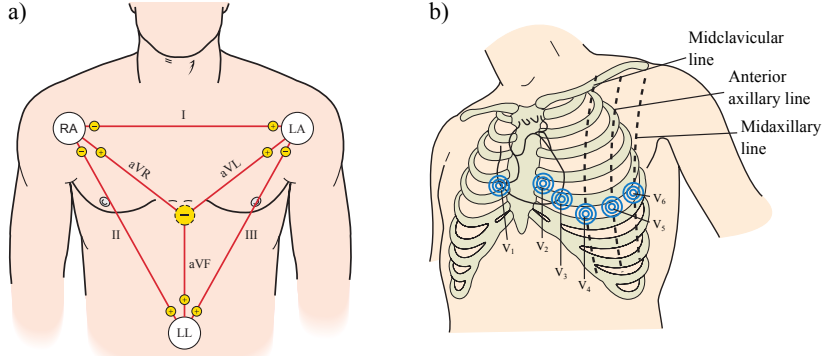


Figure 1.4: Electrode location of the 12-lead ECG system: a) unipolar and bipolar limb leads electrode location and b) unipolar precordial leads electrode location. Reproduced, adapted and modified from [8].

The ECG is an interesting tool for diagnosis of CVDs which reflect as disorders in the heart's electrical activity. The 12-lead ECG system is the most widely-used electrode configuration used in clinical practice [7]. It is composed by 3 bipolar limb leads, 3 augmented unipolar limb leads and 6 precordial unipolar leads, whose electrode locations are illustrated in Fig. 1.4.

The bipolar limb leads were introduced by the Dutch physiologist Willem Einthoven in the early 20th century [7]. Therefore, this three-lead configuration is known as the “*Einthoven's Triangle*”. These leads are denoted as *I*, *II* and *III*; and are obtained as:

$$I = V_{LA} - V_{RA}, \quad (1.1)$$

$$II = V_{LL} - V_{RA}, \quad (1.2)$$

$$III = V_{LL} - V_{LA}, \quad (1.3)$$

where V_{RA} , V_{LA} and V_{LL} are the voltage variations sensed by the electrodes located at the right arm, left arm and left leg, respectively and illustrated in Fig. 1.4(a). These leads show the frontal plane of the heart activity in 60° orientation gaps. Therefore, for spatial completion of the existing 30° gap between these leads, the *augmented unipolar limb leads* (denoted *aVL*, *aVR* and *aVF*) were introduced [7]:

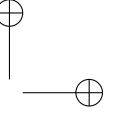
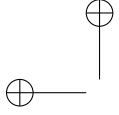
$$aVR = V_{RA} - \frac{V_{LA} + V_{LL}}{2}, \quad (1.4)$$

$$aVL = V_{LA} - \frac{V_{RA} + V_{LL}}{2}, \quad (1.5)$$

$$aVF = V_{LL} - \frac{V_{LA} + V_{RA}}{2}, \quad (1.6)$$

where each augmented lead can be seen as the voltage difference between each vertex of the triangle and the average voltage of the remaining two vertices.

Finally, the *precordial leads*, labelled from V_1 to V_6 , are positioned in succession on the front and left sides of the chest, as illustrated in Fig. 1.4(b). The precordial



leads are unipolar, and are referred to as the *Wilson central terminal* obtained as the average voltage measured at the right and left arms and at the left leg:

$$V_{\text{WCT}} = \frac{V_{\text{LA}} + V_{\text{RA}} + V_{\text{LL}}}{3}. \quad (1.7)$$

The precordial leads provide a more detailed view of the heart: V_1 and V_2 mainly reflect the activity of the right ventricle (RV), V_3 and V_4 show the activity of the anterior wall of the left ventricle (LV) and V_5 and V_6 the lateral wall of the LV [7].

Arrhythmias

Arrhythmias are alterations of the normal SR of the heart either by increasing (> 100 beats/min) or decreasing (< 60 beats/min) the normal rate. Each arrhythmia courses with different symptoms and its management and treatment depends on its mechanism and type.

1.3 Electrophysiological Mechanisms of Arrhythmias

The electrophysiological mechanisms involved on the initiation and perpetuation of cardiac arrhythmias can be divided into: 1) cardiac impulse formation disorders (automaticity and trigger activity) and 2) cardiac impulse propagation disorders (reentry) [5, 6, 9–11]. However, a specific arrhythmia can occur as a combination of both mechanisms.

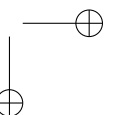
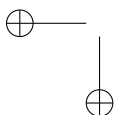
1.3.1 Cardiac Impulse Formation Disorders

Automaticity

Automaticity is defined as the ability of a cardiac cell to spontaneously depolarize, reach the threshold potential and trigger an AP in the absence of any external stimulus [6].

Automaticity can be referred as normal when arising from natural pacemaker cells in the SAN or other subsidiary and latent structures as some atrial parts, the AVN and the HPS [6, 12]. SAN cells have shorter AP period than the subsidiary pacemaker cells, thus in normal condition, it depresses the automaticity of the subsidiary pacemaker cells. Therefore, those structures remain as a fail-safe mechanism ensuring the maintenance of ventricular activation [6, 13]. However, any change in normal automaticity (see Fig. 1.5(c)), either by suppression of SAN activity and/or *enhanced automaticity* of the subsidiary structures, can be responsible of arrhythmia development [5, 6].

On the other hand, *abnormal automaticity* develops when major abnormalities in the cell transmembrane potential are present, particularly in the steady-state depolarization of the membrane potentials (see Fig. 1.5(a)–(b)). This can happen anywhere in the heart and it is not limited to the normal pacemaker structures [6]. Working



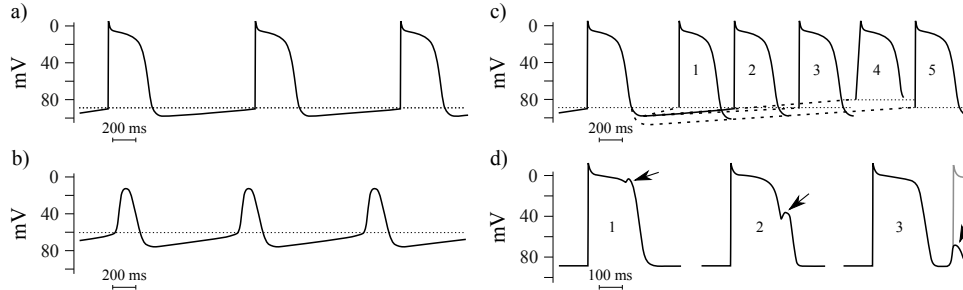


Figure 1.5: Disorders of the cardiac impulse formation: a) normal His-Purkinje AP, b) abnormal automaticity of the His-Purkinje cell resembling SAN AP when increased resting potential, c) different modulations of AP rate: 1) increasing rate of phase 4 depolarization, 2) normal rate, 3) slowing rate of phase 4 depolarization, 4) increasing threshold potential, 5) hyperpolarization and d) different types of afterdepolarizations (pointed by arrows) in His-Purkinje cell APs: 1) phase 2 EAD, 2) phase 3 EAD, 3) subthreshold DAD (bold line) occurring after full repolarization and triggered AP by a DAD (grey line). Dashed line in panels (a)–(c) indicates Nernst potential. Reproduced, adapted and modified from [6].

atrial or ventricular cells do not have spontaneous depolarization due to their low resting potential (-120 to -170 mV), even when they are not excited during a long period. However, several factors such as I_K activation or deactivation, sarcoplasmic Ca^{2+} release, catecholamines, ischemia and infarction can increase this resting potential allowing these cells to spontaneously depolarize [5, 6]. Therefore, abnormal automaticity can contribute to a shift of the pacemaker from the SAN to another place of the heart promoting an arrhythmic event.

Trigger Activity

Trigger activity stands for the impulse initiation in cardiac cells that occurs consequent to one or more preceding APs due to depolarizing oscillation in the membrane voltage, which are known as afterdepolarizations [6, 14].

Afterdepolarizations occurring early during the repolarization phase of the AP are known as early afterdepolarizations (EADs) while those occurring late after completion of the repolarization phase are known as delayed afterdepolarizations (DADs). When an afterdepolarization reaches the threshold potential for activation of an inward current, a new AP is generated, hence referred to as triggered AP.

Membrane voltage oscillations within the diastolic period define a DAD, which distinguishes from spontaneous normal pacemaker by its transient nature (see Fig. 1.5(d.3)) [6]. A triggered AP happens when a DAD reaches the voltage threshold, moreover, this triggered AP can be followed again by other DAD which may or not reach the threshold and promote a new AP, therefore DADs are usually shown in short or long trains [6]. DADs amplitude and rate depend proportionally to cycle length, helping to sustain the arrhythmic event [5, 6]. Commonly, DADs occur under conditions in which increases intracellular Ca^{2+} concentration [5, 6, 11, 15].

On the other hand, EADs are membrane potential oscillations occurring during the AP, hence interrupting the normal repolarization process of the myocyte, changing the time course of the repolarization such that the membrane potential rises in depolarization direction, as illustrated in Fig. 1.5(d.1–2) [6]. EADs have been classified as phase 2 or 3 EADs (see Fig. 1.5(d.1–2)). However, their ionic mechanisms differ [5, 6, 11]. The plateau phase of the AP is a high resistance (low conductance) phase of the membrane. Consequently, small changes in ion currents can promote EADs [5, 6]. Phase 2 EADs seem to be related with I_{Ca-L} current while phase 3 EADs may be due to low I_{K1} current [5]. Prolongation of the AP is a fundamental condition underlying the development of EADs, whose amplitude increase at slow rates [5, 6].

1.3.2 Cardiac Impulse Propagation Disorders: Reentry

During normal excitation of the heart, the propagating impulse extinguishes due to the long tissue refractoriness period compared to the excitation impulse duration. Reentry occurs when this propagating impulse fails to extinguish and persists on activating the heart by finding excitable tissue [6, 16]. Therefore, reentrant tachycardias are repetitive propagations of the activation wave in circular paths returning to its origin in order to reactivate that site [5, 6].

Reentry can be sustained under the following requirements [5, 6]:

- Substrate: Presence of a heterogeneous cardiac tissue with different electrophysiological characteristics, conduction and refractoriness that forms a circuit.
- Area of block: An area of unexcitable cardiac tissue (anatomical or functional) around which the activation wavefront can circulate.
- Unidirectional conduction block.
- Area of slow conduction: Tissue with slow conduction that assures enough time to the circulating wavefront to reach an excitable area proximal to the unidirectional block.
- Critical tissue mass: Tissue which sustains the reentrant circuit.
- Initiating trigger: Changes in heart rate, autonomic tone, ischemia, electrolyte, PH abnormalities or premature depolarization can serve as triggers that initiate the reentrant path causing unidirectional block and slow conduction, hence the arrhythmic event [6].

Wavefront Wavelength and Excitable Gap

The *wavelength* λ quantifies the distance travelled by the activation wavefront relative to the effective refractory period, expressed as [6, 16]:

$$\lambda = v \cdot t_r, \quad (1.8)$$

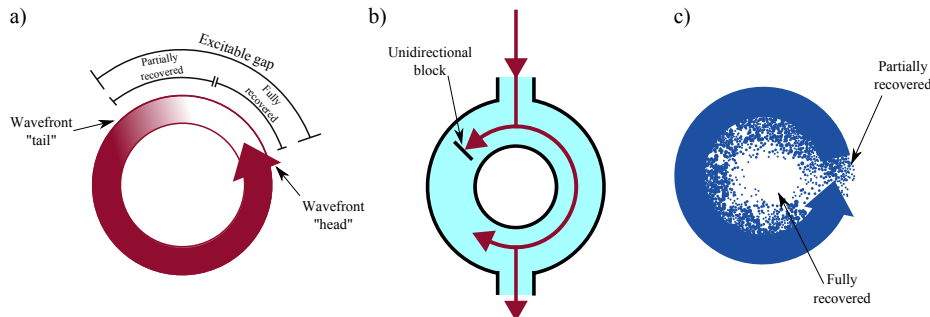


Figure 1.6: Disorders of the cardiac impulse propagation: a) concept of excitable gap, b) anatomical reentry showing an unidirectional block and slow conduction of the retrograde wavefront sustaining the reentry path and c) functional reentry where dots indicated partial recovery. Reproduced, adapted and modified from [6].

where v and t_r stand for the conducting velocity and the relative refractory period of the tissue, respectively.

The wavelength of the activation wavefront must be shorter than the length of the potential reentrant circuit pathway for reentrant excitation to occur [6]. Therefore, the excitable gap occurs as long as the extension of the refractory zone (“tail”) behind the excitation wave (“head”) is smaller than the entire length of the reentrant pathway, as illustrated in Fig. 1.6(a) [5, 6, 16]. Hence, the existence of this excitable gap allows the reentrant wavefront to continue propagate along the reentrant circuit.

A fully excitable gap is defined as the part of the reentrant circuit where the *tail* of the preceding wavefront does not affect the *head* and the velocity of the following wave, i.e., absence of *head-tail* interaction. On the other hand, the partially excitable gap is defined as the zone where the rotating wavefront can be captured by local stimulation in the presence of *head-tail* interaction (see Fig. 1.6(a)) [6, 16].

The excitable gap characteristics may be different among types of reentrant circuits [6, 16]. Many anatomically related circuits have large excitable gaps with a fully excitable area, although it can be also only partially excitable. On the other hand, functional circuits have often small and partially excitable gaps [6, 16]. This phenomenon connects with the stability of the reentrant arrhythmia. While the wavefront wavelength is smaller than the reentrant path, the excitable gap is stable respecting to the frequency of rotation and so the cycle length (CL) of the arrhythmia will be stable. However, in the setting where the wavelength of the excitation exceeds the reentrant pathway, the excitation wave encounters the non-excitable tissue and extinguish. The intermediate situation, where the head of the wavefront meets the partially recovered tissue, leads to unstable CLs and complex dynamics of the arrhythmia [6].

The existence and extent of excitable gaps in reentrant circuits has important implications [16]: 1) it enables modulation of the frequency of a reentrant tachycardia by external or local stimuli, 2) it can determine the effect of drugs in the reentrant circuits and 3) it may be exploited in order to terminate the arrhythmia.

Anatomical Reentry

It was first observed by *Meyer* in a subumbrella tissue preparation of jellyfish [17] and confirmed later by *Mines* in heart muscle preparations [18]. This type of reentry is based on an unexcitable anatomical obstacle surrounded by a substrate which allows the wavefront to reenter, creating fixed and stable reentrant circuits [5,6].

As illustrated in Fig. 1.6(b), the anatomical obstacle determines two pathways; when the wavefront encounters the anatomical obstacle, it travels down one path and gets blocked (unidirectional block) and the wavefront of the other path encounters the unidirectional block starting the reentry [5,18]. Hence, the anatomically-based reentry pathway is usually longer than the wavefront wavelength, yielding in stable CL arrhythmias [6].

Functional Reentry

It was first hypothesized by *Garrey* in 1914 [19]. Functional reentry is determined by dynamic heterogeneities in the electrophysiological properties of the cardiac tissue without the intervention of anatomical structures or conducting pathways, as illustrated in Fig. 1.6(c) [5,6]. Such heterogeneities involve dispersion of excitability or refractoriness and conduction velocity, as well as anisotropic conduction properties of the myocardium [6].

Usually, the size of the functional reentrant circuits is small and their rhythm and location are unstable [5]. This occurs due to the different dynamics between the *head* and *tail* of the reentrant wavefront explained by many mechanisms.

In 1977, *Allessie* and co-workers formulated the *leading circle* concept [20]. They described a reentrant wavefront turning around a functionally region of unexcitable tissue or refractory core and among a surrounding tissue with different electrophysiological properties, as illustrated in Fig. 1.7(a). It was defined as “the smallest possible path in which the impulse can continue to circulate” and “in which the stimulating efficacy of the wavefront is just enough to excite the tissue ahead which is still in its relative refractory phase” [20]. Therefore, this reentry is less susceptible to external stimulation because it does not have a fully excitable gap [5].

In 1981, *El-Sherif et al.* [21,24] delineated a *figure of eight* in epicardial mapping of canine infarction models. It consists of two concomitant wavefronts travelling in opposite directions (clockwise and counterclockwise) around two functional or fixed arcs of blocks that merge in a central pathway [5,6,11,24], as illustrated in Fig. 1.7(b). The same pattern can be obtained by creating artificial anatomical obstacles [25] and in functional reentry created by premature stimulation [26].

The concept of *spiral waves* or *rotors* was introduced by *Weiner* and *Rosenbluth* in 1946 but related to anatomical reentry [11,27]. Later, multiple studies translate this concept to functional reentry [22]. Although *spiral waves* are considered similar to the *leading circle* concept, they differentiate in some considerations in two- and three-dimensions [5,6,11,16]. The term *spiral wave* describes a rotational wave in two-dimensions. When the rotational wave occurs in three-dimensions, it is called

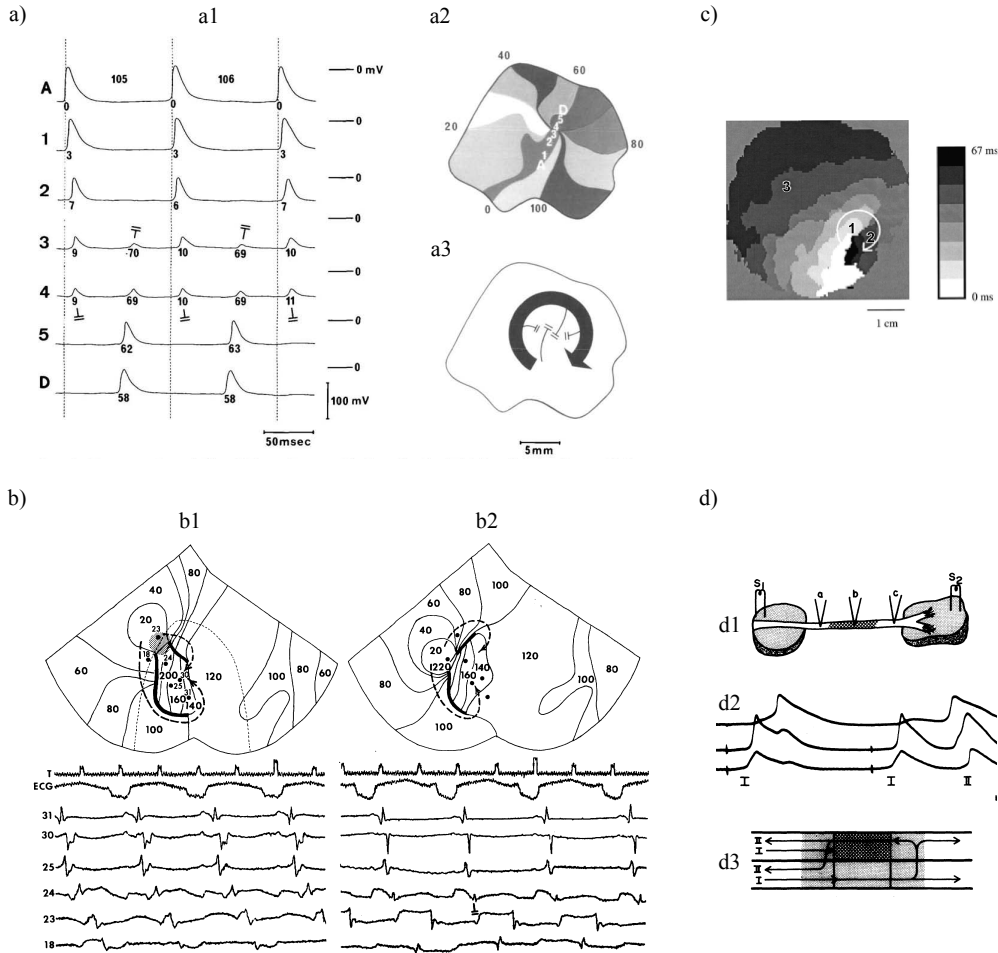
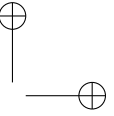
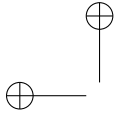


Figure 1.7: Functional reentrant mechanisms: a) leading circle concept (reproduced from [20]) depicted in panel (a1), where panel (a2) shows the corresponding membrane potentials at the points indicated as A,1...5,D in the isochronal activation sequence in panel (a3); b) figure of eight reentry (reproduced from [21]) showing the isochronal map with the figure of eight reentry indicated by dashed arrows at the top of each panel (b1) and (b2), at the bottom are shown recordings of ECG and intracardiac signals from the indicated dots; c) spiral wave (rotor) reentry (reproduced from [22]) illustrated by an isochronal map of optical activity where the rotor evolution is indicated by a white arrow and numbered from 1 to 3; and d) reflection reentry (reproduced from [23]), where panel (d1) shows the preparation of the Purkinje fibre at the sites of excitation (S1 and S2), panel (d2) shows the recording obtained at points a-c and panel (d3) depicts the reflection reentry.



scroll wave. The term *rotor* is commonly used to refer to the rotating source, and *spiral wave* usually refers to the shape (i.e. curvature) of the wave emerging from the rotating wave [6]. Spiral waves are organized activation patterns around a core, which remains unstimulated thanks to the curvature of the spiral wave (see Fig. 1.7(c)). This curvature is the key to core formation because it limits propagation velocities thus resulting in slow conduction and blocks [5, 6, 11]. The tip of the spiral wave can be stationary or move along complex pathways, radiating waves into the medium [5, 6]. In contrast to the *leading circle* concept, rotors have a fully excitable gap [5].

Reflection is a special subclass of reentry where the wavefront does not travel around a functional block but travels back and forth in the same path (e.g. trabecula or Purkinje fibres) containing an area of conduction block [5, 6, 11] as illustrated in Fig. 1.7(d).

Phase 2 reentry is another special subclass of reentry which does not imply a circus movement but can appear to be of focal origin [11]. It occurs when the phase 2 dome of the AP propagates from areas where it is maintained (endocardium and mid-myocardium) to zones where it is abolished (epicardium) causing local excitation and generation of a closely coupled extrasystole [6, 11].

Anisotropy is a normal condition of the heart related to the differential conduction velocity in the transversal vs. longitudinal direction of cardiac fibres [5, 6, 28, 29]. Anisotropy and structural differences between adjacent areas of myocytes can lead to conduction velocity and repolarization heterogeneities that may yield in blocked impulses and slowed conduction, which sets the substrate for reentry [6].

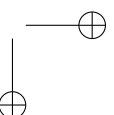
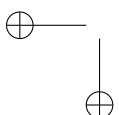
1.4 Types of Arrhythmias

1.4.1 Bradycardias

Bradycardias are defined as those arrhythmias where the normal SR is decelerated below 60 beats/min [4]. In healthy and trained subjects it could be a non-pathological condition [4]; however it may also be cause of SAN dysfunctions, AVN aberrant conduction and other intrinsic or extrinsic factors that may require a pacemaker implantation to restore the normal SR [30–32].

1.4.2 Tachycardias

Tachycardias are defined as those arrhythmias where the normal SR is accelerated above 100 beats/min [4]. Some Tachycardias are life-threatening but some others have benign course. Tachycardias are usually classified according to the part of the heart where they are originated.



Supraventricular Tachycardias

Supraventricular Tachycardias are those arising above the HB bifurcation or have mechanisms dependent of the HB [33]. They are mainly classified into:

- Atrial tachycardia: Rapid and regular rhythm of the atria (100-200 beats/min) with stable P-wave followed by electric silence, no AVN origin and sustained solely by atrial structures [34,35]. Focal-related mechanisms (automaticity and trigger activity) or macroreentry are mainly responsible of atrial tachycardias (ATs) which can arise from almost any part of the atria [35,36].
- Atrial Flutter: Very high rate (240-350 beats/min) atrial tachycardia with continuous oscillating atrial waves without flat isoelectric line. [34,35,37]. Its mechanism is macroreentry and it distinguishes from atrial tachycardia in its dependence with RA anatomy and ECG characteristics [35].
- Atrial Fibrillation: Characterizes by an irregular activation of the atrium (400-700 beats/minute) with absence of distinct repeating P waves in the surface ECG and irregular ventricular response when AVN is reached by the impulses. [4,38]. Mechanisms related with atrial fibrillation (AF) are still under study but covers different combinations of automaticity, trigger activity and reentry. [6,39–46].

Ventricular Tachycardias

Arrhythmias arising from any part of the ventricles below the bifurcation of the HB and independently of AVN conduction are known as ventricular tachycardia (VT) [6]. They are usually classified by its duration and surface ECG QRS complex morphology as:

- Extrasystoles: They are ventricular contractions occurring after a normal beat followed by a pause (also known as ectopy or premature ventricular contraction (PVC) beats). Extrasystoles are related with automaticity, trigger activity and microreentry [47–49]. They can occur independently of the present of structural heart disease (SHD) [49,50]. When there is no underlying SHD, they are known as idiopathic ventricular arrhythmias (VAs) and have benign clinical course and good prognosis. However, frequent extrasystole bursts can cause tachycardia-induced cardiomyopathies [6,49,50].
- Non-sustained Ventricular Tachycardia: They are characterized by bursts of ventricular complexes which self-terminates in less than 30 s [49]. They have similar course that idiopathic VAs but are associated to mortality and sudden cardiac death in SHD patients [50].
- Sustained Monomorphic Ventricular Tachycardia: VT lasting more than 30 s, whose ventricular complexes morphology does not change during the course of the tachycardia or can present different single morphology at different arrhythmia episodes [6]. Reentry is the main mechanism associated to this VTs and it is

frequently related to the presence of myocardial scars [6,51]. Ventricular flutter is recommended to be included in this classification as monomorphic VT with indeterminate QRS morphology [49].

- Polymorphic Ventricular Tachycardia: VT whose ventricular complexes morphology change during the course of the tachycardia indicating a variable sequence of activation of the ventricles [6]. *Torsades de pointes* is an example of polymorphic VT.
- Ventricular Fibrillation: Rapid and irregular ventricular rhythm (usually over 350 beats/min) with strong variability of QRS morphology due to a disorganization of electrical impulses [6] which results fatal if not cardioverted due to the completely inefficient ventricular contraction [4].

1.5 Electrophysiological Study of Arrhythmias

Invasive electrophysiological testing is used in patients with suspected or documented history of cardiac arrhythmias in order to precisely manage the diagnostic and decision process during ablation interventions. It uses multi-electrode catheters, percutaneously located in contact with the cardiac chambers, to record portions of the cardiac electrical activity and perform programmed cardiac electrical stimulation [6].

1.5.1 Catheters

Invasive catheters are used for electrophysiological testing in order to record the electrical activity of the heart and perform electrical stimulation (pacing). Catheters are isolated wires which are attached to a one or more electrodes exposed to the cardiac surface. They are made of different materials depending on the desirable properties (deflectability, curvature, stiffness, etc.) and allow different electrode configurations [6].

Catheters are usually guided through the cardiac structures using fluoroscopy. Right heart structures like RA, HB or RV are commonly accessed via femoral vein; the coronary sinus (CS) is more easily accessed via superior vena cava access, although femoral vein approach can be appropriate in most cases [6]. Femoral artery approach and retrograde aortic access is used for mapping LV and mitral annulus but a transeptal approach can also be used [6,52]. The LA, due to its complex anatomy, is mapped via transeptal puncture from the RA [6,52]. In some special cases, epicardium access is done via a subxiphoid puncture [6].

Multi-electrode catheters have different shapes and electrode configuration (either electrode number or inter-electrode distances) which allow to have special properties for mapping individual heart structures (see Fig. 1.8(a)–(e)). Ablation catheters (see Fig. 1.8(f)) are a special subclass which are equipped with a metal tip (with different tip lengths) connected to an ablation energy generator in order to perform permanent lesions in the cardiac tissue.

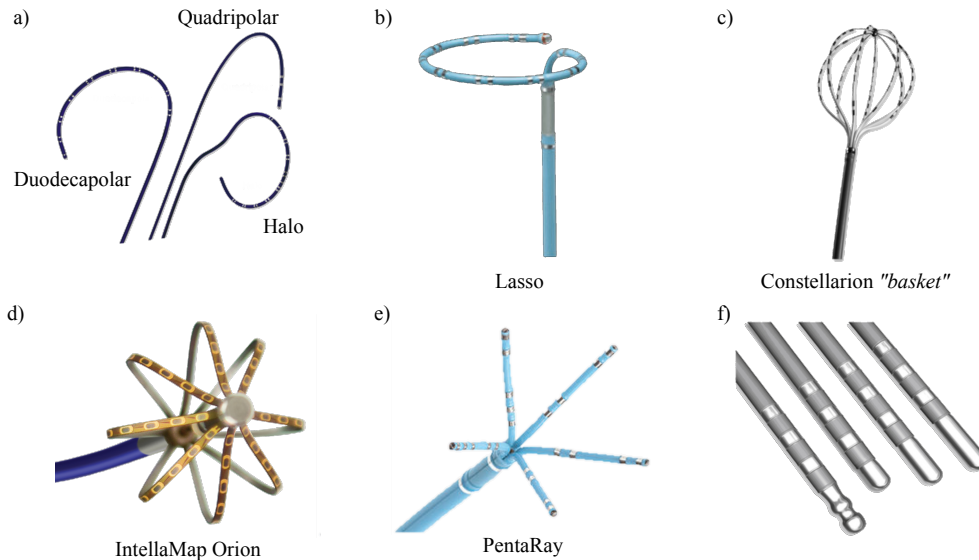


Figure 1.8: Multi-electrode mapping and ablation catheters: a) linear catheters (*Boston Scientific, Inc., Natick, MA, USA*), b) Lasso[®] catheter of different sizes (*Biosense-Webster, Inc., Diamond Bar, CA, USA*), c) Constellation[™] "basket" catheter (*Boston Scientific, Inc., Natick, MA, USA*), d) IntellaMap Orion[™] catheter (*Boston Scientific, Inc., Natick, MA, USA*), e) PentaRay[®] catheter (*Biosense-Webster, Inc., Diamond Bar, CA, USA*) and f) ablation catheters with different tip shape and size (*Boston Scientific, Inc., Natick, MA, USA*).

1.5.2 Intracardiac Signals

Multi-electrode catheters serve for recording the local electrical activity of the heart (otherwise known as electrogram (EGM)) and are connected to a recording system in their proximal part. Depending on the arrangement of these electrodes, different kind of signals with different properties can be acquired from the cardiac activity. In general, EGMs provide information about: 1) the time of activation of the myocardium, 2) the direction of the propagation of the cardiac activity in the field of view of the current electrode and 3) the complexity of myocardial activation within the field of view of the current electrode [6].

Unipolar Electrograms

The local electrical activity sensed by a single electrode referred to a common potential (generally located in the patient's surface) is known as unipolar electrogram (u-EGM). By convention, the electrode in contact with the cardiac tissue is connected to the positive input of the recording amplifier, therefore, an approaching wavefront creates a positive deflection that abruptly reverses itself when the wavefront surpasses the recording electrode with a final return to baseline, hence generating an RS complex [6, 53, 54], as illustrated in Fig. 1.9(a).

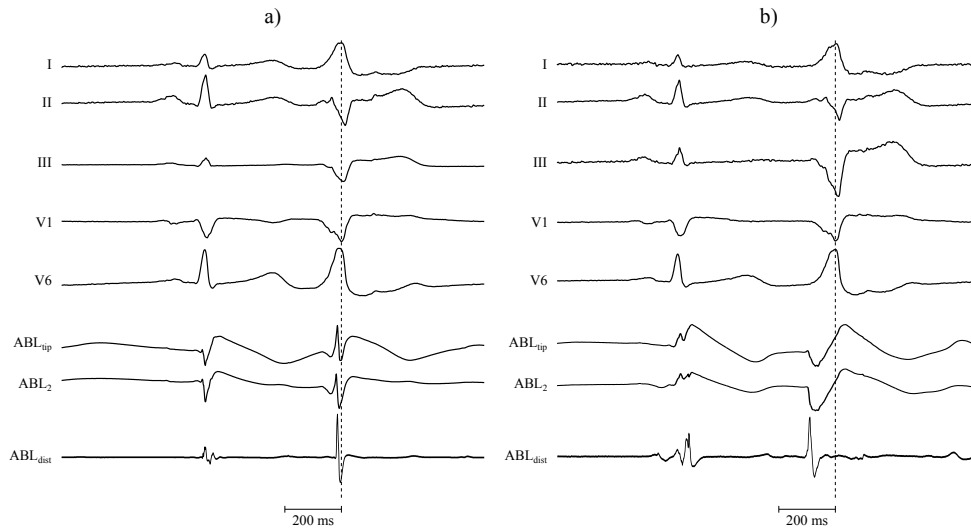


Figure 1.9: Two different recording sites during PVC after a normal beat from a patient with focal VA: a) anywhere in the myocardium and b) close to the VA focus site indicated by the QS morphology at ABL₂. Each panel shows from top to bottom: ECG leads I, II, III, V1 and V6; u-EGM signals recorded at the tip and second electrode of the ablation catheter (noted as ABL_{tip} and ABL₂, respectively) and the distal b-EGM signal from the ablation catheter (noted as ABL_{dist}). Vertical dashed line indicates the reference time for LAT computation.

In homogeneous propagation conditions, the maximum negative slope (dV/dt) of u-EGMs coincides with the phase 0 of the AP corresponding with the rapid Na⁺ intake and thus with the true activation of the myocyte (or local activation time (LAT)) [6, 53, 55, 56]. Also, u-EGMs provide information about the direction of the impulse propagation: positive deflections (i.e. R-waves) are generated by wavefronts propagating towards the electrode whereas negative deflections (i.e. QS morphology and the S-waves) are generated by wavefronts propagating away from the electrode [6, 53–56], as illustrated in Fig. 1.9(b).

The major disadvantage of u-EGMs is they are affected by far-field electrical signals generated by depolarization of tissue remote from the recording electrode. [6, 54, 57]. Despite the interesting properties of u-EGMs regarding timing and direction of the propagation, they are less preferred in clinical routine compared with bipolar electrograms (b-EGMs) [6].

Bipolar Electrograms

A b-EGM signal is obtained by subtraction of the cardiac electrical activity sensed by a pair close electrodes [6, 53, 54], as illustrated in Fig. 1.9. Usually, multi-electrode catheters have short inter-electrode distances (around 2 mm) hence b-EGMs are less sensitive to far-field electrical sources and have high signal-to-noise ratio [6]. Therefore,

b-EGMs allow better identification of local activity, like those coming from myocardial infarction (MI) scar areas, which can be masked by far-field activity [54].

In contrast, the amplitude of the b-EGM depends on the direction of the activation wavefront with respect to the b-EGM recording bipole axis. The b-EGM signal amplitude is maximal if the depolarization wavefront propagates parallel to the recording axis, whereas it is close to zero if the propagation occurs perpendicular to the recording axis [6, 54]. Additionally, in homogeneous conduction, the maximal peak of the b-EGM is related to the LAT [6, 57]; however, in case of complex activation, there is no consensus on the correct b-EGM signal characteristic for LAT measurement [49]. Therefore b-EGMs loses the directivity features and the LAT relation of u-EGMs due to their differentiation nature [6, 53, 54, 57].

1.5.3 Approaches for Cardiac Mapping

Cardiac mapping refers to the process of identifying the spatiotemporal characteristics of the cardiac substrate during a certain heart rhythm [6]. The choose of the correct mapping approach depends on the intrinsic mechanism of the clinical arrhythmia.

Activation Mapping

The analysis of the sequence of myocardial activation during a certain rhythm is referred as activation mapping (AM). It can help to assess the mechanisms that sustain and maintain cardiac arrhythmias and can be used in combination with other mapping techniques [49]. It is indicated to identify the site of origin (SOO) of the activation during focal tachycardias or the critical reentrant isthmus during macroreentrant tachycardias [6, 57].

Pace Mapping

Pace mapping is a technique that helps to localize tachycardia sources by pacing at different endocardial sites in order to reproduce the ECG morphology of the clinical arrhythmia [6]. Pace mapping is more useful for assessing focal tachycardias than for reentrant tachycardias because the reentrant circuit can be activated in a different configuration than the one that promotes the clinical tachycardia [6]. High match on surface ECG for a certain pacing site can be an indicative of the SOO of the clinical arrhythmia [6, 53]. Pace mapping does not require induction of the clinical arrhythmia when this is non-tolerated or non-inducible, thus presenting an advantage over AM [53]. However a pacing site can resemble high ECG morphology similarity to the clinical arrhythmia at distances up to 15 mm away from the true origin [6], hence this mapping approach is less precise than AM [49].

Entrainment Mapping

Entrainment mapping consist of identify the reentrant isthmus of an stable reentrant tachycardia by continuous resetting of the reentrant circuit by a series of stimuli [6, 53]. It is performed by pacing at a slightly superior cycle length than the reentrant arrhythmia until capture of the excitable gap of the reentrant circuit [6, 49, 53, 58]. Once the presence of entrainment is confirmed [49], pacing is terminated and the post pacing interval is analysed in order to establish the relation of the pacing site with the reentrant circuit and identify the ablation targets [6, 49, 58].

Substrate/Voltage Mapping

Substrate/voltage mapping is a non-conventional mapping approach that requires the usage of an electroanatomical mapping (EAM) system for data visualization. It consists on evaluating the amplitude (voltage) of the b-EGM signal in order to characterize areas involved in the generation and maintenance of reentrant arrhythmias [49]. This mapping approach facilitates the ablation of multiple VTs, pleomorphic VTs and unmappable VTs due to haemodynamic instability, non-inducibility or non-tolerance [49]. It is usually helpful for catheter ablation of scar-related post-MI VTs [49, 51]

1.5.4 Non-fluoroscopy Systems

Catheter ablation interventions have become a first-line therapy in multiple scenarios [49, 59]. In those interventions, catheters were introduced within the cardiac chambers and located using fluoroscopy and EGM signals have been interpreted by the physician using conventional recording systems. Recent technological advances have yield in the development of non-fluoroscopy systems (otherwise known as EAM systems) that locate multiple catheters in a three-dimensional space within the patient's chest and provides tools for interpretation of the cardiac substrate [57, 60]. With some differences in the operation principles among EAM systems, their common features are [49, 60]:

- Three-dimensional location of multiple catheters within the patient's chest that allows the reconstruction of the cardiac anatomy and minimize fluoroscopy exposure.
- Display EGM signal characteristics (most commonly activation and voltage) in the electroanatomical cardiac anatomy using a colour-coded scale.
- Allow integration of radiographic anatomy (computed tomography (CT), magnetic resonance imaging (MRI), fluoroscopy) in relation with the catheter position within the electroanatomical cardiac anatomy.
- Use of visual tags that help to identify areas of interest within the electroanatomical cardiac anatomy.

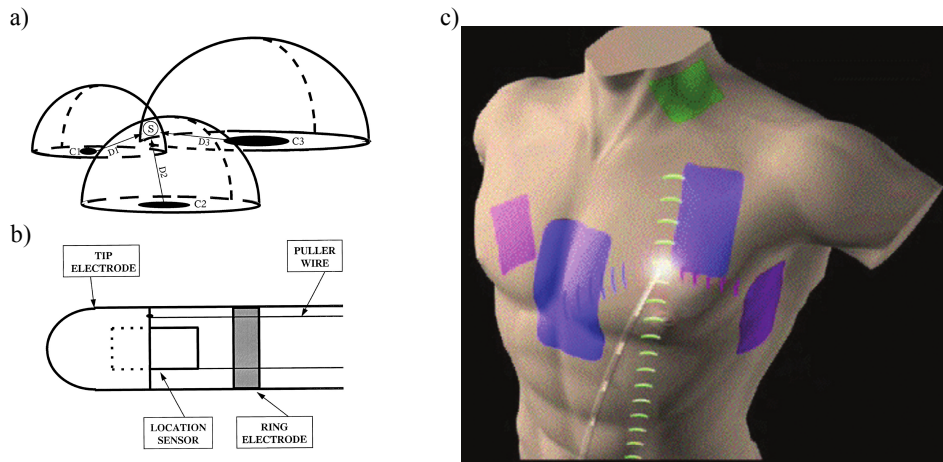


Figure 1.10: Catheter location technologies of the principal EAM systems: a) diagram of the location pad of CARTO[®] system (reproduced from [61]), b) diagram of the mapping catheter sensor of CARTO[®] system (reproduced from [61]), and c) orthogonal surface patches for catheter location of the EnSite[™] NavX[™] system (reproduced from [60]).

CARTO[®] Electroanatomical Mapping System

The CARTO[®] EAM system is developed by *Biosense Webster Inc.* (Diamond Bar, California, USA) and it is one of the most commonly used EAM systems in clinical practice. The system uses ultra-low energy magnetic fields emitted from three coils in a locator pad beneath the laboratory table (see Fig. 1.10(a)) [61–63]. These magnetic fields are sensed by a sensor embedded in the tip of the mapping catheter, which different field strengths allow to triangulate the catheter tip position within the patient’s chest (see Fig. 1.10(b)) [61–63].

EnSite[™] NavX[™] Electroanatomical Mapping System

The EnSite[™] NavX[™] EAM system is developed by *St. Jude Medical Inc.* (St. Paul, Minnesota, USA) and it is also widely used in clinical practice. The location system is based on measuring the impedance variation from the catheter to three pairs of patches (a pair for each spatial coordinate, see Fig. 1.10(c)) connected to a low-current generator [64]. The main characteristics of the NavX[™] EAM system is its ability to locate any diagnostic and ablation catheter within the patient’s chest without using an special catheter equipped with sensors [6, 60].

Other Systems

Other EAM systems technologies are available in the market as well as experimental technologies proposed to overcome the limitations of current EAM system approaches.

One of them is a non-contact mapping system and multi-electrode array (MEA) catheter (EnSite™ 3000 system, *St. Jude Medical Inc., St. Paul, MN, USA*). This system uses a 64 electrode MEA mounted on an inflatable balloon which is located within the cardiac chambers and expanded without contact with the myocardium. Therefore, the system measures far-field electrical activity and allows to reconstruct the surface cardiac activity by computation of virtual EGMs using a single beat [65].

More recently, the Rhythmia™ contact EAM system developed by *Boston Scientific Inc.* (Natick, Massachusetts, USA) has become clinically available. It combines magnetic and impedance localization technologies paired with the IntellaMap Orion™ 64 mini-electrode catheter (*Boston Scientific Inc., Natick, MA, USA*, See Fig. 1.8(d)) [66]. The main advantage of this system is the rapid acquisition of high-density electroanatomical maps without the need of manual annotation [66, 67].

Other experimental technologies use robot and/or magnetic navigation to overcome the necessary skills in catheter manipulation of electrophysiologists, reduce radiation exposure of the patient and operator and reduce intervention times [49].

Moreover, body surface potential mapping (BSPM) is being investigated as a non-invasive measurement of cardiac activity during arrhythmias in order to precisely plan ablation interventions [6]. BSPM places multiple surface ECG electrodes in the patient's chest and compute the inverse problem to derive potential activation of the myocardium projected on CT or MRI anatomy of the patient's heart [6, 68].

1.5.5 Ablation Energy Delivery

After electroanatomical mapping and proper identification of the arrhythmia mechanism and ablation target, permanent lesions in the arrhythmogenic tissue are achieved by heating the cardiac tissue above 50°C [6, 49, 69].

Radiofrequency Ablation Energy

The most common form of ablation energy is radiofrequency (RF) energy [49]. Electrosurgery RF ablation energy currently uses hectometric wavelengths, around 300-1000 kHz, being electrically conducted to the cardiac tissue through the catheter tip. In this setting, the body becomes a part of the in-series circuit formed between the RF generator connected to the catheter tip and a ground pad located in the patient's skin (unipolar configuration). This circuit forms lines of field (currents) that flow from the catheter tip to the ground pad whose energy dissipates as heat; thus, the high current density around the catheter tip heats the tissue in contact with the catheter tip [6].

The thermal injury created by RF ablation is due to two phenomena: resistive heating and conductive heating. Resistive heating refers to the ablation lesion created by direct contact of the catheter tip with the tissue, which spans in a 1-2 mm rim behind the electrode. Conductive heating refers to the conduction of the thermal heating created by direct contact which spans to a distance depending on the applied power and continues after RF application stops (see Fig. 1.11(b)–(c)) [6, 69].

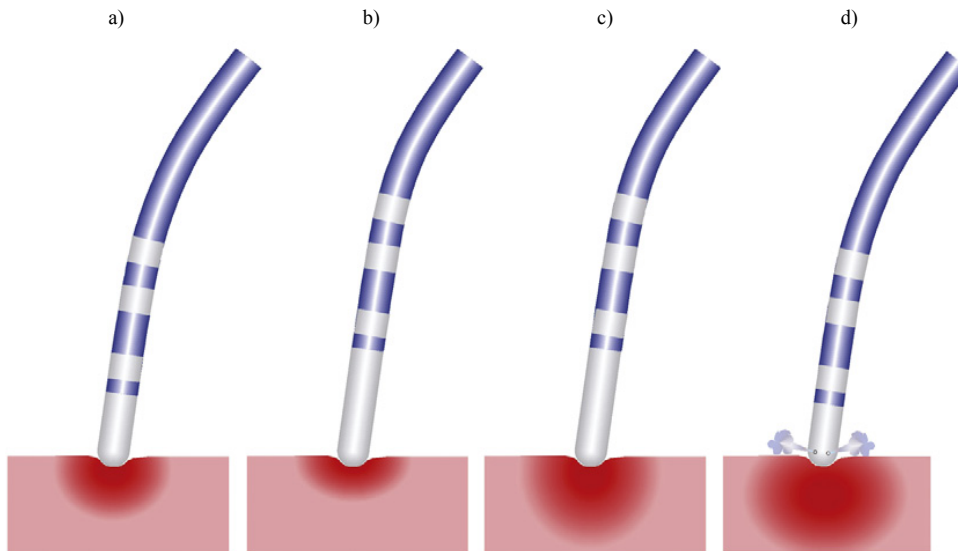


Figure 1.11: Illustration of lesion formation (extension and depth) of different catheter tip sizes: a) lesion created by a 4 mm catheter tip, b) lesion created by a 8 mm catheter tip with 20 W power output, c) lesion created by a 8 mm catheter tip with 50 W power output and d) lesion created by an open irrigated catheter tip of 3.5 mm. Reproduced and modified from [6].

Application of Radiofrequency Ablation Energy

Efficacy of RF ablation is dependent on RF power and application duration but most importantly by the contact of the catheter tip with the cardiac tissue and the cooling effect of blood [6, 49, 69, 70]. Most of RF energy is dissipated into the blood and the measured catheter temperature is lower than tissue temperature, thus limiting lesion formation [6, 49]. Tissue heating, and thus lesion formation, is indicated by an increase of electrode temperature and a fall of measured impedance during ablation [49].

Energy delivery should be titrated to that required to perform permanent lesion avoiding excessive tissue damage like coagulum formation, carbonization and steam popping [6, 49]. Energy titration typically limits RF power to 30-50 W, controlling electrode temperature between 55-70°C and impedance fall between 10-15 ohms [49].

Bigger catheter tip sizes (typically 8 to 10 mm) allow greater energy delivery but most of the energy is dissipated by blood cooling, yielding into lower lesion sizes that requires more generator power compared with smaller tip size catheters, as illustrated in Fig. 1.11(a)–(c) [6, 49]. Cooled-tip catheters aim to prevent overheating of the endocardium by actively cool the catheter tip before temperature increases to coagulation formation (above 70°C), therefore, allowing sufficient RF energy delivery to increase lesion size [6, 49, 71] (see Fig. 1.11(d)). The catheter tip can be cooled by a room temperature liquid flowing through a close circuit within the catheter (close

irrigation) or by a saline solution that emerges through pores in the catheter tip (open irrigation) [6, 49, 71]. However, the temperature of the catheter tip can not be reliably measured and impedance control is further needed for safe operation with cooled-tip catheters [6, 49, 71].

Other Forms of Ablation Energy

Alternative sources of energy for ablation are proposed to improve lesion size and deep, but not all being clinically available. Cryoablation catheters are the main alternative to RF ablation in clinical practice, but do not demonstrate a clear superiority [6, 49]. Other sources of energy are microwaves, laser or ultrasounds but are less used or not yet clinically available [6, 49].

1.6 Scope and Objectives of the Thesis

This thesis aims to contribute in reducing the burden of CVDs from the technical point of view of processing the electrical signals coming from the heart. Especially, the main objective of this thesis is to investigate signal processing techniques of invasive EGM signals that provide useful tools for helping electrophysiologists and technicians in the decision process during ablation procedures or arrhythmia studies. More precisely, the problems addressed in this thesis with their specific aims are:

1. **Signal processing for automatic electroanatomical mapping:** EAM systems play a key role for mapping and ablation of focal VTs. However EAM systems do not include convenient EGM signal processing techniques and the system operator usually needs to modify the measurements during the procedure. This is a very subject-dependent and time-consuming task done during stress situations. Within this specific context, the aim of this thesis is to provide signal processing techniques that allow automatic accurate measurements of relevant EGM signal characteristics for cardiac mapping during ablation interventions using EAM systems. This may help to improve procedure time and reduce measurement variability, which may yield into less risk of the ablation procedures and reduction of VT recurrence rates.
2. **Signal processing for high-density activation mapping during AF:** AM helps to understand the underlying arrhythmia mechanisms. However, during unstable arrhythmias (like AF) sparse electrode catheters or sequential point-by-point EAM systems are not suitable. Therefore simultaneous high-density mapping of AF is desirable. Classically, construction of high-density activation maps rely on the LAT detector accuracy and do not take into consideration the spatial relations between close electrodes. Hence, this thesis aims to explore spatiotemporal signal processing methods for obtaining high-density activation maps which may help in the study of the mechanisms perpetuating AF.

- 3. Signal processing for characterizing AF activity:** Multi-electrode catheters are used for guiding ablation interventions during AF. Therefore, multiple signal processing techniques have been developed to help in the decision process. Most of these techniques rely on activation detection and/or do not take into consideration spatiotemporal features of the multiple acquired signals. This thesis aims to evaluate the causal relations of these multiple sites in order to provide a global view of the fibrillation process and help to interpret such activity during AF.

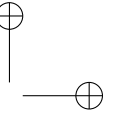
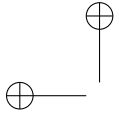
1.7 Document Organization

This document is organized as follows:

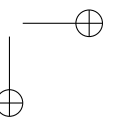
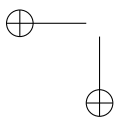
Chapter 2: Electroanatomical Ventricular Activation Mapping: In this chapter the problem of automatic VT AM using current EAM system software is introduced and a method for automatic ventricular AM is presented. The method is evaluated in two clinical scenarios: 1) The first scenario assess the detection performance of the method in a database of focal VT patients by comparing automatic LAT annotations with manual LAT annotations from different experts and 2) a clinical scenario where the ability of the automatic activation maps in identifying the SOO of idiopathic VTs is tested. This chapter is based in the research presented in [72–75]; result of a research collaboration with Hospital Clinic (Barcelona, Spain) and Universitat Pompeu Fabra (Barcelona, Spain) and, in part, of a research stay at Universitat Pompeu Fabra subsidized by MINECO (Spain).

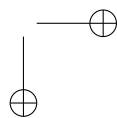
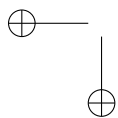
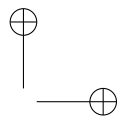
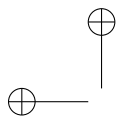
Chapter 3: Spatiotemporal High-Density Atrial Activation Mapping: In this chapter, AM of AF is introduced and a spatiotemporal method for assessing high-density AF activation maps is presented and evaluated. Evaluation of the method is done by comparison with expert manual annotations of high-density invasive open chest surgery data during SR and AF. This chapter is based on the research presented in [76, 77]; result of a research collaboration with Dr. Richard P. M. Houben in a research stay at Applied Biomedical Systems B.V. (Maastricht, The Netherlands) subsidized by MINECO (Spain).

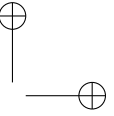
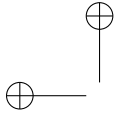
Chapter 4: Causal Characterisation of Atrial Activity: In this chapter, investigation of atrial regularity and interactions during AF is addressed by proposing a linear multi-variate predictability framework. Evaluation and validation of the proposed framework is conducted by a simulation study of different AF complexity patterns and the capabilities of the proposed framework are illustrated using additional real patient data. This chapter is based on the research presented in [78]; result of a research collaboration with Dr. Luca Faes in a research stay at BIOtech Centre, Università Degli Studi di Trento (Trento, Italy) subsidized by MINECO (Spain).



Chapter 5: Final Discussion and Conclusion: Finally, the methods presented in this thesis are discussed and the main limitations are outlined, together with a final conclusion, analysis of the clinical implications and introduction of future extensions of this thesis.







“This world spins from the same
unseen forces that twist our hearts.”
Cloud Atlas by David Mitchell

Chapter 2

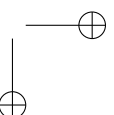
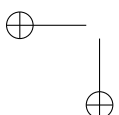
Electroanatomical Ventricular Activation Mapping

2.1 Introduction	2.3.2 Evaluation Protocol
2.1.1 Sequential Electroanatomical Activation Mapping	2.3.3 Results
2.1.2 Methods for Sequential Activation Mapping	2.4 Mapping Performance
2.1.3 Motivation	2.4.1 Idiopathic Outflow Tract Ventricular Arrhythmias
2.2 The Wavelet-Envelope Detector and Delineator	2.4.2 Map Descriptors
2.2.1 Electrogram Signal Pre-processing: the Hilbert Transform	2.4.3 Patient Sample
2.2.2 The Wavelet Transform	2.4.4 Evaluation Protocol
2.2.3 Delineating the Electrogram	2.4.5 Results
2.2.4 Including Spatial Information	2.5 Discussion
2.3 Delineation Accuracy	2.5.1 Algorithm Performance
2.3.1 Testing Database	2.5.2 Clinical Application
	2.5.3 Comparison with Other Methods
	2.5.4 Limitations
	2.6 Conclusion

2.1 Introduction

2.1.1 Sequential Electroanatomical Activation Mapping

The aims of AM are to determine the electrical activation sequence of the heart during an arrhythmia and to identify the mechanism involved on its initiation and mainte-



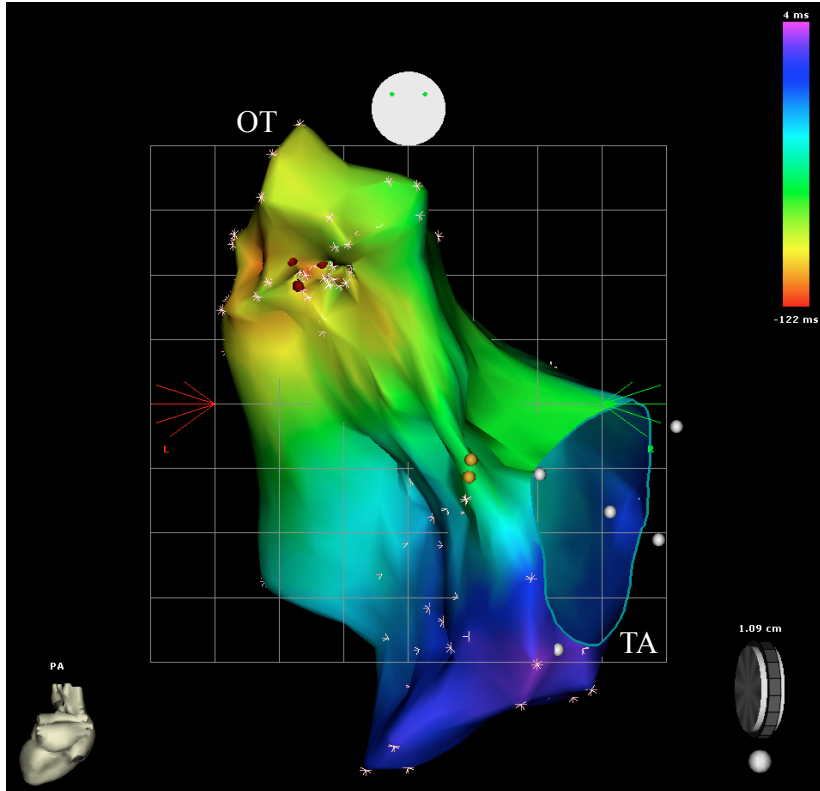


Figure 2.1: Activation map of the RV in posterior-anterior view: focal activation arise from the septal part of the RV outflow tract. LAT is colour-coded from red (earlier) to purple (later). White spheres indicate the location of reference anatomical structure points, red spheres indicate sites of RF delivery, orange spheres indicate HPS points. White crosses indicate acquired EAM points. OT: outflow tract, PA: posterior-anterior, TA: tricuspid annulus.

nance, hence defining the ablation target [6, 79]. This activation sequence is obtained by moving a single or multi-electrode catheter through the cardiac chambers during the clinical arrhythmia. Therefore, this approach is preferably applicable during stable arrhythmias [79], such as focal or macroreentrant tachycardias [6]. In case of focal tachycardia, the earliest activation site (EAS) becomes the ablation target while in macroreentrant tachycardias the ablation focuses on the critical reentrant isthmus [6]. Using an EAM system, the arrhythmia mechanism can be identified by using a colour-coded scale of the activation sequence after acquisition of a sufficient number of mapping points to characterise both anatomy and activation propagation, as illustrated in Fig. 2.1.

During AM using EAM systems, the timing of activation (otherwise known as LAT) is referred to a stable time reference [6, 49, 79, 80]. In case of VT AM, this reference time must be carefully selected from the surface ECG QRS complex [57].

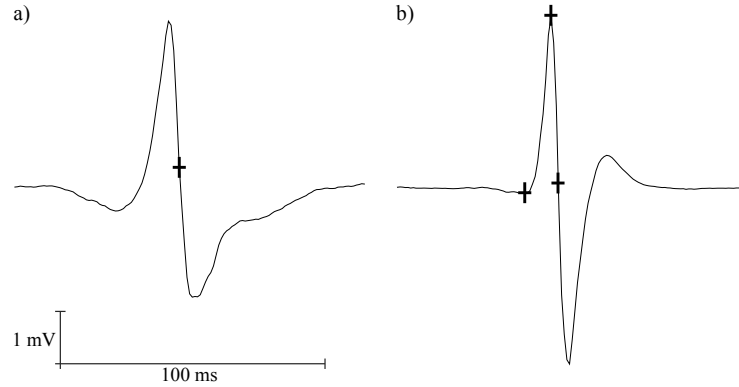


Figure 2.2: LAT measurement surrogates (indicated with black crosses): a) u-EGM maximum negative slope and b) from left to right: b-EGM onset, b-EGM maximal peak and b-EGM maximal slope.

Different characteristics of u-EGM or b-EGM signals can be used for LAT measurement, as introduced before in section 1.5.2. The maximum negative slope (dV/dt) of u-EGM signals (see Fig. 2.2(a)), coincides with the upstroke of the cardiac AP and therefore with the true activation time [55, 56]. However, u-EGMs are not commonly used in the clinical practice because they are prone to be disrupted by other electrical sources such as baseline wander or far-field potentials [6, 54, 57].

On the other hand, common LAT surrogates from b-EGM signals are: 1) the maximal peak of the signal, 2) the maximal slope and 3) the activation onset, defined as a voltage change from baseline of 45° or more at a recording paper speed of 100 mm/s [55]. Those LAT surrogates are illustrated in Fig. 2.2(b). However, there is not an established consensus on these surrogates. The first two can not be reliably estimated in fractionated b-EGMs [49] and the b-EGM onset definition is ambiguous since depends of the used amplitude scale. Nevertheless, the b-EGM onset is considered a better marker for AM using b-EGMs [6].

2.1.2 Methods for Sequential Activation Mapping

Usually, the software in EAM systems locates the maximal peak of the b-EGM signal in a window of interest. Therefore, the EAM system software forces the operator to manually modify the marker if they want to use other LAT surrogate for AM.

Only a few approaches for LAT measurement have been proposed in the bibliography as alternatives to those performed by EAM systems. *El Haddad et al.* proposed an algorithm which heavily filters the b-EGM signals for detecting its onset and end. These landmarks were used as a window for LAT estimation from u-EGMs, and this LAT surrogate is called *slope-hybrid* u-EGM LAT [81, 82], as illustrated in Fig. 2.3. On the other hand, the non-linear energy operator has been proposed for b-EGM LAT identification by *Oesterlein et al.* and tested on simulation data [83].

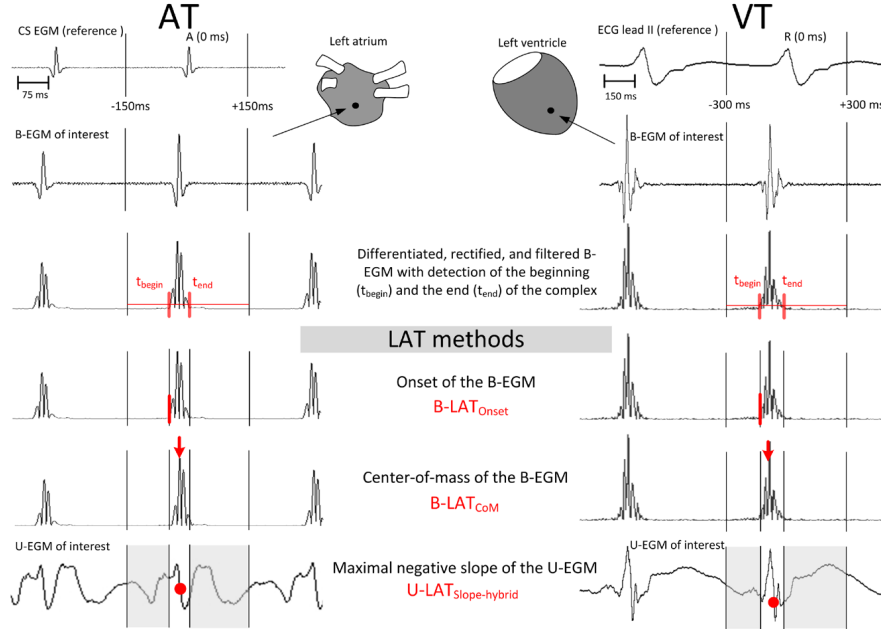


Figure 2.3: Algorithmic LAT measures for AT and VT AM proposed by *El Haddad et al.* [81, 82]. Reproduced from [82]. AT: atrial Tachycardia, CoM: center of mass, CS: coronary sinus, LAT: local activation time, VT: ventricular tachycardia.

2.1.3 Motivation

Estimation of LATs based on the b-EGM onset landmark for AM using EAM systems is a highly manual task performed by the EAM system operator [84]. This LAT identification turns into a very subjective and time-consuming task done in stressing conditions, which can compromise the accuracy of the mapping procedure. This chapter introduces an automatic delineation strategy combining information from the surface ECG and the wavelet decomposition of the b-EGM envelope for LAT computation, with the aim of providing fast and observer-independent activation maps.

2.2 The Wavelet-Envelope Detector and Delineator

2.2.1 Electrogram Signal Pre-processing: the Hilbert Transform

During arrhythmias, b-EGM signals show large morphology variations due to different causes such as complex activation, the relative position between the activation wavefront and the catheter electrodes or the contact of the electrodes with the my-

ocardium [85, 86]. Thus, in order to minimise the influence of b-EGM morphological variations in detection performance, an envelope-based pre-processing step is proposed.

Let an EGM activation $x[n]$ be modelled as a positive valued low-pass signal $e[n]$ modulated by a cosine with modulation frequency ω_m and phase angle ϕ :

$$x[n] = e[n] \cdot \cos(\omega_m n + \phi). \quad (2.1)$$

The envelope $e[n]$ can be extracted by means of the analytic signal of $x[n]$ defined as in [87]:

$$x_a[n] = x[n] + j\check{x}[n], \quad (2.2)$$

where j is the imaginary unit and $\check{x}[n]$ stands for the Hilbert transform of the signal $x[n]$, defined by:

$$\check{x}[n] = \mathcal{H}\{x[n]\} = \frac{1}{\pi} \sum_{k=-\infty}^{\infty} \frac{x[k]}{n-k}, \quad (2.3)$$

which is the convolution of $x[n]$ with an impulse response $h[n] = 1/\pi n$, known as the Hilbert transformer, whose transfer function is

$$H(e^{j\omega}) = \begin{cases} j, & -\pi \leq \omega < 0 \\ -j, & 0 \leq \omega < \pi \end{cases}, \quad (2.4)$$

thus $\check{x}[n]$ is a 90° phase-shifted version of $x[n]$. Therefore the analytic signal $x_a[n]$ represents a frequency-shifted version of the envelope $e[n]$,

$$x_a[n] = e[n] \cdot e^{j\omega_m n}, \quad (2.5)$$

from which the envelope $e[n]$ can be directly obtained, without any previous knowledge of the modulation frequency ω_m or phase angle ϕ , by means of the modulus

$$e[n] = |x_a[n]| = \sqrt{x^2[n] + \check{x}^2[n]}. \quad (2.6)$$

Figure 2.4 shows representative examples of different EGM morphologies and the computation of its envelope, yielding to a positive-peak shape of the resulting pre-processed signal.

2.2.2 The Wavelet Transform

The continuous wavelet transform (CWT) is the decomposition of a signal $x(t)$ into a set of basis functions, which are created by dilation and translation of a single prototype wavelet function $\psi(t)$ [88]. Therefore, the CWT can be written as:

$$W_a x(b) = \frac{1}{\sqrt{a}} \int_{-\infty}^{+\infty} x(t) \psi\left(\frac{t-b}{a}\right) dt, a > 0, \quad (2.7)$$

where a and b stand for the expansion and translation factors, respectively. The CWT can be interpreted as the filtering of $x(t)$ with an impulse response $h(t) = \psi(-t/a)/\sqrt{a}$.

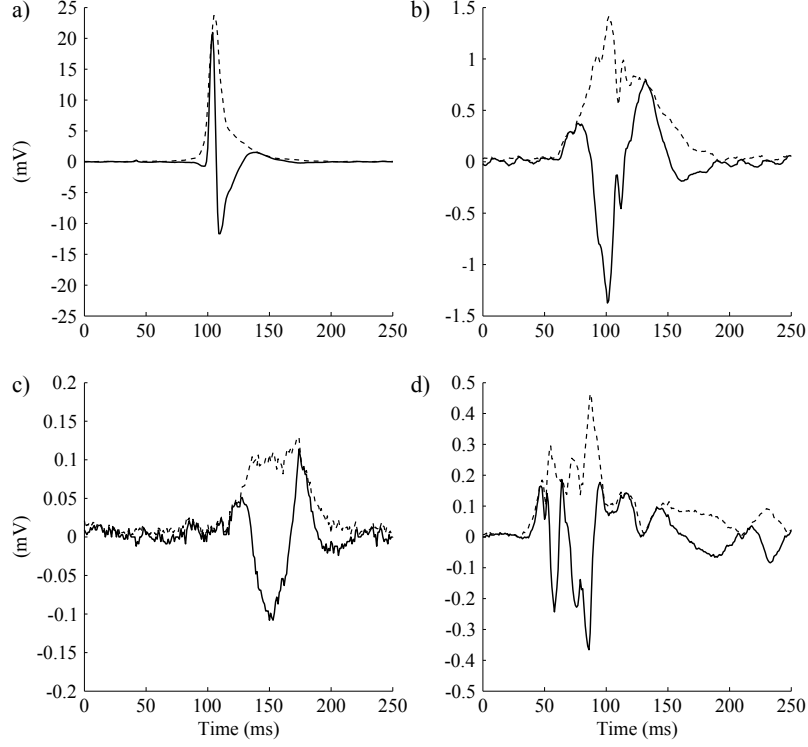


Figure 2.4: Examples of b-EGM activations (bold line) and its envelope $e[n]$ (dashed line) in: a) Normal b-EGM, b) noisy wide b-EGM, c) low amplitude b-EGM and d) fractionated b-EGM.

Hence, the expansion factor a modifies the bandwidth of the signal representation in the CWT domain, i.e., the larger is a , the wider is $\psi(t/a)$ and more information about lower frequencies is included in the CWT signal representation and vice versa.

If the prototype wavelet $\psi(t)$ is the derivative of a smoothing function $\theta(t)$, then (2.7) can be written as [89]:

$$W_a x(b) = -a \left(\frac{d}{db} \right) \int_{-\infty}^{+\infty} x(t) \theta_a(t-b) dt, \quad (2.8)$$

where $\theta_a(t) = (1/\sqrt{a})\theta(t/a)$ is the scaled version of the smoothing function. Therefore, the CWT at scale a is proportional to the derivative of the convolution of $x(t)$ with a smoothing impulse response at scale a . Then, the zero-crossings of the CWT correspond to local maxima or minima of the smoothed signal at different scales, and maximum or minimum values in the CWT are respectively associated with maximum upward or downward slopes in the smoothed signal.

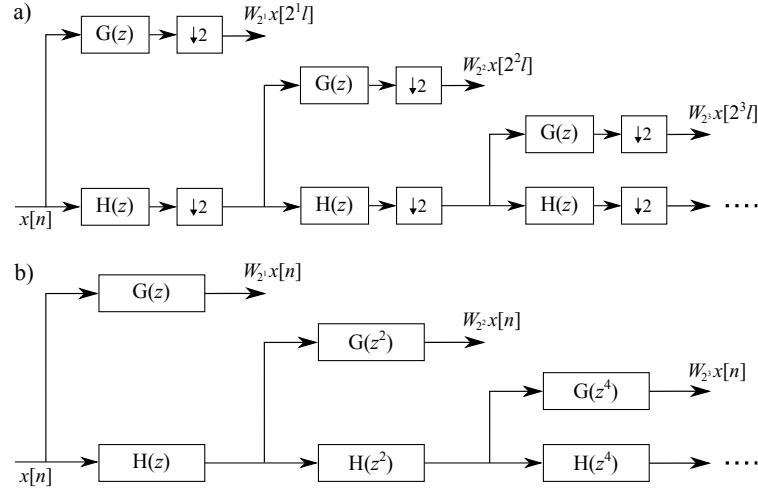


Figure 2.5: Implementation of the DWT: a) Mallat's algorithm analysis filter-bank, b) *algorithme à trous* analysis filter-bank. $G(z)$ and $H(z)$ are low-pass and high-pass FIR filters, respectively.

The “Dyadic” Discrete Wavelet Transform

The CWT is highly redundant because the wavelet decomposition coefficients are computed for each value of the expansion factor a . Therefore, for computer-based implementation purposes, a discrete signal $x[n]$ is considered and the CWT can be discretised by means of the called dyadic discrete wavelet transform (DWT). The dyadic DWT discretises the time-scale plane parameters a and b following a dyadic sampling grid ($a = 2^m$, $b = 2^m l$; $m \in \mathbb{N}$, $l \in \mathbb{Z}$). Therefore, the resulting basis function is:

$$\psi_{m,l}[n] = 2^{-m/2} \psi[2^{-m}n - l]. \quad (2.9)$$

Mallat and *Zhong* [89] demonstrated that the DWT is equivalent to an octave filter-bank that can be implemented as a cascade of identical cells of low-pass and high-pass finite impulse response (FIR) filters followed by decimation stages as illustrated in Fig. 2.5(a). The signal $x[n]$ can be reconstructed from the wavelet coefficients $W_{2^m}x[2^m l]$ and the low-pass residual using the reconstruction filter-bank. The reconstruction filter-bank is not shown because it is not relevant for the application aim.

The *Mallat's algorithm* turns the signal representation time-variant due to the reducing temporal resolution of the wavelet coefficients as scale increases. The decimation stages can be removed using the *algorithme à trous* by interpolating the filter impulse response of the previous stage (see Fig. 2.5(b)), thus keeping the time-invariance representation of the signal and the temporal resolution of the different scales while preserving the sampling rate [90]. Using the *algorithme à trous*, the equivalent fre-

quency response of the m th scale can be written as:

$$Q_m(e^{j\omega}) = \begin{cases} G(e^{j\omega}), & m = 1 \\ G(e^{j2^{m-1}\omega}), \prod_{l=0}^{m-2} H(e^{j2^l\omega}), & m \geq 2 \end{cases}, \quad (2.10)$$

where $G(e^{j\omega})$ and $H(e^{j\omega})$ are the frequency response of the impulse response functions $g[n]$ and $h[n]$ associated with the low-pass and high-pass filters of the filter-bank respectively.

The Prototype Wavelet

The frequency response at each scale shown in equation (2.10) depends on the used prototype wavelet function $\psi(t)$. A function can be considered a wavelet prototype if it forms an orthonormal basis on $L^2(\mathbb{R})$ through dilation and translation [88].

On the other hand, the interesting properties derived from equation (2.8) combined with the positive-peak shape of the preprocessed b-EGM signal explained in section 2.2.1, allow to represent the signal peaks as zero-crossings and its upward and downward slopes as maximum or minimum values in the wavelet domain.

Thus, inspired in a similar problem with surface ECG signal detection and delineation [91], the selected prototype wavelet $\psi(t)$ corresponds to the derivative of a quadratic spline, whose Fourier transform is of the form:

$$\Psi(\Omega) = j\Omega \left(\frac{\sin(\frac{\Omega}{4})}{\frac{\Omega}{4}} \right)^4, \quad (2.11)$$

that can be interpreted as the derivative of the convolution of four rectangular pulses, i.e. the derivative of a smoothing function. Figure 2.6(a) shows the used wavelet prototype $\psi(t)$ and its corresponding smoothing function $\theta(t)$. Therefore, the corresponding filters $H(e^{j\omega})$ and $G(e^{j\omega})$ to implement the DWT in (2.10) are [91, 92]:

$$\begin{aligned} H(e^{j\omega}) &= e^{j\omega/2} \left(\cos \frac{\omega}{2} \right)^3 \\ G(e^{j\omega}) &= 4j e^{j\omega/2} \left(\sin \frac{\omega}{2} \right), \end{aligned} \quad (2.12)$$

which correspond to the following FIR filter impulse responses:

$$\begin{aligned} h[n] &= \frac{1}{8} \{ \delta[n+2] + 3\delta[n+1] + 3\delta[n] + \delta[n-1] \} \\ g[n] &= 2\{ \delta[n+1] - \delta[n] \}. \end{aligned} \quad (2.13)$$

Using the *algorithme à trous* and equations (2.10) and (2.12), the frequency response of the first four scales for an interpolation sampling frequency of 1000 Hz are

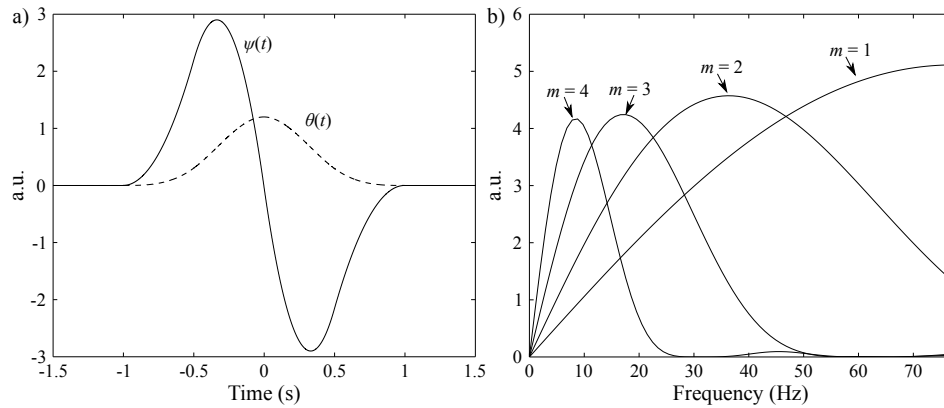


Figure 2.6: Implemented wavelet transform: a) prototype wavelet $\psi(t)$ and smoothing function $\theta(t)$ and b) equivalent frequency responses of the DWT using the prototype wavelet $\psi(t)$ at scales 2^m , $m = 1 \dots 4$ for 1000 Hz interpolation sampling frequency.

those presented in Fig. 2.6(b). These transfer functions behave as low-pass differentiators and, as the analytic filters have linear phase [91], the delay of the filter output can be compensated in order to preserve synchronisation with the original signal. Therefore, the implementation of the DWT using this wavelet prototype can be considered as a low-pass differentiator filter-bank.

2.2.3 Delineating the Electrogram

The algorithm is based in the outcomes of a combined surface ECG and EGM signal analysis strategy, as illustrated in Fig. 2.7.

Reference Beat QRS Detection and Delineation

This detection step (illustrated in bottom branch of Fig. 2.7) aims to identify the reference beat and provide a reference window for the EGM delineation algorithm (illustrated in top branch of Fig. 2.7).

A single-lead wavelet-based QRS detector and delineator was applied on each surface ECG lead [91] and a global multilead QRS delineation is obtained using the rule algorithm described in [93]. These rules were designed to include the spatiotemporal information of each ECG lead while avoiding errors and miss-detections, obtaining a single set of temporal marks that are in agreement across the recorded leads.

This multilead delineation process identifies three time instants for each lead l and beat b : 1) the onset of the b th QRS complex $n_o^{l,b}$, 2) the fiducial point of the b th QRS complex $n_f^{l,b}$ (usually related with the R wave) and 3) the end of the b th QRS complex $n_e^{l,b}$.

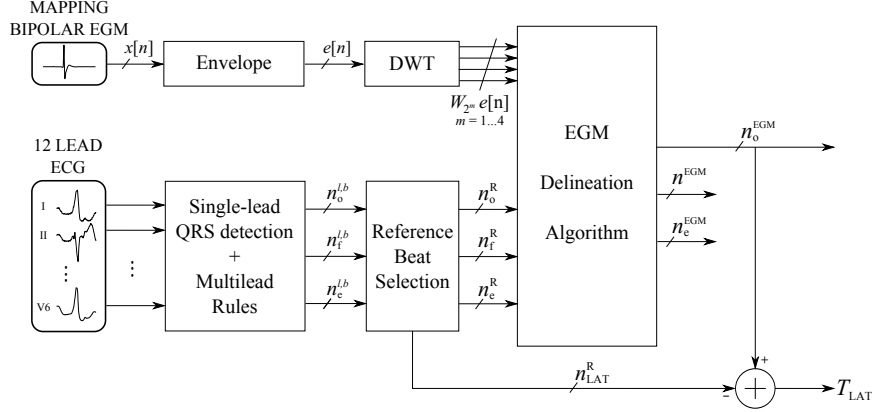


Figure 2.7: Block diagram of the wavelet-envelope detector and delineator: the EGM delineation algorithm uses the DWT of the b-EGM activation envelope (top branch) centred within a window obtained from the QRS delineation of the reference beat (bottom branch). T_{LAT} stands for the computed LAT value.

The nearest QRS fiducial point to the reference time selected by the EAM system operator, defines the reference beat fiducial point n_f^R . This point and its related onset and end time instants (n_o^R and n_e^R) describe the reference beat. Therefore, the basic searching window S spans from the onset to end time points of the reference beat (marked as blue dotted vertical lines in each panel of Fig. 2.8)

Electrogram Delineation Algorithm

After QRS detection and delineation of the reference beat, an EGM delineation strategy is applied to the DWT of the b-EGM signal envelope $e[n]$.

The strategy is inspired on the multi-scale approach used in [91], whose objective is to locate a set of local maxima and minima across the different scales of the DWT, called maximum modulus lines (MML) [94]. First, the highest peak of the EGM signal envelope is located, defining the “*main activation wave*”. Since the EGM activation envelope is a positive peaked signal, the main activation wave is related with the zero-crossings between a pair of positive and negative MMLs in the DWT domain [91].

A local maximum or minimum value at scale 2^m can be considered a part of an MML if it is higher than a threshold defined as:

$$\epsilon_{\text{EGM}}^m = \epsilon_m \sqrt{\frac{1}{L} \sum_{n \in S} (W_{2^m} e[n])^2}, m = 1 \dots 4, \quad (2.14)$$

where $\epsilon_4 = 3/4$ and $\epsilon_m = 3/8, m = 1 \dots 3$, are the threshold scaling factors of each DWT scale and L stands for the length of the window S . Given the low-pass frequency content of the EGM envelope, most of their frequency components are likely to lie at scales 2^4 and 2^3 (see Fig. 2.6(b)).

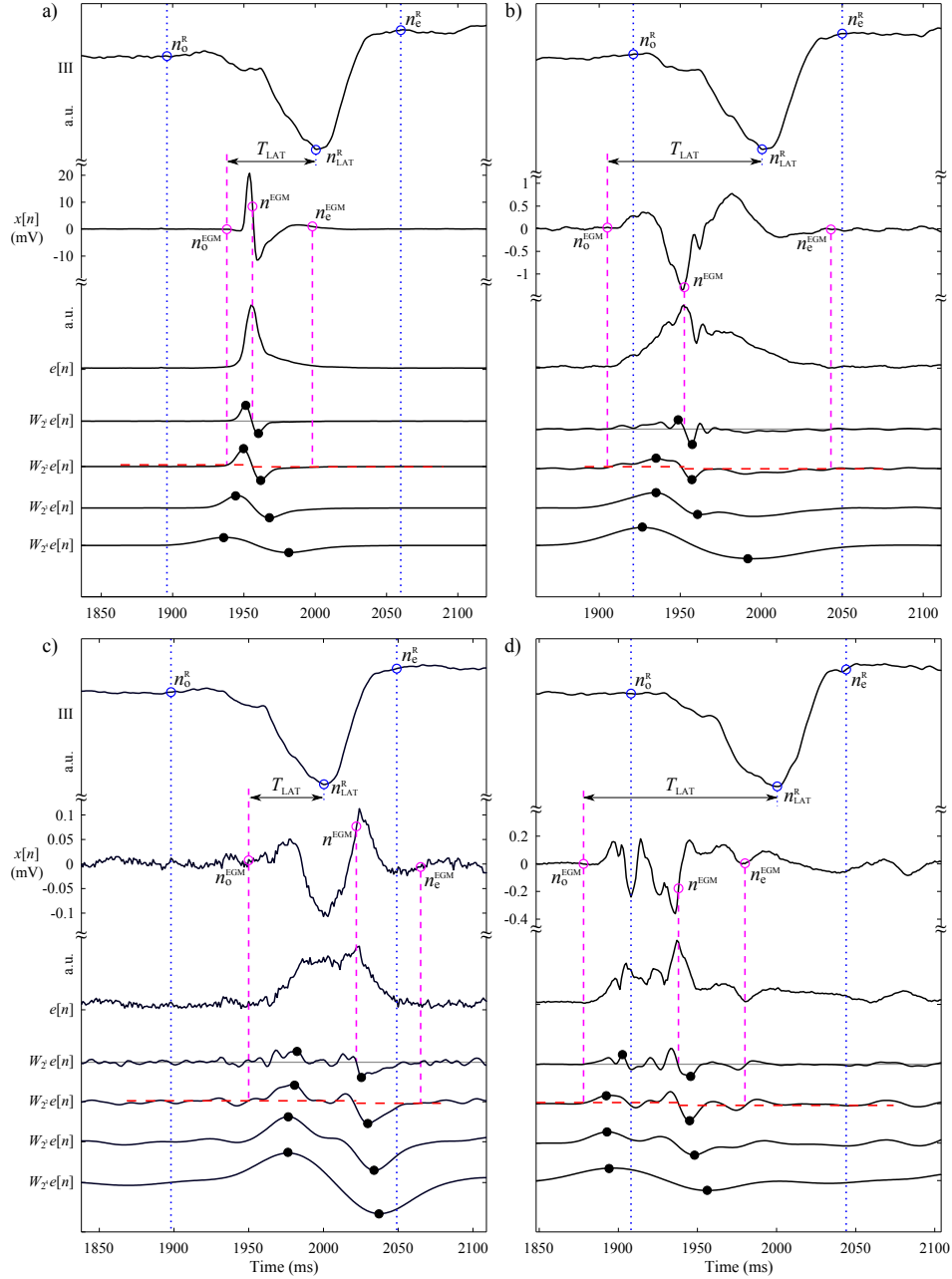


Figure 2.8: LAT detection in representative b-EGM morphologies from the same patient during PVCs: a) normal EGM, b) noisy wide EGM, c) low amplitude EGM and d) fractionated EGM. Each panel shows, centred at the reference beat and from top to bottom: ECG lead III, mapping catheter EGM signal $x[n]$, its envelope $e[n]$ and the four first scales of the DWT $W_{2^m}e[n]$, $m = 1 \dots 4$. Black dots indicate MMLs. Blue dotted vertical lines show the search window S . Gray line at scale 2^1 indicates zero level. Red dashed lines at scale 2^2 indicate detection thresholds ξ_o^{EGM} and ξ_e^{EGM} . Purple dashed vertical lines connect the DWT characteristic landmarks with their annotations: the *main activation wave* n^{EGM} and its onset and end points n_o^{EGM} and n_e^{EGM} , respectively. T_{LAT} stands for the computed LAT value.

An EGM activation can occur outside the QRS complex boundaries of the reference beat, especially during PVCs in focal arrhythmias [6]. Therefore, S is extended in both ends by 30 ms defining the extended window S' . Within S' , those local maxima and minima values exceeding the threshold $\varepsilon_{\text{EGM}}^4$ defined by (2.14) at scale 2^4 were selected.

If S' was inadequate for finding at least a pair of local maximum-minimum (LMM) at scale 2^4 , a new searching procedure was performed by extending 30 ms S' , forward or backward depending on the sign of the already detected local maxima and minima, and applying a threshold reduction by 50% of the previous value. If there was no success in the LMMs searching procedure at scale 2^4 , then scale 2^3 was used for LMM detection in combination with the threshold $\varepsilon_{\text{EGM}}^3$ defined by (2.14). This scale includes higher frequency components of the signal than scale 2^4 but it is usually noisier.

Once LMM pairs were located at the appropriate detection scale (either 2^4 or 2^3), MML searching across the rest of the scales was performed by connecting the local maxima and minima detected using their corresponding thresholds defined by (2.14), followed by rejection of those isolated and redundant lines in the same way as in [91].

When a single zero-crossing between a pair of positive and negative MMLs at scale 2^1 is present, it is marked as the main activation wave n^{EGM} (see Fig. 2.8(a)–(b)). In case that more than one zero-crossings are found, the main activation wave n^{EGM} is determined by selecting among the possible pairs of LMM candidates, the zero-crossing at scale 2^1 whose associated LMM pair presents higher maximum-to-minimum value. The result of this procedure can be seen in Fig. 2.8(c)–(d).

Once the main activation wave is detected, the next step of the algorithm is to delineate the onset and end points. The algorithm starts from the formerly detected main activation wave n^{EGM} , which will be flanked by a pair of positive and negative MMLs at scale 2^2 . Local maximum or minimum values at scale 2^2 are related to up and down slopes of the EGM signal envelope, respectively. Therefore, the EGM activation onset and end points, n_o^{EGM} and n_e^{EGM} , are detected as the single first sample below or above a threshold defined as:

$$\xi_o^{\text{EGM}} = \gamma_o \cdot \max(W_{2^2}e[n]), n \in S_o, \quad (2.15)$$

$$\xi_e^{\text{EGM}} = \gamma_e \cdot \min(W_{2^2}e[n]), n \in S_e, \quad (2.16)$$

where $\gamma_o = 0.1$ and $\gamma_e = 0.05$ are the proportional threshold factors. Those thresholds are computed within two windows, S_o and S_e , spanning 30 ms before and after the main activation wave n^{EGM} , respectively. An example of this delineation process is shown in Fig. 2.8(a). In order to protect the method against fractionated and noisy EGM activations, as those shown in Fig. 2.8(b)–(d), the algorithm only considers those candidate samples lying within the biggest upward slope at scale 2^4 . This scale is related with the overall shape of the EGM activation envelope.

Computation of the Local Activation Time

Sequential AM requires an stable time reference for LAT computation. This is usually identified as the maximum or minimum deflection of the QRS complex from the stablest ECG lead during mapping [6, 49, 79, 80]. Therefore, for each mapping point, the

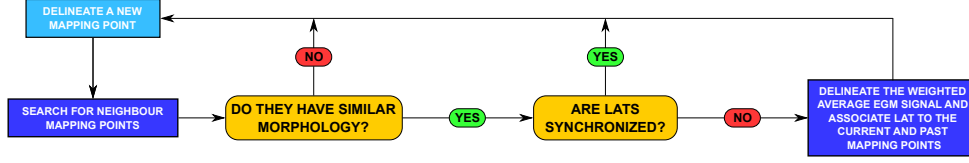


Figure 2.9: Decision diagram of the spatial consistency algorithm.

LAT value T_{LAT} is defined as the time difference between the QRS reference time n_{LAT}^R and the onset of the b-EGM activation from the mapping catheter n_o^{EGM} , as illustrated in Fig. 2.8:

$$T_{LAT} = n_o^{EGM} - n_{LAT}^R. \quad (2.17)$$

2.2.4 Including Spatial Information

Rationale

When mapping focal arrhythmias, the EAS becomes the area of interest (AOI) and thus the ablation target [6]. Therefore, a high number of close mapping points are usually acquired in order to identify the EAS. However, the delineation algorithm introduced in section 2.2.3 analyses each mapping point separately, without taking profit of the existing spatiotemporal relations between the already acquired mapping points.

Activation Spatial Consistency Algorithm

The aim of this algorithm is to exploit the morphological similarities of spatially close mapping points for obtaining reliable and coherent activation patterns. This algorithm makes a difference in areas with high-density of mapping points. The decision diagram illustrating this algorithm is shown in Fig. 2.9.

The algorithm is applied after delineation of the b-EGM at each i th mapping point, $x_i[n]$. Each mapping point has a position vector $\mathbf{r}_i = [r_{x_i}, r_{y_i}, r_{z_i}]^T$ given by the EAM system. Then, from the already acquired mapping points $x_k[n]$, $k = 1 \dots i$, those located within a neighbourhood defined as:

$$N_i = \{k ; \|\mathbf{r}_i - \mathbf{r}_k\|_2 \leq 6 \text{ mm}\}, \quad (2.18)$$

were considered as *neighbour cluster candidate* points ($k \in N_i$).

Next, the morphology similarity of these *neighbour cluster candidate* points is quantified by means of the normalized cross-covariance function:

$$C_{i,k}[m] = \frac{\sum_{n=-L/2}^{L/2} (x_i[n] - \bar{x}_i)(x_k[n+m] - \bar{x}_k)}{\sqrt{\sum_{n=-L/2}^{L/2} (x_i[n] - \bar{x}_i)^2 \sum_{n=-L/2}^{L/2} (x_k[n] - \bar{x}_k)^2}} \quad (2.19)$$

where L is the window length spanning 70 ms before and after the estimated QRS onset and end points, \bar{x}_i and \bar{x}_k are the mean values of $x_i[n]$ and $x_k[n]$, respectively, and m stands for the lag between signals. The delay between signals $\tau_{i,k}$ is obtained by maximizing (2.19):

$$\tau_{i,k} = \arg \max_m \{C_{i,k}[m]\}. \quad (2.20)$$

Then, the cluster of neighbour and morphologically similar points is defined as:

$$M_i = \{k \in N_i ; C_{i,k}[\tau_{i,k}] \geq 0.85 \ \& \ \tau_{i,k} \leq \pm 10 \text{ ms}\}. \quad (2.21)$$

All signals from the cluster points $x_k[n], k \in M_i$, were aligned with respect to $x_i[n]$ using the delay $\tau_{i,k}$ in order to check the LAT agreement between adjacent points. The algorithm considers that the current mapping point is consistently annotated if the difference between its LAT with the median LAT of the rest of mapping points in M_i is below ± 2 ms. If this condition is not fulfilled, a weighted average EGM signal $x_{w,i}[n]$ is computed as follows:

$$x_{w,i}[n] = \frac{\sum_{k \in M_i} w_{i,k} \cdot x_k[n - \tau_{i,k}]}{\sum_{k \in M_i} w_{i,k}}, \quad (2.22)$$

where $w_{i,k}$ stands for the weights for each cluster signal $x_k[n]$, defined as:

$$w_{i,k} = \frac{C_{i,k}[\tau_{i,k}] - 0.85}{1 - 0.85}, k \in M_i. \quad (2.23)$$

Finally, this weighted averaged EGM signal $x_{w,i}[n]$ is delineated with the same algorithm explained in section 2.2.3. The resulting onset, end and main activation wave landmark times, $n_{o,i}^{\text{EGM}w}$, $n_{e,i}^{\text{EGM}w}$ and $n_i^{\text{EGM}w}$, respectively, are associated to the current mapping point and a reliability value of the new mark is assigned as the median value of $C_{i,k}[\tau_{i,k}], k \neq i$.

For the rest of the clustered points in M_i , their single-point-computed landmarks are modified by correcting $n_{o,i}^{\text{EGM}w}$, $n_{e,i}^{\text{EGM}w}$ and $n_i^{\text{EGM}w}$ with the corresponding delay $\tau_{i,k}$. This landmark modification is performed except if the same point had been previously assigned to another cluster with a greater maximum covariance than the current $C_{i,k}[\tau_{i,k}]$. Figure 2.10 illustrates an application example of this process.

2.3 Delineation Accuracy

To evaluate the proposed wavelet-envelope EGM detector and delineator, its accuracy in the identification of the b-EGM signal onset is assessed.

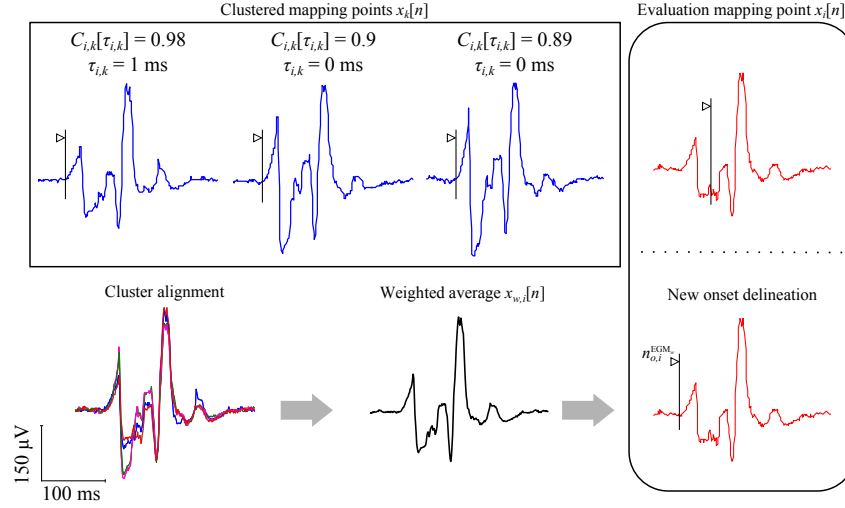


Figure 2.10: Application example of the spatial consistency algorithm on a fractionated, low amplitude b-EGM: evaluation point $x_i[n]$ (red trace) is paired with three clustered mapping points $x_k[n]$ (blue traces). A weighted averaged EGM $x_{w,i}[n]$ is obtained (black trace) after alignment and annotation consistency checking. Finally, a new activation onset $n_{o,i}^{EGM}$ is identified and reassigned to $x_i[n]$. Activation onsets are indicated with black vertical lines pointed by a triangle.

2.3.1 Testing Database

The studied database is composed of 10 patients with idiopathic VAs and non-tolerated PVC beats whose were admitted for ablation procedure at Hospital Clínic (Barcelona, Spain). All patients signed their written informed consent form and the study was approved by the Local Ethics Committee.

From those patients, 14 electroanatomical maps (9 RV and 5 LV maps) were studied. Each of these maps were acquired using the CARTO 3 system (*Biosense Webster, Inc., Diamond Bar, CA, USA*). For each patient and map, different number of mapping points were acquired depending on the electrophysiological protocol, large enough to have sufficient anatomical and electrical information to support the clinical decision.

The total number of mapping points is 1982 (142 ± 60 points/map). Each mapping point includes 12-lead surface ECG signals and b-EGM signals from a 4-pole, 3.5 mm irrigated tip *NaviStar Thermocool* catheter (*Biosense Webster, Inc., Diamond Bar, CA, USA*). For mapping and ablation purposes, the distal EGM signal from the catheter was used. Those signals were acquired point-by-point with 1 kHz sampling frequency during 2.5 s, assuring stable contact of the catheter tip with the myocardial wall and has at least one PVC beat in the recording excerpt matching the clinical VA. The CARTO system stores the signal within a window spanning from 2 s before to 0.5 s after the fiducial point of the PVC beat of interest at the reference ECG lead. The b-EGM signals were band-pass filtered between 16 and 500 Hz with a 50 Hz power-line suppression notch filter.

Table 2.1: Details of the delineation accuracy assessment database. LV: Left ventricle, LVOT: Left ventricle outflow tract, On: available *on-procedure* manual annotations, Off-1: available *off-procedure* manual annotation from expert 1, Off-2: available *off-procedure* manual annotation from expert 2, RV: Right ventricle. N/A: Not applicable.

Patient (#)	Map (#)	Location	Mapping points (#)	RF applications (#)	Available manual annotation sets
1	1	RV	128	12	On, Off-1, Off-2
	2	LV	110	N/A	On, Off-1, Off-2
2	3	RV	155	5	On, Off-1
3	4	LV	179	10	On, Off-1, Off-2
4	5	RV	204	2	On, Off-1, Off-2
5	6	RV	230	1	On, Off-1, Off-2
	7	LV	49	N/A	On, Off-1
6	8	RV	193	2	On, Off-1, Off-2
7	9	RV	156	1	On, Off-1, Off-2
8	10	RV	181	3	On, Off-1, Off-2
9	11	RV	192	10	On, Off-1, Off-2
	12	RV	81	N/A	On, Off-1
10	13	LV	87	21	On, Off-1
	14	LVOT	37	N/A	On, Off-1

Activation maps were generated by the EAM system operator which manually annotated each EGM signal onset during the intervention. The EAS was identified and RF energy was delivered until termination of the arrhythmia.

These manual annotations obtained during the intervention (referred here as “*on-procedure*” annotation set) represent the annotation accuracy currently achieved during the procedure. However, they may not be appropriate as a reference annotation set as they are obtained during stressing conditions. Therefore, a second type of annotations from two other experts (blind to the *on-procedure* annotation set) were obtained after the intervention with no time limitation (referred here as “*off-procedure*” annotation set 1 and 2). Table 2.1 summarizes the characteristics of the database.

2.3.2 Evaluation Protocol

The proposed wavelet-envelope EGM detector and delineator was evaluated against the different annotation sets available in the studied database. Due to the absence of a systematic well-established rule of LAT measurement for AM, the manual *off-procedure* annotation sets were considered as the reference (gold standard) for evaluation. The annotations performed during the procedure (*on-procedure* annotation set) were also evaluated with respect to the *off-procedure* annotation sets, being a reference for performance comparison.

Due to expert availability, annotations performed by both experts were available only in 9 maps (see Table 2.1). In those maps with two available annotations, the average value between both expert annotation sets were computed and labelled as “*averaged off-procedure*” annotation set, which serves as “*gold standard*”.

Errors between annotation sets were shown as mean \pm standard deviation (SD). Due to the sequential nature of LATs (i.e. from earliest to latest activated point) and in order to estimate the agreement in the sequences of activations obtained with the different LAT annotations, Spearman’s rank correlation ρ_s was computed. Additionally Lin’s concordance correlation factor ρ_c [95] and Bland-Altman analysis [96] were used for assessing agreement between the different LAT annotation sets. A p -value ≤ 0.05 was considered as a threshold for statistical significance.

Additionally, annotation errors were evaluated with respect to: 1) a qualitative accuracy scale and 2) the signal voltage amplitude. On one hand, inspired in the accuracy scale proposed by *El Haddad* et al. [81], annotations were classified as: 1) *Highly accurate* annotations (error $\leq \pm 5$ ms), 2) *accurate* annotations (error $\leq \pm 10$ ms) and *inaccurate* annotations (error $> \pm 10$ ms). On the other hand, errors were studied depending on the signal voltage using the standard b-EGM voltage thresholds for: healthy tissue ($V \geq 1.5$ mV), scar border-zone (BZ) tissue ($1.5 \text{ mV} > V \geq 0.5$ mV) and scar core-zone (CZ) tissue ($V < 0.5$ mV) [49].

2.3.3 Results

Double Expert Assessment

The error in LAT estimation by the proposed algorithm compared with the evaluation reference is shown in the third column of Table 2.2. The automatic annotation error is 1.20 ± 10.72 ms from 1573 LAT measures. Thus, automatic delineation provides slightly later LATs than the reference. Moreover, high correlation values ($\rho_s = 0.94$ and $\rho_c = 0.93$, $p < 0.05$ both) indicate high agreement with the evaluation reference (see fourth and fifth columns of Table 2.2).

Evaluation results of the *on-procedure* annotation set are shown in columns six to eight of Table 2.2 for comparison purposes. The error is -2.80 ± 6.01 ms, thus provides slightly earlier LATs than the reference. Additionally, it has higher correlation with the reference than the automatic annotations ($\rho_s = 0.97$ and $\rho_c = 0.97$, $p < 0.05$ both).

The inter-expert variability can be considered as a lower bound for comparison, since an algorithm having smaller error than the inter-expert variability could mean that it is over-adapted to one of the experts. Columns nine to eleven of Table 2.2 show the inter-expert variability results. The low difference in LAT annotation (-0.01 ± 5.44 ms) and high correlation values ($\rho_s = 0.98$ and $\rho_c = 0.98$, $p < 0.05$ both) indicate a high level of agreement between experts in the same conditions (*off-procedure* annotations).

Figure 2.11 shows scatterplots for Lin’s concordance correlation factor ρ_c (top panels) and Bland-Altman plot analysis (bottom panels) for the error (Fig. 2.11(a)–(b))

Table 2.2: Double expert assessment of the LAT error and inter-expert difference (mean \pm SD) by electroanatomical; and Spearman's rank correlation ρ_s and Lin's concordance correlation factor ρ_c .

Map (#)	Points (#)	Automatic LATs			<i>On-procedure</i> LATs			Inter-expert		
		error (ms)	ρ_s	ρ_c	error (ms)	ρ_s	ρ_c	difference (ms)	ρ_s	ρ_c
1	128	-0.09 ± 6.85	0.97*	0.97*	-3.22 ± 5.97	0.98*	0.97*	-2.20 ± 4.11	0.99*	0.99*
2	110	-0.36 ± 8.03	0.91*	0.92*	-3.18 ± 4.63	0.96*	0.95*	-0.93 ± 3.69	0.97*	0.98*
4	179	-0.26 ± 6.25	0.80*	0.85*	-3.15 ± 4.28	0.89*	0.87*	-1.22 ± 3.72	0.94*	0.93*
5	204	-0.64 ± 9.01	0.94*	0.95*	-6.61 ± 7.55	0.96*	0.93*	-1.35 ± 3.37	0.99*	0.99*
6	230	1.18 ± 7.82	0.92*	0.94*	0.37 ± 3.78	0.98*	0.98*	-0.31 ± 3.93	0.97*	0.98*
8	193	4.04 ± 10.62	0.91*	0.89*	-2.26 ± 6.02	0.95*	0.96*	-0.97 ± 3.11	0.98*	0.99*
9	156	4.12 ± 12.07	0.85*	0.82*	-3.12 ± 6.24	0.94*	0.93*	-1.01 ± 3.40	0.98*	0.98*
10	181	3.29 ± 11.17	0.96*	0.94*	-3.26 ± 4.61	0.98*	0.98*	-0.58 ± 2.70	0.99*	$\sim 1^*$
11	192	-0.92 ± 17.32	0.90*	0.90*	-1.59 ± 6.94	0.96*	0.98*	7.24 ± 9.66	0.94*	0.94*
Total	1573	1.20 ± 10.72	0.94*	0.93*	-2.80 ± 6.01	0.97*	0.97*	-0.01 ± 5.44	0.98*	0.98*

* indicates p -value ≤ 0.05

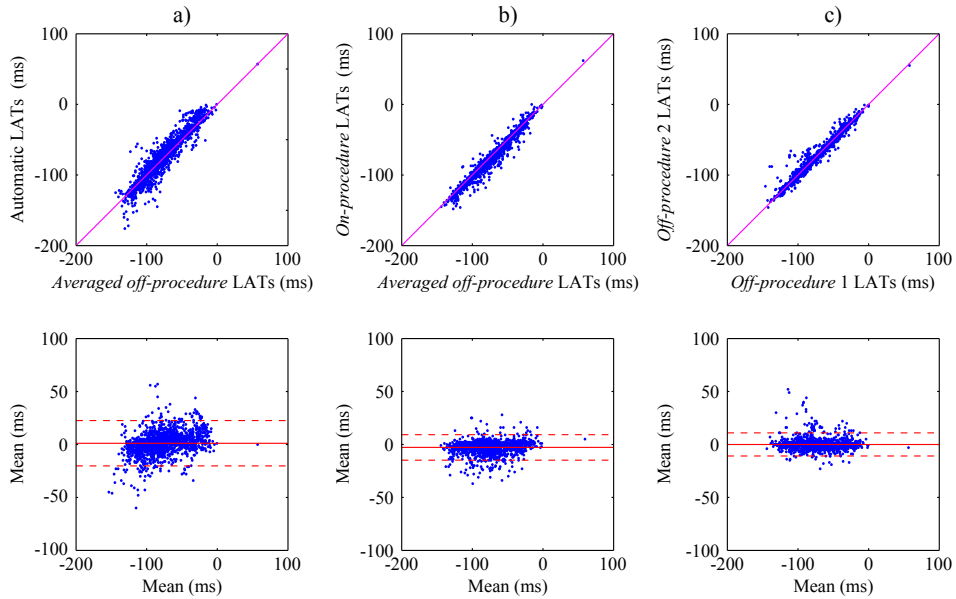


Figure 2.11: Boxplot for Lin's concordance correlation factor ρ_c analysis and Bland-Altman plot of the double expert assessment: a) automatic LATs error assessment, b) manual *on-procedure* LATs error assessment and c) inter-expert variability. Top panels show scatterplot for ρ_c computation (pink line indicates the unitary slope) and bottom panels show the Bland-Altman plot (red continuum line indicates mean error/difference and red dashed lines indicate mean \pm 2 SD of the error/difference).

Table 2.3: Accuracy classification of automatic and *on-procedure* annotation sets compared with the averaged *off-procedure* annotation set.

	Automatic (%)	<i>On-procedure</i> (%)
Highly accurate	52	74
Accurate	24	16
Inaccurate	24	10

Table 2.4: Double expert assessment of LAT error and inter-expert difference (mean \pm SD) by EGM voltage amplitude; and Spearman's rank correlation ρ_s and Lin's concordance correlation factor ρ_c .

Voltage	Points (#)	Automatic LATs			<i>On-procedure</i> LATs			Inter-expert		
		error (ms)	ρ_s	ρ_c	error (ms)	ρ_s	ρ_c	difference (ms)	ρ_s	ρ_c
Normal	1102	4.55 ± 7.72	0.96^*	0.95^*	-3.17 ± 5.98	0.98^*	0.97^*	-0.12 ± 4.91	0.98^*	0.98^*
BZ	260	-3.11 ± 8.55	0.96^*	0.95^*	-2.30 ± 6.38	0.98^*	0.97^*	-0.15 ± 4.28	0.99^*	0.99^*
CZ	211	-11.01 ± 15.01	0.87^*	0.80^*	-1.50 ± 5.43	0.98^*	0.98^*	0.79 ± 8.48	0.95^*	0.95^*

* indicates p -value ≤ 0.05

and the inter-expert variability (Fig. 2.11(c)). Bland-Altman plots of Fig. 2.11(a)–(b) reveals that errors of both automatic and *on-procedure* annotation sets have a slight linear tendency (Pearson's $\rho = 0.36$ and $\rho = 0.10$, respectively; $p < 0.01$ both) towards an under-estimation of LAT precocity compared with the reference. On the other hand, the Bland-Altman plot for the inter-expert variability (bottom panel of Fig. 2.11(c)) reveals no tendency between experts (Pearson's $\rho = -0.03$, $p = 0.215$).

Annotation accuracy classification is shown in Table 2.3. With this classification, 76 % of the mapping point annotations obtained with the automatic algorithm are considered as *accurate* or *highly accurate* compared with the reference. However, the performance of the automatic detection is inferior to the 90 % of mapping points considered as *accurate* or *highly accurate* in the *on-procedure* annotation set.

Table 2.4 illustrates the LAT assessment by b-EGM voltage amplitude. It shows that the automatic algorithm performance decreases with b-EGM voltage amplitude. Automatic LATs have positive error bias (i.e., late LATs than the reference) for normal EGMs and negative error bias (i.e., precocious LATs than the reference) for BZ and CZ EGMs. Moreover, high correlation is found for normal and BZ EGMs with respect to the evaluation reference while in CZ, ρ_s and ρ_c reduce to 0.87 and 0.80, respectively. On the other hand, automatic delineation is outperformed by the *on-procedure* annotation set, which shows lower bias and higher correlation in all b-EGM amplitudes.

Single Expert Assessment

As introduced in section 2.3.1, the *off-procedure* annotation set 1 has annotated all patients and maps of the studied database by the same expert. In order to evaluate

Table 2.5: Single expert assessment of the LAT error (mean \pm SD) of the complete database; and Spearman's rank correlation ρ_s and Lin's concordance correlation factor ρ_c .

Map (#)	Points (#)	Automatic LATs			<i>On-procedure</i> LATs		
		error (ms)	ρ_s	ρ_c	error (ms)	ρ_s	ρ_c
1	128	-1.38 ± 7.60	0.97*	0.97*	-4.51 ± 6.55	0.97*	0.96*
2	110	-1.03 ± 8.55	0.91*	0.91*	-3.85 ± 5.26	0.94*	0.94*
3	155	10.12 ± 11.27	0.91*	0.89*	3.31 ± 5.07	0.98*	0.98*
4	179	-1.06 ± 6.60	0.80*	0.84*	-3.96 ± 5.58	0.86*	0.80*
5	204	-1.53 ± 9.17	0.94*	0.94*	-7.49 ± 7.88	0.96*	0.92*
6	230	0.77 ± 8.44	0.92*	0.93*	-0.04 ± 4.75	0.97*	0.97*
7	49	7.20 ± 14.07	0.65*	0.51*	0.02 ± 5.33	0.96*	0.92*
8	193	3.35 ± 10.87	0.90*	0.89*	-2.95 ± 6.47	0.94*	0.95*
9	156	3.37 ± 12.43	0.84*	0.82*	-3.86 ± 6.89	0.93*	0.91*
10	181	2.77 ± 11.28	0.95*	0.94*	-3.78 ± 5.17	0.98*	0.98*
11	192	2.44 ± 19.32	0.86*	0.86*	1.77 ± 7.98	0.96*	0.97*
12	81	5.30 ± 16.69	0.60*	0.58*	3.06 ± 5.78	0.92*	0.89*
13	87	-2.25 ± 10.55	0.63*	0.73*	2.14 ± 6.29	0.85*	0.87*
14	37	-2.08 ± 24.77	0.50*	0.40*	4.11 ± 5.61	0.93*	0.92*
Total	1982	1.82 ± 12.38	0.92*	0.91*	-1.85 ± 7.07	0.97*	0.97*

* indicates p -value ≤ 0.05

the performance of the automatic method in the complete database, the LAT error was computed using this annotation set as a reference. Table 2.5 shows an increase of the error, especially in the case of the automatic annotations (0.70 ± 12.88 ms), as compared with results shown in Table 2.2.

Execution Time

A low computational time of the algorithm is important for being suitable to be used into an EAM system software and for its application in real time during clinical routine. The complete process of ECG and EGM detection and delineation is done in 791 ± 26 ms/mapping point with a regular computer (Windows 7 based PC, Intel Core i7 3.4GHz, 8Gb RAM with Matlab R2010a). Within this processing time, only the 13.7 % corresponds to the EGM detection and delineation process (109 ± 7 ms/mapping point).

2.4 Mapping Performance

This section assess the performance of the proposed wavelet-envelope detector and delineator in a clinical scenario.

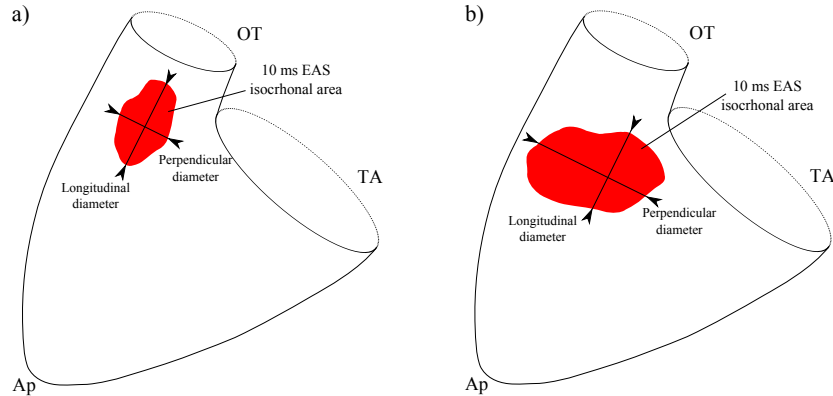


Figure 2.12: Schematic of the RV in posterior-anterior view illustrating the studied map descriptors for different VA origins with septal activation (shown in red): a) expected EAS isochronal area size and shape of an RVOT VA and b) expected EAS isochronal area size and shape of a LVOT VA. Ap: apex, OT: outflow tract, TA: tricuspid annulus.

2.4.1 Idiopathic Outflow Tract Ventricular Arrhythmias

Idiopathic VAs are those occurring in patients without SHD [49]. Among idiopathic VAs, those arising from the outflow tract (OT) regions are the most common [97–100]. In particular, 70-80 % of idiopathic VAs arise from the right ventricle outflow tract (RVOT) and 15 % from the left ventricle outflow tract (LVOT) [49].

Adenosine-induced DADs and triggered activity are the mechanisms responsible of idiopathic outflow tract ventricular arrhythmias (OTVAs) [100]. Therefore, it is a focal arrhythmia where AM can help to identify the EAS for ablation [6]. Ablation treatment of idiopathic OTVAs using EAM systems is very effective once identified the SOO prior to catheter ablation by analysis of the ECG [49]. However, the OTs have complex 3-dimensional anatomical relationships [6, 101, 102], which makes the identification of the SOO especially challenging in those cases showing maximum EGM precocity in septal RVOT, where it is unknown a priori whether the SOO is located in the RVOT or the LVOT.

2.4.2 Map Descriptors

Map descriptors aim to characterize the extent and spreading of the activation pattern during PVCs arising from the septal RVOT. Those were already introduced by *Herczku et al.* [99] and have been shown to predict the SOO of idiopathic OTVAs [99, 103].

Those map descriptors quantify the size and shape of the 10 ms EAS isochronal area in the RV electroanatomical activation map. In particular, the size of the 10 ms EAS isochronal area and its longitudinal and perpendicular diameters relative to the RVOT as it is illustrated in Fig. 2.12. The longitudinal diameter was defined by the

line parallel to the septal projection of the RVOT longitudinal axis (perpendicular to the plane of the pulmonary valve), then defining its perpendicular diameter. Hence, the spreading of the activation pattern was characterized by defining the ratio between those two axes [99].

As it is illustrated in Fig. 2.12, these map descriptors were proposed under the hypothesis that VAs arising from the septal RVOT will show an activation pattern whose main direction extends along the fibre orientation (i.e., elliptical shape of the EAS isochronal area oriented along the longitudinal direction, see Fig. 2.12(a)) whereas those arising from the LVOT would show slower and less preferential conduction path in the longitudinal direction (i.e., circular/elliptical shape of the EAS isochronal area along the perpendicular direction, see Fig. 2.12(b)) [99, 103].

2.4.3 Patient Sample

The patient sample is composed of 18 patients with symptomatic, drug-refractory OT PVC beats, whose were admitted for ablation procedure at Hospital Clinic (Barcelona, Spain). Inclusion criteria were as follow: 1) patients with idiopathic OTVAs submitted for ablation; 2) EAS located at the septal part of the RVOT electroanatomical map and 3) successful ablation at the EAS identified by manual AM during the intervention. All patients signed their written informed consent form and the study was approved by the Local Ethics Committee.

Patient electroanatomical maps were acquired with the CARTO 3 system (*Biosense Webster, Inc., Diamond Bar, CA, USA*) using a 3.5 mm irrigated tip *NaviStar Thermocool* catheter (*Biosense Webster, Inc., Diamond Bar, CA, USA*) for mapping and ablation. The 12-lead surface ECG and EGM signals were displayed during each intervention and stored for offline prospective analysis. EGM signals were acquired point-by-point during stable contact with the myocardium; pulmonary and aortic root wall and assuring the presence of PVCs matching the clinical VA during mapping time.

The EAM system operator manually annotated the onset of the distal b-EGM signal from the mapping catheter during the intervention. Detailed AM of the RVOT was performed during PVCs. If according to RVOT isochronal activation map, a LVOT origin was suspected, the distal CS, great cardiac vein, left anterior descendent vein, supra- and subvalvular LVOT were mapped as part of the electrophysiological study protocol. A LVOT origin was suspected when EAS was located ≥ 1 cm below pulmonary valve or the 10 ms isochronal area longitudinal/perpendicular diameter ratio was ≤ 0.8 [103].

After the acquisition of a sufficient number of mapping points to reconstruct anatomy and activation pattern by using a filling threshold of 6 mm, RF was delivered at the EAS. A power limit of 40 W was used in the RVOT, subvalvular LVOT and aortic root whereas a limit of 20 W was used in the CS.

2.4.4 Evaluation Protocol

Offline automatic LAT detection was performed using the presented wavelet-envelope detector and delineator. Those annotations were manually introduced in the CARTO 3 system for analysis.

Manual and automatic isochronal activation maps were reconstructed using an interpolation filling threshold of 6 mm. Those maps were generated by discretising the colour scale into 10 ms isochronal areas, defined as those areas whose mapping point LATs lie within a temporal interval of 10 ms starting from the earliest activated EGM mapping point in 10 ms steps.

The CARTO 3 integrated measurement tools were used for offline measurement of the map descriptors introduced in section 2.4.2. Additionally, in those maps where a RVOT origin was identified, the accuracy of the proposed algorithm in locating the EAS for ablation purposes was assessed. In that regard, two distances were measured: 1) the distance from the centre of mass of the 10 ms EAS isochronal area to the effective RF ablation site and 2) the distances between EAS isochronal area centre of masses from manual and automatic maps. The effective RF ablation site was defined as that location where ablation terminates the clinical arrhythmia. LVOT activation maps were not considered for this specific measurement because they did not fulfil the 6 mm filling threshold criteria as they had lower density of mapping points, compared with the RVOT maps.

Comparison between different populations is given by the Wilcoxon-Mann-Whitney test for continuous variables and by the Fisher's exact test for categorical variables. A p -value ≤ 0.05 was required for considering results of statistical significance. Sensitivity Se , specificity Sp and the accuracy Acc of the SOO identification have been computed as:

$$Se = \frac{TP}{TP + FN}, \quad (2.24)$$

$$Sp = \frac{TN}{TN + FP}, \quad (2.25)$$

$$Acc = \frac{TP + TN}{TP + FP + TN + FN}, \quad (2.26)$$

where TP stands for the number of *true positives* meaning the number of LVOT SOO patients correctly identified, TN stands for the number of *true negatives* meaning the number of RVOT SOO patients correctly identified, and FP and FN stand for the number of *false positives* and *false negatives*, meaning the number of miss identifications of RVOT and LVOT SOO patients, respectively.

2.4.5 Results

Characteristics of the Patient Sample

Eighteen patients were included in the study (50 % males, mean age 56.3 ± 16.6 years, 33.3 % hypertensive). Table 2.6 summarizes the baseline clinical characteristics of the

Table 2.6: Baseline clinical characteristics of the studied patient sample. Values are given in mean \pm SD and median [1st quartile,3rd quartile] or number and (%), when appropriate.

	Entire population (n = 18)	RVOT SOO (n = 6)	LVOT SOO (n = 12)	<i>p</i> -value ¹
Age (years)	56.3 \pm 16.6 58 [45,72]	51.5 \pm 15.8 45 [39,69]	58.8 \pm 17.1 60 [53,72]	0.372
Male sex, (n)	9 (50)	2 (33.3)	7 (58.3)	0.244
Hypertension, (n)	6 (33.3)	1 (16.7)	5 (41.6)	0.256
Mapping points (n)	175 \pm 61 169 [120,240]	172 \pm 47 155 [148,181]	177 \pm 69 183 [112,247]	1.000
Total RF applications (n)	6 \pm 6 3 [1,8]	2 \pm 2 2 [1,3]	7 \pm 7 4 [1,12]	0.259
RF application on RVOT (n)	3 \pm 4 2 [0,4]	2 \pm 2 2 [1,3]	3 \pm 4 1 [0,5]	0.556

¹ refers to the comparison between RVOT and LVOT SOO.

Table 2.7: Distance from the 10 ms EAS isochronal area to the effective RF ablation site and inter-EAS area distance measured from the RVOT origin population.

Patient	Distance to the effective RF site (mm)		Inter-EAS isochronal area distance (mm)
	Manual	Automatic	
1	4.3	3.1	2.8
2	9.1	12.4	7.2
3	11.5	8.8	6.8
4	7.2	8.1	10
5	2.7	2.7	0
6	5.3	4.1	6.6

patient sample. Ablation was successful in all these eighteen patients, twelve of them in the LVOT (9 in left/right coronary cusp and 3 in subvalvular LVOT) and six in the septal RVOT. The median [interquartile range] number of RF applications was 3 [1,8] and mean RF time was 6 \pm 6.7 minutes. No complications were observed.

Identification of the Earliest Activation Site

Table 2.7 shows the distance of the identified 10 ms EAS isochronal area centroid from manual and automatic activation maps to the effective RF application point as well as the distance between automatic and manual EAS area centroids. Automatic and manual activation maps have similar distance with respect to the effective RF application point (difference of distances: 0.15 \pm 2.08 mm, $p = 0.859$) and short distance between them (5.55 \pm 3.56 mm).

Table 2.8: Map descriptors measurement from manual and automatic activation maps. Data are shown as mean \pm SD and median [1st quartile,3rd quartile].

Map descriptor	Measurement	Entire population (n = 18)	RVOT SOO (n = 6)	LVOT SOO (n = 12)	<i>p</i> -value ¹
10 ms isochronal area (cm ²)	Manual map	3.83 \pm 3.03 2.30 [2.00,5.20]	2.77 \pm 2.52 2.05 [1.50, 2.30]	4.37 \pm 3.22 3.85 [2.30, 5.80]	0.157
	Automatic map	2.44 \pm 1.99 1.95 [0.80,2.70]	3.10 \pm 2.67 2.25 [0.70,5.50]	2.11 \pm 1.59 1.65 [0.90,2.65]	0.767
	<i>p</i> -value ²	0.117	0.971	0.040	
10 ms isochronal area longitudinal/perpendicular ratio	Manual map	1.38 \pm 0.85 1.06 [0.73,1.63]	1.97 \pm 0.88 1.90 [1.12,2.63]	1.08 \pm 0.67 0.82 [0.72,1.31]	0.019
	Automatic map	1.27 \pm 0.71 1.00 [0.74,1.83]	2.01 \pm 0.44 1.99 [1.72,2.38]	0.90 \pm 0.48 0.80 [0.58,1.00]	0.001
	<i>p</i> -value ²	0.740	0.937	0.544	

¹ refers to the comparison between RVOT and LVOT SOO.

² refers to the comparison between manual and automatic map measurements.

Assessment of Map Descriptors Measurement and Origin Identification

Table 2.8 shows the measurements of the map descriptors obtained from manual and automatic activation maps. In the LVOT population, statistically significant differences were observed in the size of the 10 ms EAS isochronal area determined from automatic vs. manual activation maps. Automatic maps provide smaller 10 ms EAS isochronal areas compared with the manual maps (2.11 ± 1.59 cm² vs. 4.37 ± 3.22 cm², respectively, $p = 0.040$). The rest of map descriptor measurements showed no statistically significant differences between automatic and manual activation maps.

Map descriptors were compared in their ability of distinguish between RVOT and LVOT origin (see Table 2.8). The 10 ms isochronal area longitudinal/perpendicular diameter ratio differs significantly between RVOT and LVOT populations, whether measured from the manual activation maps (1.97 ± 0.88 vs. 1.08 ± 0.67 , $p = 0.019$) or from the automatic activation maps (2.01 ± 0.44 vs. 0.90 ± 0.48 , $p = 0.001$).

Figure 2.13 and Table 2.9 illustrate the SOO identification. The size of the 10 ms EAS isochronal area distinguishes better between RVOT and LVOT populations if measured from manual activation maps with 83 % sensitivity and 67 % specificity using an optimal threshold for area ≥ 2.2 cm². However, superior SOO identification performance has been achieved by the 10 ms isochronal area longitudinal/perpendicular diameter ratio measured either from manual or automatic activation maps. More specifically, the best SOO identification performance is obtained from the automatic activation map, with 92 % sensitivity and 100 % specificity using an optimal threshold for the longitudinal/perpendicular diameter ratio ≤ 1.27 , which yields in a SOO identification accuracy of 94 % in the studied patient sample.

Table 2.9: LVOT SOO identification performance of the map descriptors measured from manual and automatic activation maps.

Map descriptor	Classification characteristics	Manual map	Automatic map
10 ms isochronal area	Optimal threshold (cm ²)	2.2	2.5
	Sensitivity (%)	83	33
	Specificity (%)	67	67
	Accuracy (%)	77	44
	AUC	0.72	0.48
10 ms isochronal area longitudinal/perpendicular ratio	Optimal threshold	0.91	1.27
	Sensitivity (%)	58	92
	Specificity (%)	100	100
	Accuracy (%)	72	94
	Hypothesis-based threshold	1	1
	Sensitivity (%)	67	67
	Specificity (%)	83	100
	Accuracy (%)	72	78
AUC	0.84	0.94	

As explained in section 2.4.2, VAs arising from the RVOT are expected to show a preferential activation in the longitudinal direction whereas those arising from the LVOT should show slower and less preferential longitudinal activation. This hypothesis allows establishing a comparison between both AM modalities (i.e. manual and automatic) using a hypothetical threshold for LVOT SOO identification ≤ 1 for the 10 ms isochronal area longitudinal/perpendicular diameter ratio. This decreases automatic maps' performance on SOO identification to 67 % sensitivity, 100 % specificity and 78 % accuracy, which remains slightly superior to the performance obtained from manual activation maps (67 % sensitivity, 83 % specificity and 72 % accuracy). This superiority is consistent with the higher area under the curve (AUC) observed for automatic activation maps (0.94) compared with the manual activation maps (0.84).

2.5 Discussion

There is no clear consensus regarding the measurement of LATs in b-EGMs [55, 80], especially when fractionated or split potentials are present [49]. However, detection of the EAS by locating the onset of the b-EGM has been shown to be useful for the treatment of focal arrhythmias [80, 99]. Some definitions of the activation onset [55] seem to be arbitrary as they depend on the amplitude scale of the activation. Hence, the identification of the activation onset for LAT computation in AM is a strongly observer-dependent task that complicates the selection of a reliable reference annotations for evaluation.

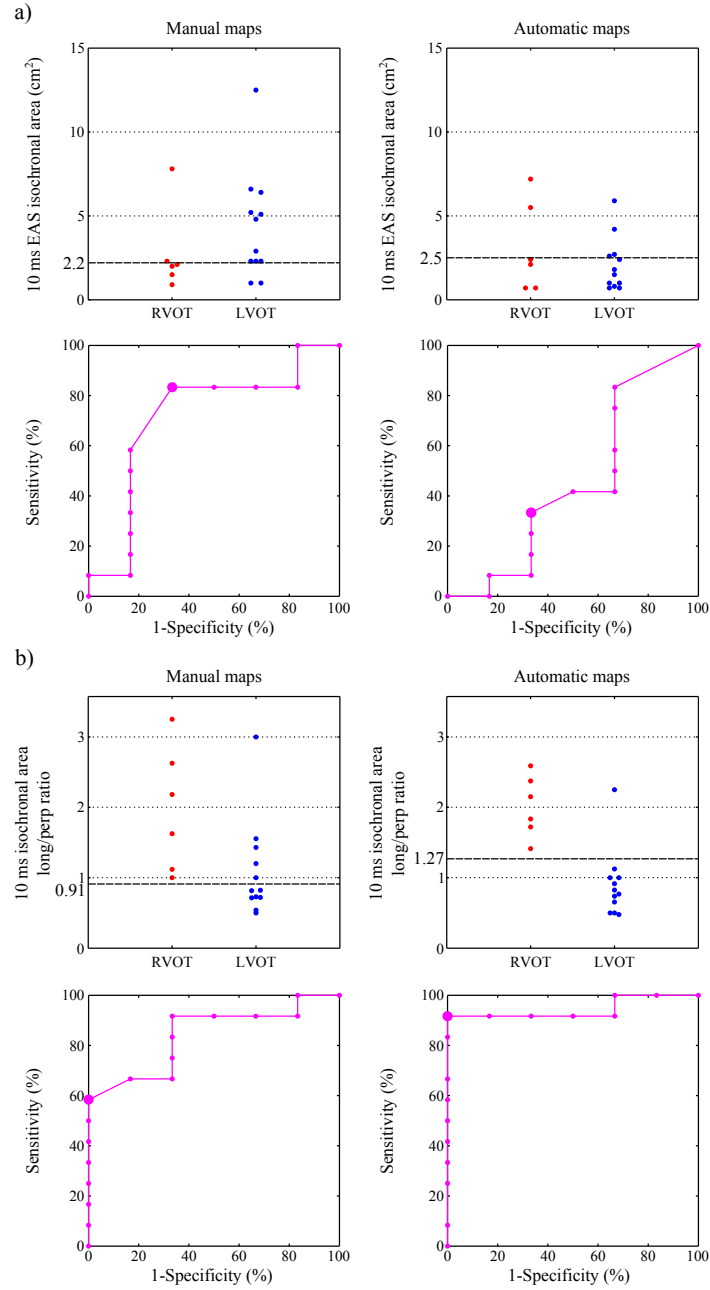


Figure 2.13: SOO identification by map descriptors, measured from manual and automatic activation maps (left and right column of panels, respectively): a) 10 ms EAS isochronal area and b) 10 ms EAS isochronal area longitudinal/perpendicular diameter ratio. Top panels show scatter plots by SOO (red dots: LVOT SOO, blue dots: RVOT SOO). Black dashed line indicates the optimal threshold for SOO identification. Bottom panels show the corresponding receiver operation curve where big dots indicate the optimal point for SOO identification.

EAM systems are useful tools for cardiac mapping as they allow to have a 3D location of the mapping catheter within the patient’s heart combined with the electrical properties of the cardiac substrate [49]. However, they do not provide automatic measurement of LATs using the b-EGM activation onset. Therefore, this must be made manually by the operator, turning it into a highly time-consuming task.

In this chapter, an automatic envelope-wavelet EGM detector and delineator for AM of focal VTs is introduced. The complete process is the combination of a two-step signal analysis. First, detection and delineation of the beat of interest in the surface ECG is performed. The second step uses this delineation as a basic window for the EGM delineation algorithm. The presented algorithm exploits the DWT time-scale characteristics of the EGM activation envelope signal in order to identify the b-EGM activation onset for automatic AM. As a secondary result, the end of the activation is delineated using a systematic approach. Moreover, spatiotemporal information of close mapping points with morphologically similar signals is combined in order to obtain more reliable activation maps.

Evaluation was conducted by means of two different studies. First, a detection performance study where a controlled database with annotations from different experts was used in order to evaluate the accuracy of the algorithm in identifying the onset of b-EGMs for AM. Second, the presented algorithm was evaluated in a clinical study where its ability to generate activation maps helping in the decision process for ablation interventions was assessed. In both cases, the performance of manual annotations performed during the ablation procedure were taken as a reference for the current achieved performance.

2.5.1 Algorithm Performance

In this part of the study, a good agreement between the proposed method and a gold standard built from expert annotations was obtained. The error compared with the combination of annotations from two experts is 1.20 ± 10.72 ms and correlation with the evaluation reference is high ($\rho_s = 0.94$ and $\rho_c = 0.93$). The error bias is low and positive, meaning that the automatic method provides slightly later LATs than the reference. In terms of the accuracy of the annotations, 76 % of the evaluated mapping points are considered as *accurate* or *highly accurate*.

Annotation errors show to be higher in the subset of mapping points with bipolar voltage < 0.5 mV (-11.01 ± 15.01 ms). This points out the fact that identifying the b-EGM onset in low-voltage signals is a difficult task. Higher differences between experts have also been found for this sub-set of mapping points (0.79 ± 8.48 ms).

Additionally, the error increases up to 1.82 ± 12.38 ms and the correlation decreases to $\rho_s = 0.92$ and $\rho_c = 0.91$ when only the annotation set from a single expert is considered as reference.

The automatic method does not perform better than the *on-procedure* annotations when compared with the evaluation reference (error of -2.80 ± 6.01 ms and $\rho_s = 0.97$). The negative error bias indicates that the *on-procedure* annotations provide

slightly earlier LATs than the reference. Moreover, 90 % of the evaluated mapping points are considered as *accurate* or *highly accurate* annotated. On the other hand, the difference annotation for low-voltage EGMs compared to the inter-expert variability suggests high similarity to one of the reference experts in those low-voltage EGMs.

Figure 2.14 illustrates four representative examples of activation maps obtained with all the LAT annotation sets of the studied database for detection performance evaluation. In those examples, a concentric spreading of the activation is more clear and uniform at the automatic reconstructed map, as it would be expected in case of focal activity [6]. The EAS is identified from all maps (automatic and manual maps) in the same location: septal part of the tricuspid annulus for map #1; lateral (anterior) part of the RVOT for maps #8, #9 and septal part of the RVOT for map #10 (see Fig. 2.14). The effective RF ablation point (red spheres pointed by white arrows) lies within the two first isochronal areas in all cases. Nevertheless, it must be noted that having an annotation error of -0.09 ± 6.85 ms, 4.04 ± 10.62 ms, 4.12 ± 12.07 ms and 3.29 ± 11.17 ms for maps #1, #8, #9 and #10 respectively, does not result in a lack of precision in determining the EAS for ablation of focal VAs.

In terms of computational cost, the proposed algorithm detects the b-EGM activation onset in 109 ± 7 ms, a small percentage of the total processing time per mapping point (791 ± 26 ms). It also should be noted that the computation time associated to the surface ECG delineation can be neglected in real applications since it can be performed online by current EAM systems. Manual annotation of each b-EGM was reported to be performed within 3 to 4 seconds per point. Moreover, the larger part of the acquisition time is due to the necessary operations of the physician for positioning and stabilizing the catheter and the occurrence of a PVC beat matching the clinical VA during the intervention. Therefore, the computational time of the proposed signal processing method can be considered appropriate for its use in EAM systems.

2.5.2 Clinical Application

In RVOT SOO patient maps, the location of the 10 ms EAS isochronal area centroids in manual and automatic activation maps are 5.55 ± 3.56 mm apart, illustrating the accuracy of the automatic algorithm for providing precise localization of the EAS isochronal area. Additionally, the distance from the 10 ms EAS isochronal area to the effective RF application site of manual and automatic activation maps showed to be similar (difference: 0.15 ± 2.08 mm, $p = 0.859$). Therefore, these results illustrate that the automatic detector is as accurate as manual LAT identification for the purpose of ablation of focal VAs.

The measurement of the activation pattern descriptors show statistically significant differences for the size of the 10 ms EAS isochronal areas in LVOT population obtained from the automatic maps, which shows to be smaller than those measured from the manual maps. This may come from: 1) the complex anatomical relationship between LVOT and RVOT structures [6,101,102] and/or 2) far-field signals measured from the LVOT at RVOT level, which are usually shown as low amplitude baseline drifts in the bipolar EGM signal that are difficult to distinguish by the automatic algorithm from

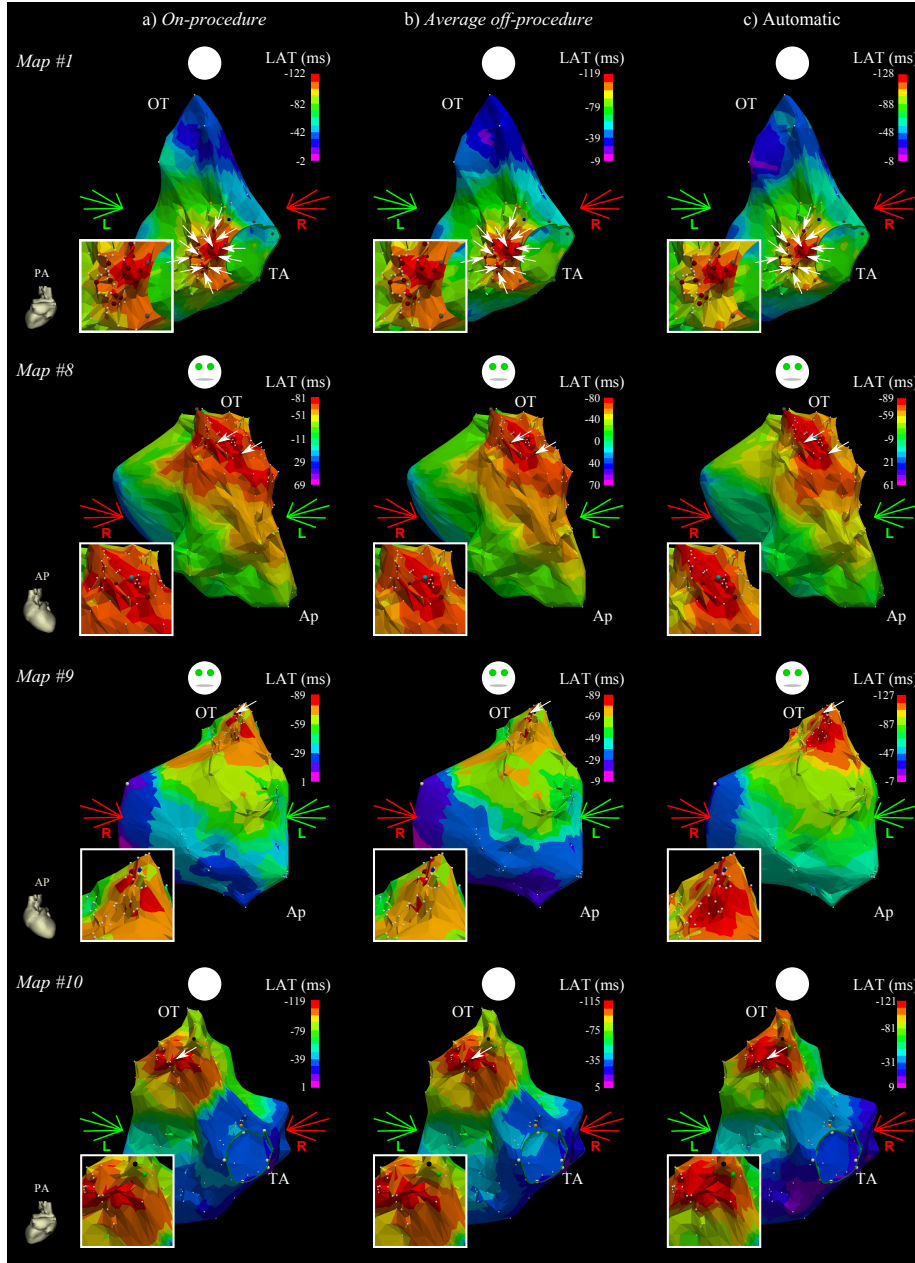


Figure 2.14: Representative examples of activation maps with zoom view of the EAS (white square): a) using the *on-procedure* annotation set, b) using the *averaged off-procedure* annotation set and c) using the automatically detected LATs. LATs are shown in 10 ms isochronal areas colour-coded from red (earlier) to pink (later). White small spheres indicate location of mapping points whereas white big spheres indicate anatomical reference points. Pointed red spheres indicate location of RF delivery. Orange spheres indicate HPS, cyan spheres indicate double EGMs, blue spheres indicate end of sheath, black spheres indicate a point of interest, green spheres indicate manually introduced annotations and grey spheres indicate discarded points. Ap: apex, AP: anterior-posterior OT: outflow tract, PA: posterior-anterior, TA: tricuspid annulus.

baseline noise level. Therefore, the LAT detection in LVOT SOO with septal activation at RVOT level supposes a challenge for automatic AM. The rest of evaluated map descriptors show no statistically significant differences measured from automatic or manual activation maps.

Regarding the SOO identification, the 10 ms isochronal area longitudinal/perpendicular diameter ratio, measured either from manual or automatic activation maps, shows the higher LVOT SOO identification performance in the current patient sample. The best performance was obtained from the automatic activation map by using a longitudinal/perpendicular diameter ratio threshold ≤ 1.27 , yielding 92 % sensitivity and 100 % specificity compared with 58 % sensitivity and 100 % specificity using a smaller longitudinal/perpendicular diameter ratio threshold (≤ 0.91). For SOO identification, it is desirable to have very high specificity while preserving sensitivity as high as possible, avoiding an unnecessary retrograde aortic approach for LVOT and aortic root mapping, which can increase the complication rate of OT ablation procedures.

These optimal thresholds for SOO identification using the 10 ms isochronal area longitudinal/perpendicular diameter ratio represent slightly different activation patterns at automatic and manual activation maps. On the one hand, the optimal ratio threshold found for automatic maps (≤ 1.27) shows a slightly longitudinal dispersion of the activation of the 10 ms isochronal area at the septal RVOT from some LVOT cases of the studied patient sample with automatic LAT detection. On the other hand, the optimal ratio threshold for manual maps (≤ 0.91) shows an opposite behaviour indicating that some RVOT cases with septal activation of the studied patient sample show a slightly perpendicular dispersion of the activation of the 10 ms isochronal area with manual LAT identification.

Nevertheless, this dispersion is not critical because both optimal thresholds are concordant with the obtained in previous studies [99, 103]. In that regard, an evaluation of the SOO identification performance was conducted based on the rationale of the 10 ms isochronal area longitudinal/perpendicular diameter ratio measurement. Therefore, a hypothesis-based threshold allows comparing the performance of both mapping modalities with slightly superiority of the activation maps created with the introduced automatic LAT detector in the studied patient sample. Representative examples of the resulting automatic activation maps and the differences in EAS shapes between RVOT and LVOT populations are illustrated in Fig. 2.15.

Moreover, the obtained performance on SOO identification is inferior to the perfect identification reported by *Herczku et al.* [99], which was achieved using only the 10 ms isochronal area longitudinal/perpendicular diameter ratio. On the other hand, using the diameter ratio in a study with larger patient sample, *Acosta et al.* [103] reported similar results to that obtained by using the hypothesis-based threshold (77 % sensitivity and 100 % specificity). In their work, SOO identification achieved 91 % sensitivity and 100 % specificity with the inclusion of a decision tree which incorporates the distance from the 10 ms EAS isochronal area to the pulmonary valve plane [103]. Additionally, automatic AM allows faster and observer-independent measurements, and has been shown to be superior to manual mapping for idiopathic VA SOO identification in the studied patient sample.

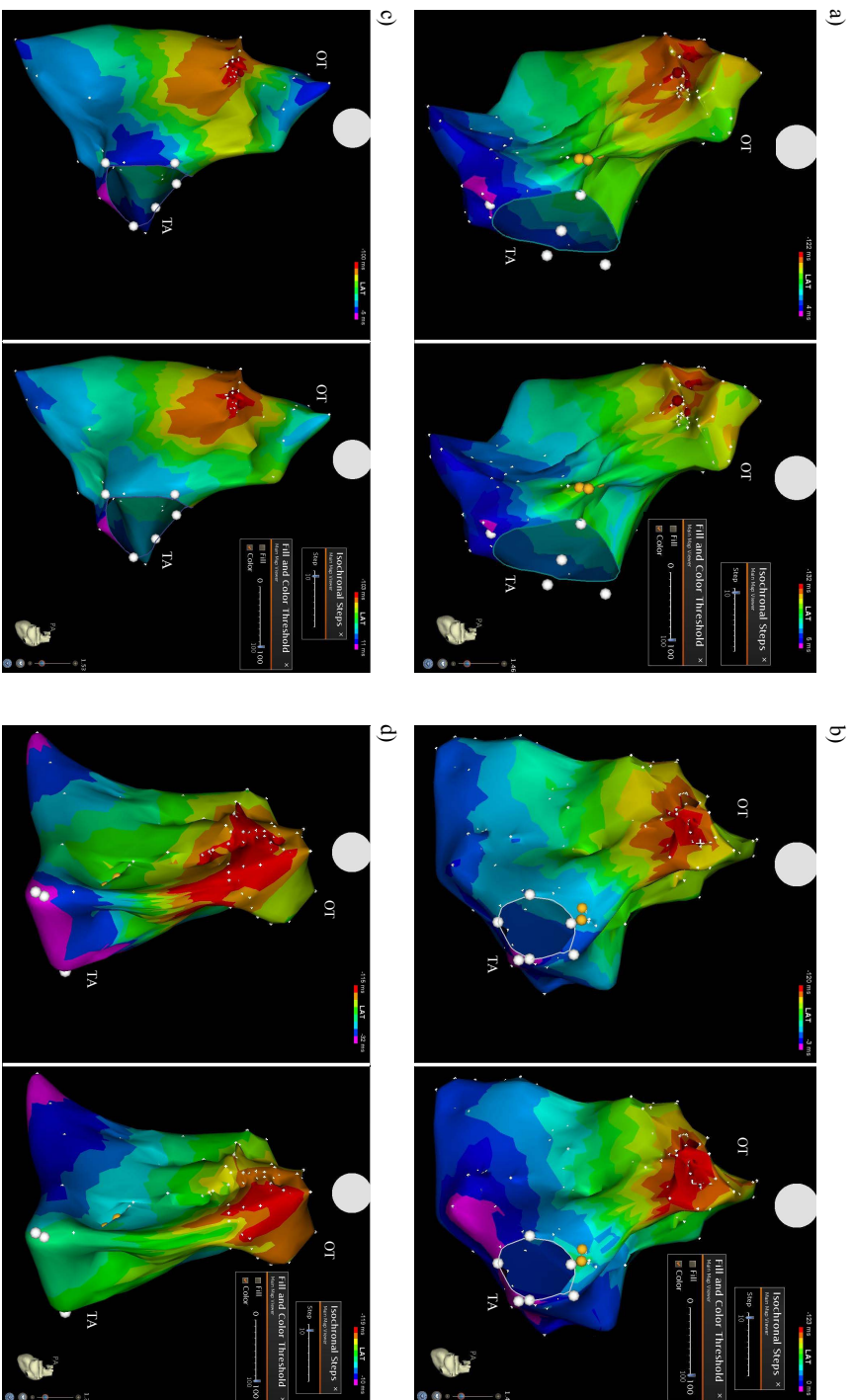


Figure 2.15: Examples of RV 10 ms isochronal activation maps shown in posterior-anterior view from RV/OT SOO VA patients (panels (a) and (c)) and for LVOT SOO VA patients (panels (b) and (d)). Each panel shows the manual and automatic activation maps at the left and right, respectively. White dots indicate the location of mapping points, white spheres indicate anatomical location, yellow spheres indicate HPS potentials and red spheres indicate RF applications. AP: anterior-posterior, OT: outflow tract, TA: tricuspid annulus.

2.5.3 Comparison with Other Methods

El Haddad et al. proposed an algorithmic detection of the onset and end of b-EGM signals based in a 4-state algorithm [81, 82]. This approach identifies the activation onset and end by counting the samples where a rectified band-pass filtered b-EGM signal is above or below a set of thresholds adapted to the studied database by trial-error process and was evaluated by visual inspection in a small set of EAM points from randomized patients.

Due to the lack of standard databases with reference annotations by expert physicians, the comparison of both methodologies is rather difficult. Moreover, the introduced envelope-wavelet detector and delineator shows a simplest and direct relation between threshold factor γ_o and annotation outcomes, making it more simple to be adjusted to the desire point of operation, whereas for the same process in [81, 82] it may imply tuning up to 4 different parameters which close interplay between them and detection outcomes become less predictable.

Additionally, in the present state of the art, there are not yet public reports about LAT identification performance from the newly released CONFIDENSE module (*Biosense Webster, Inc., Diamond Bar, CA, USA*) for CARTO system. Therefore, can neither be included in order to evaluate the LAT detection performance of the introduced wavelet-envelope detector and delineator.

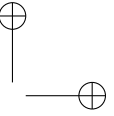
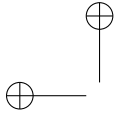
2.5.4 Limitations

In the introduced wavelet-envelope detector and delineator algorithm, threshold factors and searching intervals were selected based on empiric electrophysiological background and technical experience with surface ECG detection and delineation. Therefore, this entails a limitation since no sensitivity analysis has been performed in order to assess the effects of variation of these threshold factors.

Regarding the clinical application of the introduced wavelet-envelope detector and delineator algorithm, the evaluation database represents a very limited amount of patients with unbalanced classes (6 RVOT vs. 12 LVOT). This yields in stair-shaped receiver operation curves, as illustrated in Fig. 2.13, which may explain the slight differences of optimal threshold values obtained in the studied patient sample when compared with the bibliography [99, 103]. Moreover, half of LVOT SOO cases had ablation performed in both RVOT and LVOT, which may also contribute to the differences in optimal threshold values. This fact illustrates the difficulties of the SOO identification because of the complex anatomical relationships between OTs that yields in RF applications at the same level in both structures for termination of the clinical VA. Another possible source of error may come from the size of the mapping catheter tip used for mapping and ablation in this patient sample (3.5 mm), which may sense far-field from the other side of the septal separation between OTs. The usage of catheters with smaller electrodes may also improve both signal quality and local electrical activity measurements.

2.6 Conclusion

This chapter presents an envelope-wavelet detector and delineator to identify the b-EGM activation onset for automatic AM during focal VTs. It has been tested in two different databases assessing its precision and usefulness in clinical conditions. If integrated with EAM systems, could help physicians and companion technicians to reduce signal acquisition time and intervention since it is able to automatically identify the b-EGM activation onset in less than one second. Moreover, it could eventually be more beneficial when applied on EAM data acquired with multi-electrode catheters. These catheters acquire multiple EGM signals at one single beat, thus allow to generate high-density activation maps in a short amount of time. Therefore, the benefits of those multi-electrode catheters cause that the creation of accurate activation maps based on LAT onsets becomes unaffordable without automatic or semi-automatic signal processing techniques.



“Books must be treated with respect, we feel that in our bones, because words have power. Bring enough words together they can bend space and time.”

Terry Pratchett

Chapter 3

Spatiotemporal High-Density Atrial Activation Mapping

3.1 Introduction	
3.1.1 Atrial Fibrillation	
3.1.2 Activation Mapping of Atrial Fibrillation	
3.1.3 Motivation	
3.2 Spatiotemporal Activation Mapping Algorithm	
3.2.1 Algorithm Overview	
3.2.2 Activation Propagation Pattern and Tissue Model	
3.2.3 Modelling Unipolar Electrogram Signals	
3.2.4 Estimation of Tissue Conduction Velocity	
3.2.5 Focus Initialisation	
3.2.6 Iterative Model Optimization Algorithm	
3.2.7 Reconstruction of Activation Maps	
3.3 Estimation of High-Density Activation Maps	
3.3.1 Testing Database	
3.3.2 Evaluation Protocol	
3.3.3 Results	
3.4 Discussion	
3.4.1 Detection Performance	
3.4.2 Spatiotemporal Mapping Approach	
3.4.3 Limitations	
3.5 Conclusion	

3.1 Introduction

3.1.1 Atrial Fibrillation

The first mention to AF was done by *Thomas Lewis* in the beginning of the 20th century [104]. AF is a supraventricular arrhythmia which is characterized by an irregular activation of the atrium (400-700 beats/minute) and irregular ventricular response.

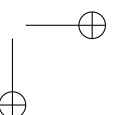
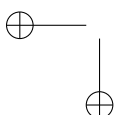




Figure 3.1: Example of ECG recording during AF (from top to bottom, leads: V1, II and V5) showing f waves (especially noticeable in lead II) and irregular ventricular response. Reproduced and modified from [106].

Electrocardiographically, AF shows absence of distinct repeating P waves substituted by continuous electrical activity called “f waves” and irregular occurrence of QRS complexes [4, 38, 105, 106], as illustrated in Fig. 3.1.

AF is the most common form of sustained arrhythmia in clinical practice [2, 38, 59, 106], affecting between 1 to 2 % of general population, with an increasing incidence due to population ageing [2, 59]. It is responsible of one third of the hospitalizations in cardiac arrhythmias units [106] and therefore, AF is becoming an epidemiological threat affecting patient’s quality of life [107–109].

The mechanism underlying the initiation and perpetuation of AF are still under investigation. *Moe et al.* [39] first proposed the wavelet hypothesis underlying the initiation and perpetuation of AF, describing the presence of multiple propagating wavelets sustaining the fibrillation process, which was experimentally proved later by *Allessie et al.* [40, 41]. Other proposed mechanisms include driving foci, mainly located at the pulmonary veins [42], reentries [43, 44], longitudinal conduction dissociation [46] and transmural conduction of fibrillation waves between epi- and endocardial atrial layers [45]. However, the complete phenomena are not yet fully understood [43], limiting the optimal treatment of patients.

3.1.2 Activation Mapping of Atrial Fibrillation

AM is the most commonly used method for visualization and study of cardiac arrhythmias [110]. During haemodynamically stable and regular tachycardia, activation maps can be created after sequential recording of EGMs and detected LATs can be referred against a fiducial point in a simultaneously recorded surface or intracardiac signal, as introduced in section 2.1.1 [6, 49, 79, 80]. However, during irregular tachycardia like AF, simultaneous mapping is needed due to the non-repetitive nature and complexity of the arrhythmia [43].

Multi-electrode mapping catheters lack spatial resolution during more complex atrial activity due to electrode sparsity and bad wall contact [111]. For high-density mapping of more complex AF, a high-density MEA mapping sensor is needed [43].

Detection of LATs from u-EGMs is related to the steepest negative slope (dV/dt) as a result of an activation wave under-passing the recording electrode [6, 53–56] (see Fig. 2.2(a)). The recorded signals using MEA sensors can be displayed into a matrix whose elements are related to the electrode locations on the mapping array, thus, displaying the LATs detected from each of the electrodes allow to create activation maps which show the propagation of cardiac activation [41, 43].

3.1.3 Motivation

The construction of high-density activation maps based on individual u-EGM signal LATs ignores the information embedded in the morphology of the u-EGM signal, thus reducing this information to a time-event signal. This chapter introduces a spatiotemporal approach which uses the information retained in the u-EGM signal shape in order to estimate and construct robust and spatially consistent high-density activation maps. The proposed approach iteratively fits an activation pattern model to the acquired cardiac activity and reconstructs the activation map as the combination of contributions from different isotropic focal activation sources.

3.2 Spatiotemporal Activation Mapping Algorithm

3.2.1 Algorithm Overview

Before algorithm starts, a 100 ms signal excerpt that includes a complete activation across the MEA sensor is selected and the mapping array is segmented into overlapped groups of 5×5 electrodes (area 64 mm^2), being this the size of the analysing mask. For notation, $s_i[n]$ stands for the recorded u-EGM signal corresponding to the i th electrode from the 5×5 group under analysis, $i = 1 \dots 25$, and $\hat{s}_i[n]$ denotes the modelled u-EGM signal corresponding to the same i th electrode located in the cardiac tissue model. The flow of the processing steps is described below:

- L1: For each 5×5 group of electrodes:
1. Estimate conduction velocity and initial focus location.
 2. Generate activation pattern and $\hat{s}_i[n]$.
 3. Compare each $s_i[n]$ against each $\hat{s}_i[n]$.
- L2: While the similarity is below a given threshold or the maximum number of iterations is not reached
- a) Compute new focus location for next iteration.
 - b) Generate new activation pattern and $\hat{s}_i[n]$.
 - c) Compare each $s_i[n]$ against each $\hat{s}_i[n]$.
- End of loop L2.
- End of loop L1. Go to step 1 unless all 5×5 groups have been already analysed.
4. Activation map reconstruction.

3.2.2 Activation Propagation Pattern and Tissue Model

Without loss of generality, the simplest activation pattern can be considered as a single focal point generating an activation wavefront concentrically spreading with uniform conduction velocity. In a 2-dimensional plane, the wavefront coordinates $\mathbf{w}_{\mathbf{f},v}[n, \theta] = [w_x[n, \theta], w_y[n, \theta]]^\top$ created by a circular activation pattern with center at the focus location $\mathbf{f} = [f_x, f_y]^\top$ at a time instant n can be described by the parametric form:

$$\mathbf{w}_{\mathbf{f},v}[n, \theta] = \begin{bmatrix} w_x[n, \theta] \\ w_y[n, \theta] \end{bmatrix} = \begin{bmatrix} f_x \\ f_y \end{bmatrix} + v \cdot n \cdot \begin{bmatrix} \cos(\theta) \\ \sin(\theta) \end{bmatrix}, \quad (3.1)$$

where $\theta \in [0, 2\pi)$ and v stand for the conduction velocity of the medium. Note that $\mathbf{w}_{\mathbf{f},v}[n, \theta]$ is the expression of a circumference of radius $v \cdot n$ centred at \mathbf{f} . Hence, (3.1) defines a circular activation pattern from a single focus, becoming approximately a planar wave when the focus is located far away from the observer scope.

The activation pattern was introduced into a uniform double layer (UDL) model using the boundary element method [112]. The UDL models a square planar slice of atrial tissue of 12×12 mm and 2 mm thick, in agreement to the average thickness of the human atria [113]. For simplicity, epicardial and endocardial conduction velocities were assumed to be equal [114]. Consequently, the modelled activation propagates in parallel and at the same velocity in both epicardial and endocardial sides of the UDL model.

3.2.3 Modelling Unipolar Electrogram Signals

A virtual multi-electrode array (v-MEA) sensor with 5×5 , 2 mm spaced, circular electrodes, mimicking the real MEA, was placed on the epicardial side of the UDL enabling calculation of electrical activity during activation. Each i th virtual electrode of the v-MEA has a spatial location $\mathbf{e}_i = [x_i, y_i]^\top$. The infinite medium potential generated by a UDL at a time instant n and position \mathbf{e}_i is given by [112]:

$$\hat{s}_i[n] = -\frac{V_d}{4\pi} \Omega_{\mathbf{e}_i}[n], \quad (3.2)$$

where V_d stands for a constant value called *double layer strength* of the UDL [112] and $\Omega_{\mathbf{e}_i}[n]$ stands for the solid angle of the surface created by the activation wavefront $\mathbf{w}_{\mathbf{f},v}[n, \theta]$ and subtended within the UDL at \mathbf{e}_i , as illustrated in Fig. 3.2. This solid angle $\Omega_{\mathbf{e}_i}[n]$ can be computed numerically by dividing the wavefront surface into triangular elements and summing the solid angles subtended by each surface element using the plane triangle formula [115].

Equation (3.2) describes the electrophysiological behaviour of local u-EGMs recorded from the myocardium. The potential $\hat{s}_i[n]$ increases when the activation wavefront approaches the recording electrode, shows a fast downward slope when the wave underpasses the electrode and goes back to baseline when the wave continues propagation [6, 53, 54, 56, 112]. The amplitude of this fast downwards slope is proportional to the *double layer strength* V_d [112]. Hence it can be estimated from the measured

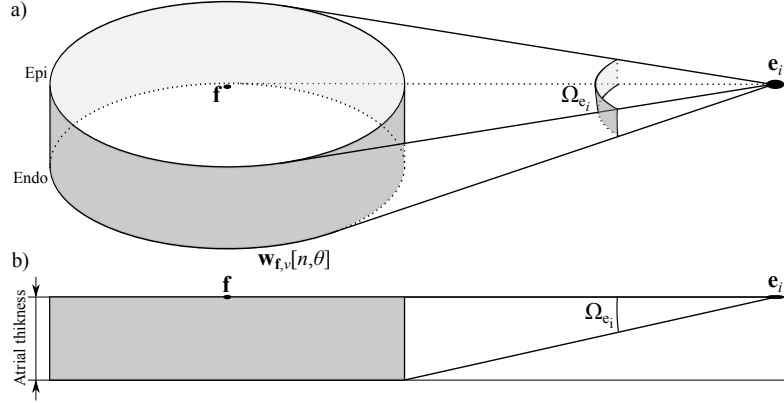


Figure 3.2: Schematic in: a) perspective view and b) lateral view, of the solid angle Ω_{e_i} obtained at electrode position e_i from a circular activation pattern $w_{f,v}[n, \theta]$ subtended within a UDL shown as a closed grey strip.

u-EGM signals as the mean value of all amplitude difference between the positive and negative deflection (i.e., the R-wave and S-wave, respectively). This constant value does not affect the rest of spatiotemporal features of $s_i[n]$, and therefore has been set arbitrarily to $V_d = 1$.

3.2.4 Estimation of Tissue Conduction Velocity

To use the propagation model (3.1), the conduction velocity of the cardiac tissue v needs to be estimated from recorded u-EGMs. Estimation of conduction velocity from invasive data is an already addressed problem (e.g. in [41, 116–118]), although difficult due to the spatiotemporal changes of cardiac tissue properties, especially during irregular tachycardias [116].

Estimation of conduction velocity based on LATs can be sensitive to detection errors. Therefore, an alternative approach inspired in that presented by *Fitzgerald et al.* [117] is used. The time delay δ_i between each u-EGM $s_i[n]$ and the central electrode of the 5×5 group being analysed $s_r[n]$ is obtained by maximizing the normalized cross-covariance function:

$$\delta_i = \arg \max_m \{C_{i,r}[m]\}, \quad (3.3)$$

$$C_{i,r}[m] = \frac{\sum_n (s_i[n] - \bar{s}_i)(s_r[n+m] - \bar{s}_r)}{\sqrt{\sum_n (s_i[n] - \bar{s}_i)^2 \sum_n (s_r[n] - \bar{s}_r)^2}}, \quad (3.4)$$

where \bar{s}_i and \bar{s}_r stand for the mean value of $s_i[n]$ and $s_r[n]$, respectively; and m represents the time lag between signals.

The next step involves the parametric estimation of the conduction velocity for the 5×5 electrode analysing mask while avoiding the possible effect of electrode bad contact, noise or conduction blocks. A biquadratic model is fitted to the delays measured

from each 3×3 sub-group of electrodes at $k = 1 \dots 4$ corners of the complete 5×5 group following [116]:

$$D^k(x, y) = a_1 + a_2x + a_3y + a_4xy + a_5x^2 + a_6y^2, \quad (3.5)$$

where $a_1 \dots a_6$ are the coefficients of the bi-quadratic model estimated in the least square sense [116]. Only those fitted models with root mean square error (RMSE) ≤ 1.5 ms were considered valid [114]. Then, the velocity vector field can be obtained by partial differentiation of $D^k(x, y)$ following [116]:

$$\hat{\mathbf{v}}^k(x, y) = \begin{bmatrix} \frac{dx}{dD^k} \\ \frac{dy}{dD^k} \end{bmatrix} = \begin{bmatrix} \frac{\dot{D}_x^k}{(\dot{D}_x^k)^2 + (\dot{D}_y^k)^2} \\ \frac{\dot{D}_y^k}{(\dot{D}_x^k)^2 + (\dot{D}_y^k)^2} \end{bmatrix}, \quad (3.6)$$

where $\dot{D}_x^k = \partial D^k(x, y) / \partial x$ and $\dot{D}_y^k = \partial D^k(x, y) / \partial y$. The estimated velocity vectors $\hat{\mathbf{v}}_i^k$ were obtained by evaluating (3.6) at each electrode location $[x_i, y_i]^\top$. Then, for each k th 3×3 sub-group of electrodes, an estimated conduction velocity is obtained for all $i \in k$ th corner as:

$$\hat{v}_k = \text{median} \{ \|\hat{\mathbf{v}}_i^k\| \}. \quad (3.7)$$

Finally, the conduction velocity \hat{v} for the complete 5×5 group of electrodes is estimated by averaging \hat{v}_k from each of the $K \leq 4$ corners with valid model fitting:

$$\hat{v} = \frac{1}{K} \sum_{k=1}^K \hat{v}_k. \quad (3.8)$$

3.2.5 Focus Initialisation

The focus location \mathbf{f} in (3.1) is estimated by means of the iterative algorithm introduced in section 3.2.1. The initialisation process of \mathbf{f} (step 1) is explained in this section.

The relation between the amplitude of the R-wave and S-wave of the u-EGMs is influenced by wavefront curvature and distance to the source of activation [6, 114]. A QS morphology (i.e., absence of R-wave) indicates that the electrode is located at the origin of the activation whereas RS morphology (i.e., equal R-wave and S-wave amplitudes) indicates activation by a planar wave [6, 53–56], as illustrated in Fig. 3.3. In order to take into account these characteristics, for each i th electrode signal $s_i[n]$, the R-S ratio has been quantified as the difference between R-wave and S-wave amplitude normalized by the peak-to-peak amplitude of the u-EGM signal [114]:

$$\mathcal{R}_{\text{RS}}^i = \frac{|R_i| - |S_i|}{|R_i| + |S_i|}, \quad (3.9)$$

where R_i and S_i stand for the R-wave and S-wave amplitudes of $s_i[n]$. This ratio ranges from -1 to 1 , where negative values show predominance of S-wave over R-wave and vice versa [114].

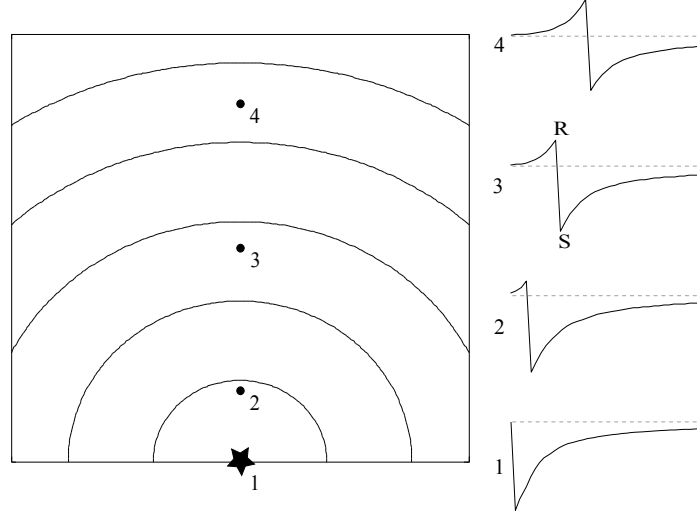


Figure 3.3: R-to-S ratio evolution with distance to the activation focus: the u-EGM measured at site 1 has pure S-wave morphology, thus is located at the source of the activation (indicated by a star); site 2 has nearly QS morphology ($\mathcal{R}_{RS}^i = -0.9$) and since sites 3 and 4 are distal from the source of activation, the measured u-EGM signal at those sites evolves to an RS morphology. The grey dashed line indicates the zero level. Curved lines show the evolution of the activation wavefront in 5 ms time-steps.

The initial focus \mathbf{f}_0 is set to the location of the electrode i_{min} that minimizes the combined criterion:

$$i_{min} = \arg \min_i \{ \delta_i + \mathcal{R}_{RS}^i \}; \quad (3.10)$$

which favours an electrode location with early activation and negative R-S ratio.

3.2.6 Iterative Model Optimization Algorithm

An iterative algorithm modifies \mathbf{f} optimizing the fitting of the u-EGM signals derived from the propagation model (3.1) to the recorded data, while the conduction velocity \hat{v} estimated in section 3.2.4 remains unmodified.

The focus location is initialized at \mathbf{f}_0 and updated in each iteration l following

$$\mathbf{f}_{l+1} = \mathbf{f}_l + \Delta \cdot \mathbf{u}_l \cdot \Delta_t, \quad (3.11)$$

where Δ represents the update step, Δ_t the signal time resolution and \mathbf{u}_l is the unit update vector towards the direction that improves the synchronization between the modelled and recorded u-EGMs. The update step is set up as $\Delta = \hat{v}$ therefore, in each iteration, \mathbf{f} changes according to the distance that the activation wavefront travels in Δ_t ms. A schematic block diagram of this model optimization is shown in Fig. 3.4.

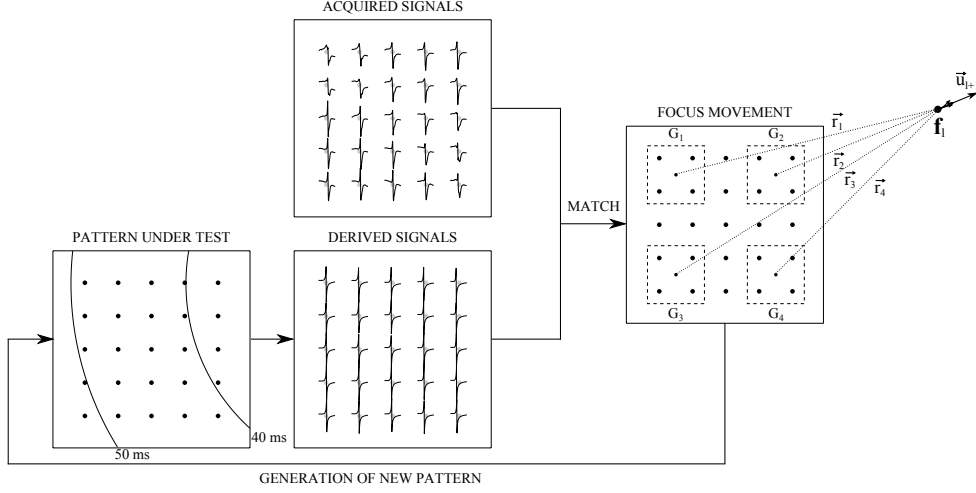


Figure 3.4: Schematic of the model optimization algorithm: signals are derived from the modelled propagation pattern under test and compared against the acquired u-EGM signals. Then, the algorithm decides a new focus location and the new pattern is tested. Direction vectors $\mathbf{r}_d, d = 1 \dots 4$ connect the center of each 2×2 corner group of electrodes G_d (indicated by dashed squares) to the activation focus \mathbf{f}_1 . Vector \mathbf{u}_i stands for the update vector for the next iteration. The signal amplitudes were scaled for visualization purposes as indicated in section 3.2.3. Note: Characters with arrows appear boldface in text.

The synchronization between the recorded and the modelled u-EGMs is quantified by the delay τ_i , maximizing the cross-covariance function:

$$\tau_i = \arg \max_m \{C_i[m]\}, \quad (3.12)$$

$$C_i[m] = \frac{\sum_n (s_i[n] - \bar{s}_i)(\hat{s}_i[n+m] - \hat{\bar{s}}_i)}{\sqrt{\sum_n (s_i[n] - \bar{s}_i)^2 \sum_n (\hat{s}_i[n] - \hat{\bar{s}}_i)^2}}, \quad (3.13)$$

where \bar{s}_i and $\hat{\bar{s}}_i$ stand for the mean value of $s_i[n]$ and $\hat{s}_i[n]$, respectively; and m represents the time lag between signals.

Then, each 2×2 sub-group of electrodes $G_d, d = 1 \dots 4$, located at the corners of the complete 5×5 group of electrodes under analysis (indicated within dashed squares in Fig. 3.4) has a “median sub-group delay” defined as:

$$\tilde{\tau}_d = \text{median}_{i \in G_d} \{\tau_i\}. \quad (3.14)$$

On the other hand, the director vector from each sub-group G_d to the focus \mathbf{f}_1 is defined as:

$$\mathbf{r}_d = \frac{\mathbf{f}_1 - \mathbf{g}_d}{\|\mathbf{f}_1 - \mathbf{g}_d\|}, \quad (3.15)$$

where \mathbf{g}_d stands for the center coordinates of G_d .

Finally, the unit update vector \mathbf{u}_l for the next iteration is determined by:

$$\mathbf{u}_l = \sum_{d=1}^4 \frac{\tilde{\tau}_d}{\sum_d |\tilde{\tau}_d|} \mathbf{r}_d, \quad (3.16)$$

$$\mathbf{u}_l = \frac{\mathbf{u}_l}{\|\mathbf{u}_l\|}, \quad (3.17)$$

whose direction depends on the sign of $\tilde{\tau}_d$.

This process is repeated until a cost function Q exceeds a threshold ϵ_Q or the maximum number of iterations is reached. The cost function Q is defined as:

$$Q = \text{mean}_i \{C_i[0]\}, \quad (3.18)$$

where $C_i[0]$ stands for the normalized cross-covariance value between the i th recorded and modelled u-EGM signals at zero delay, i.e., a measure of morphology similarity and synchronization. Therefore, Q can be interpreted as the average resemblance level between recorded and the signals derived from the activation pattern in test.

When $Q \geq \epsilon_Q$, the algorithm is terminated. This threshold value was set empirically to $\epsilon_Q = 0.85$. In case the algorithm meets the maximum number of iterations without reaching the threshold for Q , the location \mathbf{f}_l with maximum Q is chosen.

The algorithm embeds protection against oscillating solutions, avoiding getting stuck in local maxima by means of: 1) *Inertia movements* that increase the value Δ in (3.11) by 10 % during a maximum of 5 iterations while Q is not increasing and use the update vector \mathbf{u}_l of the last iteration l which increased Q ; and when inertia movements do not increase Q after 5 iterations, it uses 2) *random transition vectors* which move the focus location \mathbf{f}_l in random perpendicular directions to \mathbf{u}_l , replacing those random perpendicular vectors the update term $\Delta \cdot \mathbf{u}_l$ in (3.11).

As an overview, for each 5×5 group of electrodes, the algorithm outcomes are: the estimated conduction velocity \hat{v} , the final focus location \mathbf{f}_l , and the final cost function Q value which evaluates the solution fitting. Additionally, “*loci maps*”, which display the direction of local propagation, can be built by representing the focus location \mathbf{f}_l for each 5×5 group of electrodes in the MEA.

3.2.7 Reconstruction of Activation Maps

After analysing all the 5×5 groups of electrodes available in the complete MEA sensor, the activation sequence is obtained as explained in this section.

Each j th electrode, $j = 1 \dots 124$, of the MEA sensor lies in $h = 1 \dots h_j$ different 5×5 groups of electrodes, and therefore has h_j different LAT estimates $n_j(1) \dots n_j(h_j)$ and h_j different cost function values $Q_j(1) \dots Q_j(h_j)$. Each $n_j(h)$ was identified as the sample with maximum negative slope in the modelled signal $\hat{s}_{j,h}[n]$ from the j th electrode contained in the h th 5×5 group. Each u-EGM signal $\hat{s}_{j,h}[n]$ is obtained accordingly to (3.2), after the substitution of \hat{v}_h and $\mathbf{f}_{l,h}$ in (3.1).

A unique LAT estimate \hat{n}_j is obtained for each j th electrode as the weighted averaging of the individual LAT estimates using Q_j as weights:

$$\hat{n}_j = \left\lfloor \frac{\sum_{h=1}^{h_j} Q_j(h)n_j(h)}{\sum_{h=1}^{h_j} Q_j(h)} \right\rfloor, \quad (3.19)$$

where $\lfloor \cdot \rfloor$ stands for the nearest integer operator.

For robust LAT estimation, the number of solutions taking part of the map reconstruction in (3.19) were limited using the threshold ξ :

$$\xi = \min \{ \mu_Q - 2\sigma_Q, 0.55 \}, \quad (3.20)$$

where μ_Q and σ_Q stand for the mean and SD of the Q values for all analysed 5×5 electrode groups, respectively. Therefore, when $Q_j(h) < \xi$, the activation time $n_j(h)$ is not considered in the computation of (3.19). The value 0.55 is set empirically as a lower bound for Q in order to consider a reliable LAT solution.

3.3 Estimation of High-Density Activation Maps

3.3.1 Testing Database

The algorithm presented in this chapter was evaluated using clinical data obtained from a patient admitted for open chest surgery at Erasmus Medical Center Rotterdam (Rotterdam, The Netherlands) in whom an intraoperative electrophysiological study was performed. The patient is a 61 years-old male with coronary artery disease (CAD) and no history of AF, in whose echocardiographic examination revealed a normal left ventricular ejection fraction and normal atrial dimensions. The patient was informed and signed the consent form.

During the intervention, a custom-made high-density MEA mapping sensor (*Applied Biomedical Systems B.V., Maastricht, The Netherlands*) was positioned on the epicardial wall of the left and right atrium following a sequence of epicardial locations, as illustrated in Fig. 3.5(a). Datasets of high-density u-EGMs signals were acquired during SR and (electrically induced) AF.

The dimensions of the MEA sensor are 3.0×1.4 cm, and is composed of 128 circular gold plated electrodes (2 mm inter-electrode distance, 1 mm diameter) organized in an 8×16 rectangular grid. Electrode channels corresponding to each corner of the mapping array were not available for mapping and were reserved for storing surface ECG, reference and calibration signals, resulting in 124 u-EGM signals available for analysis (Fig. 3.5(b)). The acquired u-EGM signals were band-pass filtered (1-500 Hz) sampled and digitized at 1 kHz. The recording length during SR episodes was 5 s and 10 s during (electrically induced) AF episodes.

Automatic LAT detection was performed off-line after the procedure, using a wavelet-based algorithm [119] and subsequently audited by an expert electrophysiologist. Therefore, the resulting LATs were considered as “*gold standard*” for performance evaluation.

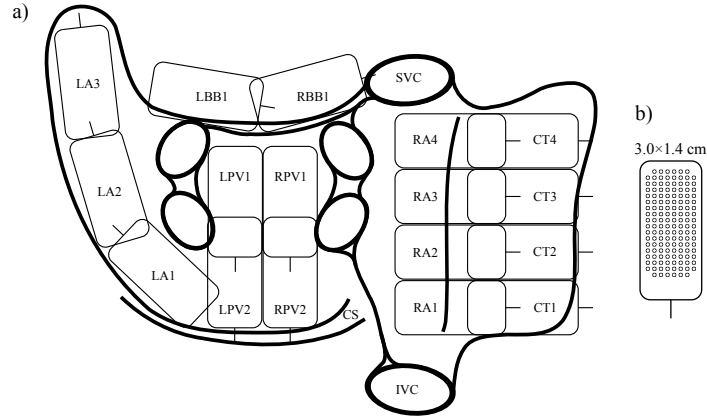


Figure 3.5: Schematic of the mapping procedure in posterior view: a) anatomical location of the MEA sensor in the atrium and b) MEA sensor used for mapping procedure. CS: coronary sinus, CT: crista terminalis, IVC: inferior vena cava, LA: left appendage, LBB: left Bachmann bundle, LPV: left pulmonary vein, RA: right appendage, RBB: right Bachmann bundle, RPV: right pulmonary vein, SVC: superior vena cava.

3.3.2 Evaluation Protocol

Activation maps were classified according to the following 7 degrees of activation pattern complexity, illustrated in the upper part of Fig. 3.6, the two first corresponding to SR patterns and the rest for AF patterns:

1. Normal sinus rhythm (NSR): Normal propagation of a single wavefront within the mapping catheter during SR (see Fig. 3.6(a)).
2. Abnormal sinus rhythm (ASR): Abnormal propagation of one or more wavefronts within the mapping catheter during SR (see Fig. 3.6(b)).
3. Single atrial fibrillation wavefront (SAFW): Single AF wavefront propagating within the mapping catheter whose origin is located outside the mapping array (see Fig. 3.6(c)).
4. Breakthrough (BT): Concentric AF propagation wavefront whose focus is located within the mapping array [45] (see Fig. 3.6(d)).
5. Atrial fibrillation wave fusion (AFWF): Two separated AF wavefronts collide and fuse into a single wavefront (see Fig. 3.6(e)).
6. Line of Block (LB): A line of block is present in the propagation pattern of the mapping catheter creating longitudinal dissociation of AF wavefronts travelling at different velocities and/or directions [46] (see Fig. 3.6(f)).
7. Complex AF (CAF): Chaotic AF activation with wave interruption and multiple lines of block (see Fig. 3.6(g)).

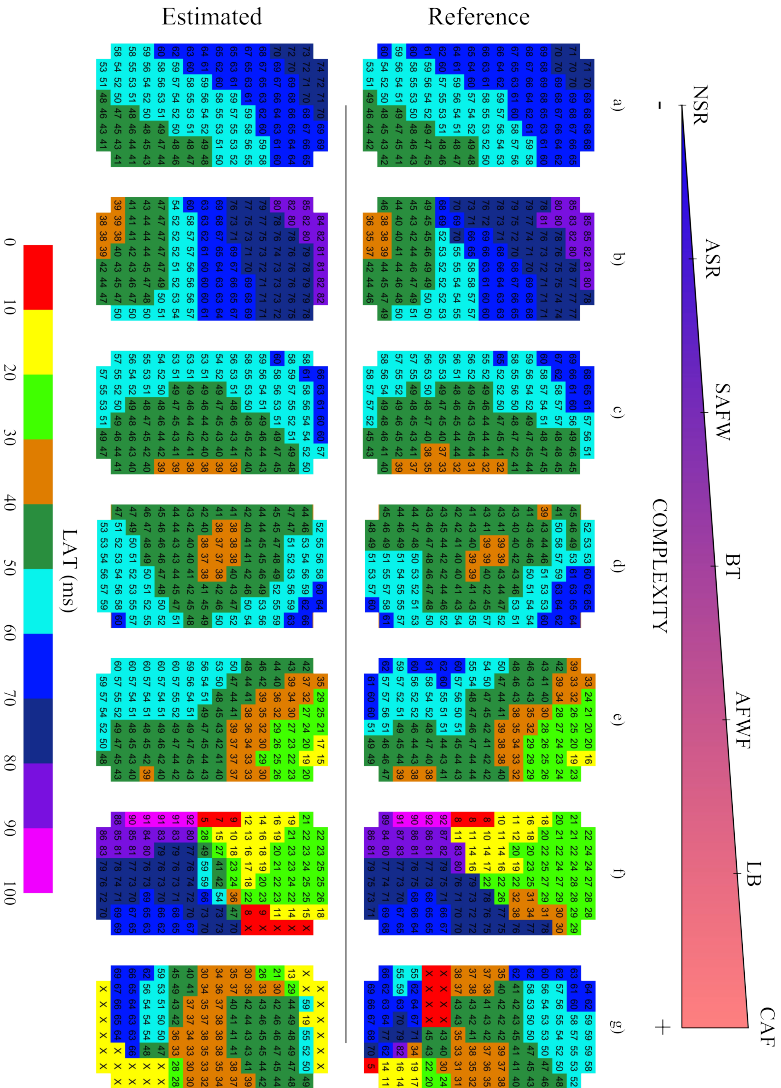


Figure 3.6: Representative examples of the proposed atrial activity complexity classes. Reference and estimated activation maps were shown in: a) normal sinus rhythm (NSR) activity (error: -0.31 ± 0.93 ms, area: 100 %), b) abnormal sinus rhythm (ASR) activity (error: -0.23 ± 3.5 ms, area: 100 %), c) single atrial fibrillation wavefront (SAFWF) activity (error: -0.03 ± 2.96 ms, area: 100 %), d) breakthrough (BT) associated atrial activity (error: -0.27 ± 2.59 ms, area: 100 %), e) atrial fibrillation wave fusion (AFWF) activity (error: -0.12 ± 1.73 ms, area: 100 %), f) dissociated atrial activity due to a line of block (LB) (error: 0 ± 13.52 ms, area: 95.97%) and g) complex atrial fibrillation (CAF) activity (error: -5.3 ± 10.55 ms, area: 80.17 %). LATs are colour-coded from red (earliest) to pink (latest) in 10 ms isochronal areas. In case of no LAT could be identified at one electrode location, a cross is used.

The evaluation is performed by comparing the estimated LATs with those audited by an expert electrophysiologist, showing this error as mean \pm SD. Moreover, the percentage of the area of the MEA sensor with valid estimated LATs is measured for each map. Spearman's rank correlation ρ_s has been computed for LAT assessment. Additionally, Lin's concordance correlation factor ρ_c [95] and Bland-Altman analysis were used to assess agreement between the measurements. A p -value ≤ 0.05 was required for considering statistical significance.

Additionally, sensitivity Se and positive predictive value P^+ of the detection have been computed as:

$$Se = \frac{TP}{TP + FN}, \quad (3.21)$$

$$P^+ = \frac{TP}{TP + FP}, \quad (3.22)$$

where TP stands for the number of true detections, FN stands for the number of missed detections and FP stands for the number of false detections. A tolerance of ± 5 ms respect to the expert reference LATs was used to consider a true detection.

3.3.3 Results

Analysis of Sinus Rhythm Recordings

Table 3.1 summarizes the results obtained from the analysis of SR recordings. Note that in contrast to recordings at $RA1$ to $RA3$, recording at position $RA4$ shows abnormal SR activity suggesting a stable functional reentrant circuit (illustrated in Fig. 3.6(b)) which is present during the complete recording time.

The global error obtained with the presented method is -0.66 ± 2.00 ms across 3100 LAT measurements, thus covering the 100 % of the sensor area. A high level of agreement is confirmed by high Spearman's correlation ($\rho_s = 0.98$, $p < 0.01$) and high Lin's concordance correlation factor ($\rho_c = 0.98$, $p < 0.01$) as shown in Fig. 3.7. The Bland-Altman analysis illustrated in Fig. 3.7(b) shows no trend in LAT estimation (Pearson's $\rho = -0.01$, $p = 0.73$). Moreover, the detection performance is also high with $Se = 100$ % and $P^+ = 97.84$ %. Those observations confirm the high agreement between measurements during SR as illustrated in Fig. 3.6(a)–(b).

Analysis of Atrial Fibrillation Recordings

Table 3.2 summarizes the results obtained from the analysis of AF recordings. Note that LB and CAF complexity levels were only present at recording $RA1$. The global error obtained by evaluating a total of 28226 different LATs is -0.83 ± 6.02 ms covering almost the complete MEA sensor area (97.99 ± 7.66 %). The LAT estimation has high agreement with manual annotations indicated by Spearman's $\rho_s = 0.93$ and Lin's concordance correlation factor $\rho_c = 0.90$ ($p < 0.01$ both). Moreover, the detection performance is also high with $Se = 97.80$ % and $P^+ = 88.36$ %. Representative examples of activation map reconstruction during AF are shown in Fig. 3.6(c)–(g).

Table 3.1: Detection error (mean \pm SD), Spearman’s correlation ρ_s , Lin’s concordance correlation factor ρ_c , sensitivity and positive predictive value of comparing estimated LATs with the manual reference in SR recordings. N/A stands for Not Applicable

Loc.	Maps (#)	LATs (#)	Area (%)	Error (ms)	NSR (#)	ASR (#)	ρ_s	ρ_c	Se (%)	P^+ (%)
<i>RA1</i>	6	744	100	-0.82 ± 1.41	6	N/A	0.99*	0.99*	100	98.66
<i>RA2</i>	6	744	100	-0.78 ± 0.92	6	N/A	$\sim 1^*$	0.99*	100	100
<i>RA3</i>	6	744	100	-0.44 ± 0.76	6	N/A	$\sim 1^*$	$\sim 1^*$	100	100
<i>RA4</i>	7	868	100	-0.62 ± 3.36	N/A	7	0.97*	0.97*	100	93.43
Total	25	3100	100	-0.66 ± 2.00	18	7	0.98*	0.98*	100	97.84

* indicates a p -value < 0.01 .

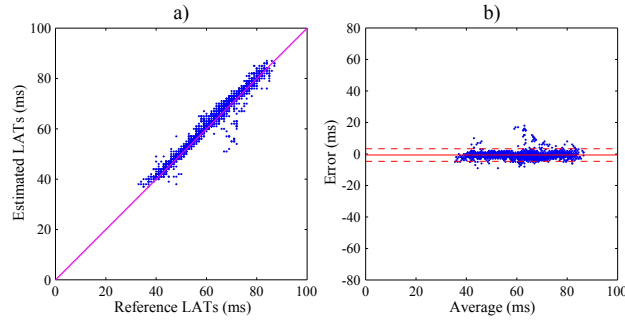


Figure 3.7: Agreement evaluation between reference and estimated LATs during SR: a) scatterplot for Lin’s concordance correlation factor ρ_c analysis, where pink line indicates the unit slope and b) Bland-Altman plot where red solid line indicates mean error and red dashed lines show mean \pm 2SD of the error.

The Bland-Altman analysis illustrates this agreement (see Fig. 3.8(f)), showing that the proposed method has a slight trend towards over-estimation of early LATs and sub-estimation of late LATs (Pearson’s $\rho = 0.21$, $p < 0.01$). LAT agreement analysis for each AF complexity level is shown in Fig. 3.8(a)–(e). A high level of agreement is found for SAFW, BT and AFWF (Fig. 3.8(a)–(c)), whereas LB and CAF show lower level of agreement (Fig. 3.8(d)–(e)).

The “*Loci Maps*”

Aside from the activation map reconstruction, an interesting result of the introduced spatiotemporal approach is the estimation of the activation pattern origin \mathbf{f} for a given 5×5 group of electrodes of the MEA sensor. Therefore, construction of “*loci maps*” is possible by plotting all estimated focus location \mathbf{f} across the MEA sensor. Figure 3.9 shows examples of these *loci maps* from different activation patterns. Note that *loci maps* spatially follow the potential activation wavefront evolution, providing extra information to complement the activation map.

Table 3.2: Detection error (mean \pm SD), Spearman's correlation ρ_s , Lin's concordance correlation factor ρ_c , sensitivity and positive predictive value of comparing estimated LATs with the manual reference by AF recording at different levels of complexity.

Loc.	Type	Maps (#)	LATs (#)	Error (ms)	Area (%)	ρ_s	ρ_c	Se (%)	P^+ (%)
<i>RA1</i>	SAFW	27	33141	-1.05 ± 4.33	95.59 ± 13.98	0.95*	0.92*	95.42	92.87
	BT	3	350	-0.58 ± 4.74	97.62 ± 4.12	0.88*	0.80*	97.43	86.57
	AFWF	3	359	-1.91 ± 7.39	98.62 ± 1.71	0.90*	0.83*	98.26	78.55
	LB	7	789	-2.39 ± 15.25	91.70 ± 8.84	0.74*	0.67*	87.11	60.84
	CAF	10	903	-7.60 ± 20.26	83.36 ± 23.09	0.46*	0.38*	62.23	35.21
	Total	50	5542	-2.33 ± 11.01	92.91 ± 15.43	0.79*	0.68*	91.16	77.59
<i>RA2</i>	SAFW	44	5419	-1.09 ± 3.41	99.50 ± 1.81	0.96*	0.95*	99.47	93.17
	BT	2	238	-3.01 ± 3.61	100	0.95*	0.93*	100	81.51
	AFWF	15	1823	-1.09 ± 4.15	99.11 ± 1.66	0.95*	0.95*	99.04	90.78
	Total	61	7480	-1.15 ± 3.63	99.42 ± 1.74	0.96*	0.95*	99.38	92.22
<i>RA3</i>	SAFW	15	1883	-0.12 ± 2.94	98.55 ± 2.00	0.97*	0.96*	98.48	95.64
	BT	43	5298	-0.11 ± 3.47	99.46 ± 0.96	0.95*	0.95*	99.41	92.26
	AFWF	2	242	0.22 ± 3.24	97.58 ± 3.42	0.92*	0.90*	97.38	92.15
	Total	60	7373	-0.10 ± 3.33	99.17 ± 1.43	0.96*	0.96*	99.10	93.10
<i>RA4</i>	SAFW	53	6478	-0.16 ± 4.21	99.42 ± 1.41	0.96*	0.96*	99.35	87.90
	BT	4	484	0.92 ± 6.70	99.57 ± 0.48	0.84*	0.81*	99.51	83.20
	AFWF	7	865	-0.67 ± 3.95	99.88 ± 0.31	0.96*	0.94*	99.87	90.06
	Total	64	7831	-0.14 ± 4.39	99.48 ± 1.30	0.96*	0.95*	99.42	87.84
All	SAFW	139	16871	-0.62 ± 3.90	98.61 ± 6.43	0.96*	0.96*	98.52	91.36
	BT	52	6374	-0.17 ± 3.94	99.38 ± 1.28	0.94*	0.94*	99.33	90.85
	AFWF	27	3289	-0.97 ± 4.54	99.14 ± 1.59	0.95*	0.93*	99.06	89.36
	LB	7	789	-2.39 ± 15.25	91.70 ± 8.84	0.74*	0.67*	87.11	60.84
	CAF	10	903	-7.60 ± 20.26	83.36 ± 23.09	0.46*	0.38*	62.23	35.21
	Total	235	28226	-0.83 ± 6.02	97.99 ± 7.66	0.93*	0.90*	97.80	88.36

* indicates a p -value < 0.01 .

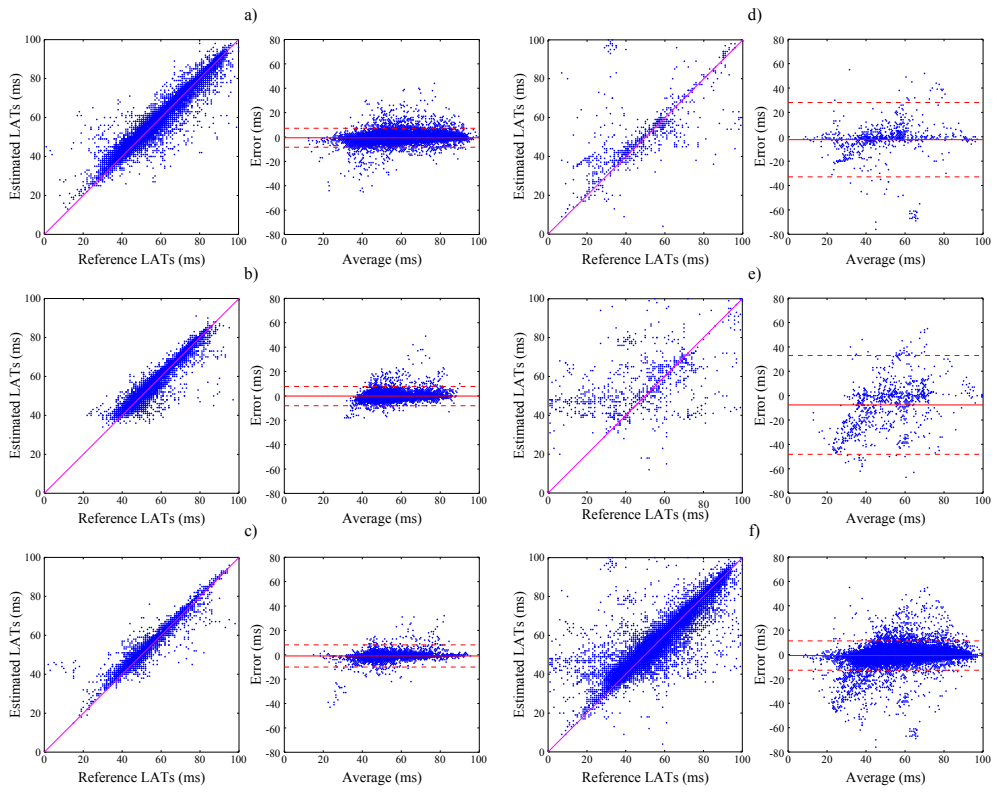


Figure 3.8: Agreement evaluation between reference and estimated LATs during AF at different complexity levels including a) SAFW, b) BT, c) AFWF, d) LB e) CAF and f) all studied maps. In each pair of panels, the one at the left shows the scatterplot for Lin's concordance correlation factor ρ_c analysis (pink line indicates the unit slope) and the one at the right shows the Bland-Altman plot (red solid line indicates mean error and red dashed lines show mean $\pm 2SD$ of the error).

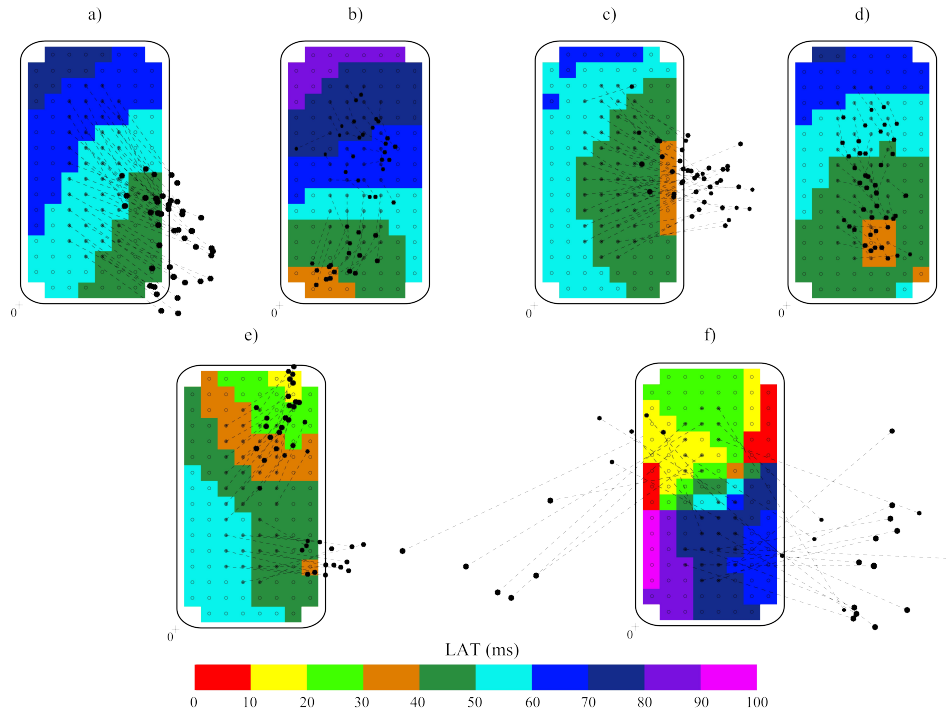


Figure 3.9: Examples of *loci map* merged with the estimated activation map: a) NSR, b) ASR, c) SAFW, d) BT, e) AFWF and f) LB. LATs are colour-coded from red (earliest) to pink (latest) in 10 ms isochrones. Electrodes are shown as empty circles and each focus solution f is shown in black dots connected with the center electrode of its corresponding 5×5 group. Spatial reference is shown with a cross.

These *loci maps* show different wavefront behaviour and properties, e.g., the number of wavefronts coming through the catheter and their directions (see Fig. 3.9(e)–(f)), curved wavefronts due to potential reentrant circuits (see Fig. 3.9(b)) and tissue anisotropy explained by small cluster of foci coming from the same place but moving into different directions, presumably following the cardiac fibres orientation (see Fig. 3.9(a)).

3.4 Discussion

Automatic LAT detection during AF relies in the detector accuracy and often requires manual checking. Moreover, classic LAT detection reduces the activation information to just a binary signal which takes values whether an activation is found, rejecting the remaining spatiotemporal information embedded in the morphology as well as the relation between adjacent electrodes.

This chapter introduces an integrated activation detection scheme, which takes benefit of the relation between close u-EGMs, hence providing a spatiotemporal detection of LATs for high-density activation maps in recordings using MEA sensors. The rationale behind this technique is that it is possible to decompose a complete (and complex) activation pattern into a combination of simpler activation patterns fitted to small areas of the MEA sensor. The simplest activation pattern is concentric and isotropic, and therefore only depends on the location of the activation origin and the tissue conduction velocity.

The algorithm introduces the parameters of the activation pattern into a UDL model of the tissue, deriving the corresponding u-EGM signals. Model pattern parameters were iteratively modified by comparing the resulting u-EGM signals against the recorded ones in order to reach a maximum shape similarity and synchronization between recorded and derived signals. Finally, the complete activation map is reconstructed by combination of all solutions obtained by running this iterative process over the complete MEA sensor.

3.4.1 Detection Performance

Mapping performance has been evaluated by comparing the estimated LATs with those obtained manually by an expert electrophysiologist in recordings during SR and AF. Additionally, activation maps were studied and classified based on a complexity scale, hence providing a more complete view of the method's behaviour and usefulness. The used complexity classification is similar to those activation modes identified by *Kuklik* and co-workers in an hypertensive sheep cardiac model [120].

The agreement between manual and estimated LATs during SR was proved to be very high. The error was -0.66 ± 2.00 ms with very high Spearman's correlation and Lin's concordance correlation factor ($\rho_s = 0.98$ and $\rho_c = 0.98$, $p < 0.01$ both). An exceptional situation was found among those recordings during SR. The cranial location of the MEA sensor over the right atrium (*RA4* recording) shows full abnormal atrial activity during SR. This activity suggests the presence of a re-entrant circuit, identified by the proposed method, as illustrated in Fig. 3.6(b). Moreover, the novel proposed *loci maps* sketch potential trajectory of the activation wavefront evolution, suggesting the presence of a curved wavefront due to a functional reentry present during SR (see Fig. 3.9(b)).

The LAT estimation error was of -0.83 ± 6.02 ms with high agreement with manual annotations ($\rho_s = 0.93$ and $\rho_c = 0.90$, $p < 0.01$ both) during AF. This agreement is even higher considering the SAFW, BT and AFWF maps solely, which correspond to the 93 % of the studied maps. However, much lesser agreement was found in higher complexity maps (LB and CAF). Nevertheless, those types of patterns were poorly represented in the available data (only at recording location *RA1*), limiting the conclusions that can be obtained from those classes.

Comparing the mean error in LAT estimation with the standard error of the mean, for each atrial rhythm and atrial location, it is shown that the proposed method presents a statistically significant bias. However, in 80 % of SR maps and 66 % of AF

maps, this bias is below one sampling interval and in 100 % of SR maps and 89 % of AF maps this bias is below two sampling intervals. Moreover, it must be noted that having a systematic bias is not crucial in activation mapping, where stability between the measurements at different sites is pursued. This is quantified by the error standard deviation and the correlation with the reference annotations.

3.4.2 Spatiotemporal Mapping Approach

The introduced algorithm for spatiotemporal activation mapping was possible due to the iterative process and the small computation times of the solid angle and UDL approaches, in contrast to the high computation times of more classic and detailed tissue simulation approaches [121]. However, the proposed method needs manual assistance to select the time interval in which to analyse the activation map; therefore, the presented method is a semi-automatic approach.

Smoother and more comprehensive activation maps were obtained using the proposed algorithm compared with those obtained manually, as illustrated by Fig. 3.6. This fact is in concordance with the smoothing nature of the weighted average process for reconstructing the final activation maps. Additionally, the modelled activation pattern used for LAT estimation also contributes to this smoothness. As an additional outcome of the iterative process, the *loci maps* appear to be an interesting tool for assessing the activation behaviour and track the wavefront evolution in the activation map under analysis.

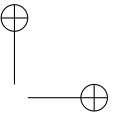
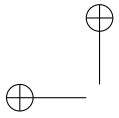
3.4.3 Limitations

The isotropic concentric activation model assumes the presence of a single wavefront at the time of mapping within each 5×5 sensors analysis mask. This assumption is not always accomplished and may be the reason behind the lower performance observed in the more complex AF activity levels. Small lines of block or high frequency (short wavelength) atrial activity may yield in poor estimation of the tissue conduction velocity or small values of the cost function due to the impossibility of the activation pattern to model the underlying activation behaviour. One possible solution is to select a smaller group of electrodes. Reducing the analysis mask size may allow to better estimate activations under those situations but also turns into a limitation because the estimation of tissue conduction velocity could be less accurate and/or less robust to data acquisition errors (i.e., non-contact of electrodes) and noise.

Another limitation is related to the studied database. Only one set of locations coming from the same patient have been studied. It must be noted the singularity of the data used as well as the fact that manual annotations and/or checking during AF of 124 channels is a high time-consuming task, constraining the possible database size. However, more than 30000 LATs combining SR and AF recordings were studied, thus making a high amount of measurements for evaluating the proposed methodology. Nevertheless, extension to more patients and more atrial locations is needed, especially in those left atrial locations where more complex activity can be expected.

3.5 Conclusion

This chapter presents an integrated spatiotemporal estimation approach that allows to obtain smooth and comprehensive high-density activation maps and to track the underlying wavefront evolution. Simplified local activation pattern and tissue models are used in order to generate u-EGM signals resembling the measured activation map using an iterative process. Results indicate high accuracy of the proposed method compared against manually audited annotations during SR and AF. Therefore, although validation was conducted using invasive data, it opens the possibility of studying high-density activations maps with robust outcomes and the development of minimally invasive high-density mapping.



“You’re reversing causality. Dreams don’t trigger events-events trigger dreams; our experiences feed our minds.”

*The Supernatural Enhancements by
Edgar Cantero*

Chapter 4

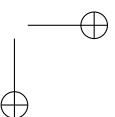
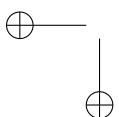
Causal Characterisation of Atrial Activity

4.1 Introduction	
4.1.1 Classification and Treatment of Atrial Fibrillation	
4.1.2 Quantitative Methods for Atrial Fibrillation Analysis	
4.1.3 Motivation	
4.2 The Predictability Framework	
4.2.1 Multi-Variate Auto-Regressive Modelling	
4.2.2 Signal Pre-processing	
4.2.3 The Granger Causality and Predictability	
4.2.4 Measurement Framework	
4.3 Predictability Analysis of Atrial Fibrillation	
4.3.1 Testing Databases	
	4.3.2 Application of the Predictability Framework on Basket Catheter Data
	4.3.3 Statistical Analysis
	4.3.4 Results
	4.4 Discussion
	4.4.1 Quantification of the Regularity of Simulated Atrial Activity
	4.4.2 Activity Tracking Capability
	4.4.3 Comparison with Other Methods
	4.4.4 Limitations
	4.4.5 Clinical Relevance
	4.5 Conclusion

4.1 Introduction

4.1.1 Classification and Treatment of Atrial Fibrillation

Although AF is not a life threatening arrhythmia by itself, it is associated with increasing risk of stroke, heart failure, dementia and mortality [38]. Clinically, AF is classified



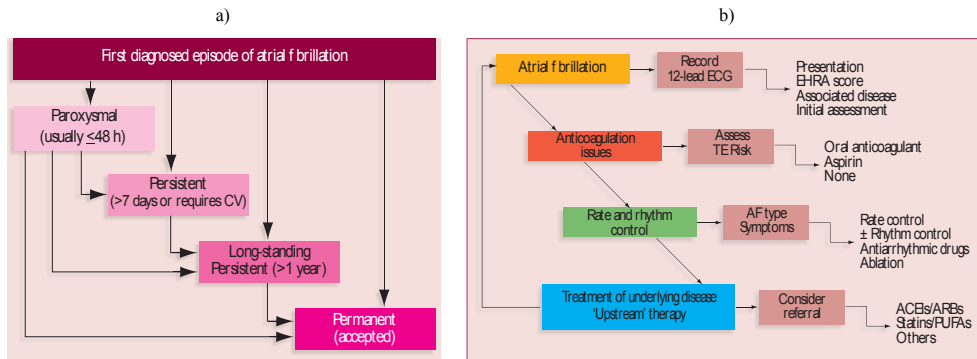


Figure 4.1: Classification and treatment of AF: a) classification and progression of the disease; b) treatment cascade. ACEI: angiotensin-converting enzyme inhibitor, ARB: angiotensin receptor blocker; CV: cardioversion, PUFA: polyunsaturated fatty acid, TE: trombo embolism. Reproduced from [59].

into five types depending on the presentation and duration of the episode [38, 59, 105] (See Fig. 4.1(a)):

1. First diagnosed AF: Every patient who has first time diagnosed AF is considered into this type, independently of the duration of the arrhythmia or the AF-associated symptoms.
2. Paroxysmal AF: The arrhythmia episode self-terminates within 48 hours. It may continue up to 7 days and will be highly recurrent.
3. Persistent AF: Recurrent arrhythmia episode lasting more than 7 days without self-terminating and requires cardioversion (either external or drug-induced).
4. Long-standing persistent AF: AF lasts for more than a year when it is decided to adopt a rhythm control strategy.
5. Permanent AF: The presence of the arrhythmia is accepted by the patient and physician and rhythm control strategy is not pursued.

The initial evaluation of a patient must be done in terms of the aforementioned arrhythmia classification prior to management and treatment, with importance of the determination of the arrhythmic event onset [38, 59].

Management and treatment of patients with AF aim to reduce symptoms and to prevent severe associated complications. These therapeutic goals need to be pursued in parallel, specially in those first-diagnosed AF cases. Antithrombotic management, rate control and adequate therapy of concomitant cardiac diseases are first therapeutic lines for prevention of AF-related complications. However, additional cardioversion, antiarrhythmic drug therapy or catheter ablation may be required to alleviate symptoms (See Fig. 4.1(b)) [59].

Catheter ablation is a reasonable therapy for rhythm control (i.e., maintain SR) for those patients whose anti-arrhythmic drug therapy is ineffective. Specially, it is justified in those paroxysmal AF patients or in those symptomatic AF patients whose quality of life can be improved and the risk of other complications can be reduced [59, 105].

Under a focal hypothesis of initiation and maintenance of AF coming from the pulmonary veins (PVs) [42]. PVs are the principal targets of catheter ablation, being this approach known as pulmonary vein isolation (PVI) [105]. The PVI approach performs linear lesions around the PV ostium close to the EAS of the PV musculature [105]. Additionally, complex fractionated atrial electrograms (CFAEs) ablation [122, 123] and linear lesions are common complements to the PVI ablation approach [105]. However, high recurrence rates in the first 6 to 12 months occur after AF catheter ablation due to many reasons such as PV reconnection, atrial remodelling or non-identified non-PV-related AF sources [105].

4.1.2 Quantitative Methods for Atrial Fibrillation Analysis

Aiming to increase the efficacy and outcomes of AF catheter ablation and to assist physicians in the decision process or in better understanding of AF mechanisms, quantitative EGM-based methods have been proposed. Those methods extract, process and quantify features of the EGM signal recorded using multi-electrode catheters (either in unipolar or bipolar configuration) pertinent to clinical AF [124–126].

In this context, some methods concentrate in the search of AF drivers assessing fibrillation rates, either in time domain (i.e., assessing LATs; e.g., in Fig. 4.2(a)) [77, 81, 82, 119, 127–131] or in frequency domain (i.e., analysing the fibrillation dominant frequency (DF); e.g., in Fig. 4.2(b)) [132–135]. Other methods quantify the regularity and organization of AF for searching areas responsible of AF maintenance [130, 136–141] (e.g., in Fig. 4.2(b)–(c)). Quantitative methods have also been proposed for identifying and quantifying areas with CFAEs in order to assist its identification during AF ablation procedures [142–144] (e.g., in Fig. 4.2(d)). Phase maps are also proposed as a mapping alternative for identification of spiral waves and rotors during AF [145–147] (e.g., in Fig. 4.2(e)). Causal relations between different atrial sites have been proposed to quantify signal interactions using parametric models represented either in the frequency [148, 149] or in the time domain [150–153] (e.g., in Fig. 4.2(f)).

4.1.3 Motivation

Some of the quantitative approaches proposed for AF activity analysis rely on activation detection and/or does not take into consideration the spatiotemporal relation between close electrodes. The influence of close electrodes may provide insights of the fibrillation process and therefore may help in the guidance of ablation procedures of AF. This chapter introduces a multi-variate predictability framework, based on the concept of Granger causality (GC), where causal interactions (in the sense of the GC)

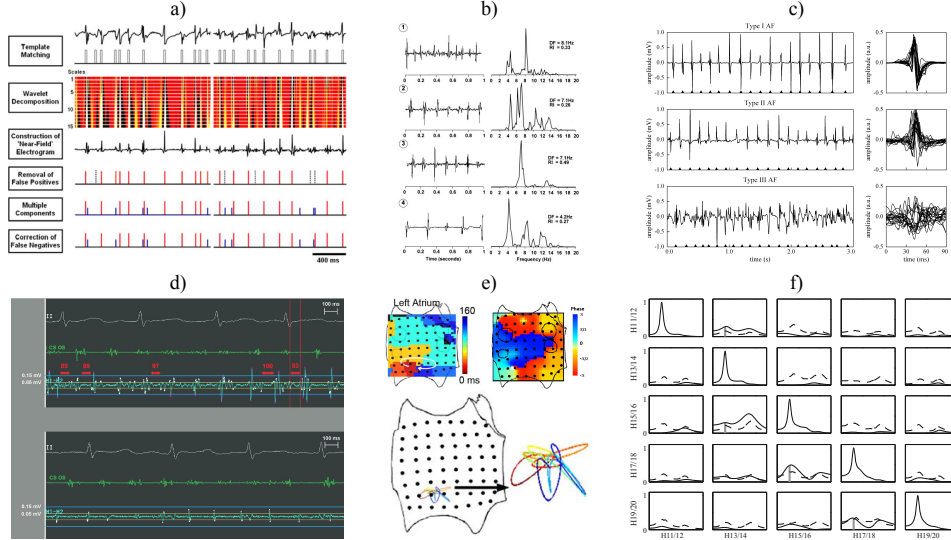


Figure 4.2: Examples of quantitative EGM-based methods for AF analysis: a) wavelet LAT detection (reproduced from [119]), b) spectral DF and regularity analysis (reproduced from [132]) c) activation morphology regularity analysis (reproduced from [138]) d) detection of CFAEs (reproduced and modified from [142]), e) phase map identifying a rotor and tip movement (reproduced and modified from [146]) and f) parametric analysis of AF propagation (reproduced from [148]).

between different atrial sites are analysed by considering the EGM signals as stochastic processes interacting with the neighbouring atrial sites by means of an information exchange driven by the atrial activity.

4.2 The Predictability Framework

4.2.1 Multi-Variate Auto-Regressive Modelling

Considering L -dimensional multi-variate stochastic processes $S = \{S_1, \dots, S_L\}$ that describe the activity of different electrodes on the atria. Each set of L simultaneous observations $\mathbf{s}(n) = [s_1(n), \dots, s_L(n)]^\top$ is assumed to be represented by a multi-variate auto-regressive (MVAR) model of order m :

$$\mathbf{s}(n) = \sum_{k=1}^m \mathbf{A}(k)\mathbf{s}(n-k) + \mathbf{v}(n), \quad (4.1)$$

where each $\mathbf{A}(k)$ is a $L \times L$ whose elements are the auto-regressive coefficients $a_{ij}(k)$, $i, j = 1 \dots L$, and $\mathbf{v}(n) = [v_1(n), \dots, v_L(n)]^\top$ is a multi-variate white noise process defined by its covariance matrix $\Sigma_{\mathbf{v}}$.

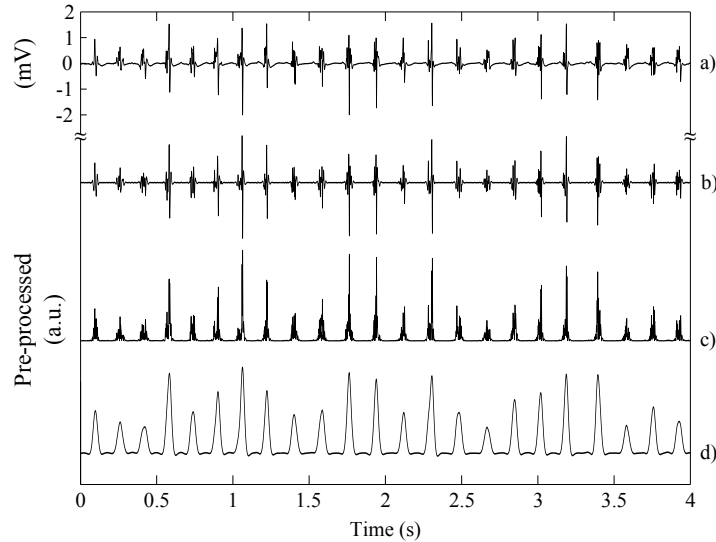


Figure 4.3: *Botteron* and *Smith* pre-processing chain [136]: a) original b-EGM signal, b) band-pass filtering (step 1), c) signal rectification (step 2) and d) low-pass filtering (step 3).

For a given observation $s(n)$, the MVAR coefficients matrices $\mathbf{A}(k)$ were estimated using the least-squares method [154] and the model order m was chosen in the range 1-15 as the value minimizing the Bayesian information criterion (BIC) [155]. In case the BIC did not reach a minimum, the model order m was chosen as the first one whose successive difference in BIC is smaller than the 5 % of the largest successive difference.

4.2.2 Signal Pre-processing

The b-EGM signals were pre-processed following the *Botteron* and *Smith* pre-processing chain [136]; consisting of three steps:

1. Band-pass filtering between 40 and 250 Hz, using a second order Butterworth infinite impulse response (IIR) filter.
2. Signal rectification.
3. Low-pass filtering with 25 Hz cut-off frequency, using a second order Butterworth IIR filter.

This pre-processing chain aims to enhance the rhythmic properties of atrial EGM signals, simplifying their shape variations while reducing noise, as illustrated in Fig. 4.3. Additionally, the pre-processed signals were downsampled to 100 Hz in order to provide sufficient information for the MVAR modelling while avoiding high model orders due to data redundancy.

4.2.3 The Granger Causality and Predictability

The GC is a measurement of predictability and precedence [156]. In a bivariate context where $L = 2$ processes are considered, i.e. $S = \{X, Y\}$, the source process X is said to be cause of the target process Y (in the sense of the GC) if the past of X contains information that helps to predict the future of Y over and above the information already contained in the past of Y [157].

Let $x' = x(n)$ denote the present value of a realization of the process X , let $\mathbf{x}^- = [x(n-m), \dots, x(n-1)]^\top$ denote the vector containing the m past values of X , and extend this notation to every considered process. Additionally, let $\sigma(A)$ be the variance of the process A and $\sigma(A|B)$ be the residual variance of the regression of the process A over the multi-variate process B . The residual variance was obtained from the parameters of the MVAR representation (4.1) using the method described in [158], which is based on the auto-covariance sequence of the MVAR process inferred from the estimated model parameters.

Then, the GC from the source process X to the target process Y can be written as [156, 159–161]:

$$\begin{aligned} G_{X \rightarrow Y} &= \ln \left(\frac{\sigma(y'|\mathbf{y}^-)}{\sigma(y'|\mathbf{y}^-, \mathbf{x}^-)} \right) \\ &= \ln(\sigma(y'|\mathbf{y}^-)) - \ln(\sigma(y'|\mathbf{y}^-, \mathbf{x}^-)), \end{aligned} \quad (4.2)$$

The above concept can be extended to the multi-variate case [156, 160], considering $L = 3$, where the observed process is $S = \{X, Y, Z\}$, being Y the target process and $\{X, Z\}$ the remaining source processes. In this extended framework, the *predictability* P_Y of the target process Y is defined as [161, 162]:

$$P_Y = \ln(\sigma(y')) - \ln(\sigma(y'|\mathbf{y}^-, \mathbf{x}^-, \mathbf{z}^-)), \quad (4.3)$$

measuring how much the present of the target process Y can be predicted from the knowledge of its own past and of the past of the other considered processes.

The predictability (4.3) can be decomposed into two terms, as follows [161]:

$$P_Y = S_Y + G_{XZ \rightarrow Y}, \quad (4.4)$$

where the first term represents the *self-predictability* of the process Y , quantifying how much of the uncertainty about the present of Y can be predicted just from its own past:

$$S_Y = \ln(\sigma(y')) - \ln(\sigma(y'|\mathbf{y}^-)), \quad (4.5)$$

and the second term represents the *joint Granger causality*, quantifying the remaining amount of uncertainty about the present of Y that could not be predicted by its own past but is predicted by the past of X and Z :

$$G_{XZ \rightarrow Y} = \ln(\sigma(y'|\mathbf{y}^-)) - \ln(\sigma(y'|\mathbf{y}^-, \mathbf{x}^-, \mathbf{z}^-)). \quad (4.6)$$

Moreover, $G_{XZ \rightarrow Y}$ can be further decomposed following the same decomposition process than for equations (4.4)–(4.6) [158], by either regressing first using the process X or Z , equivalently:

$$G_{XZ \rightarrow Y} = G_{X \rightarrow Y} + G_{Z \rightarrow Y|X} = G_{Z \rightarrow Y} + G_{X \rightarrow Y|Z}, \quad (4.7)$$

where $G_{X \rightarrow Y}$ and $G_{Z \rightarrow Y}$ stand for the *Granger causality* from X to Y and Z to Y , respectively, obtained according to (4.2). The terms $G_{Z \rightarrow Y|X}$ and $G_{X \rightarrow Y|Z}$ stand for the *conditional Granger causality* from Z to Y conditioned to the past of X , and from X to Y conditioned to the past of Z , respectively:

$$G_{Z \rightarrow Y|X} = \ln(\sigma(y'|y^-, \mathbf{x}^-)) - \ln(\sigma(y'|y^-, \mathbf{x}^-, \mathbf{z}^-)), \quad (4.8)$$

$$G_{X \rightarrow Y|Z} = \ln(\sigma(y'|y^-, \mathbf{z}^-)) - \ln(\sigma(y'|y^-, \mathbf{x}^-, \mathbf{z}^-)). \quad (4.9)$$

quantifying the influence of X or Z in Y , after removing the influence of the past of Y and the past of the other process, i.e. Z or X , respectively.

On the other hand, an alternative decomposition to (4.4) is [162]:

$$P_Y = C_{XZ \rightarrow Y} + G_{Y|XZ}, \quad (4.10)$$

where the first term stands for the *joint cross predictability* of Y from both processes X and Z , quantifying the amount of uncertainty about the present of Y that can be predicted solely from the past of X and Z taken together:

$$C_{XZ \rightarrow Y} = \ln(\sigma(y')) - \ln(\sigma(y'|\mathbf{x}^-, \mathbf{z}^-)), \quad (4.11)$$

and the second term quantifies the concept of *Granger autonomy* of Y , measuring the improvement in the prediction of the target process Y yielded by the inclusion of its own past over and above the predictability already achieved from the past of X and Z [163]:

$$G_{Y|XZ} = \ln(\sigma(y'|\mathbf{x}^-, \mathbf{z}^-)) - \ln(\sigma(y'|y^-, \mathbf{x}^-, \mathbf{z}^-)). \quad (4.12)$$

In the same manner as the decomposition presented in (4.7), $C_{XZ \rightarrow Y}$ can be decomposed as:

$$C_{XZ \rightarrow Y} = C_{X \rightarrow Y} + C_{Z \rightarrow Y|X} = C_{Z \rightarrow Y} + C_{X \rightarrow Y|Z}, \quad (4.13)$$

where $C_{X \rightarrow Y}$ and $C_{Z \rightarrow Y}$ stand for the *cross predictability* of Y from X or Z , respectively, and terms $C_{Z \rightarrow Y|X}$ and $C_{X \rightarrow Y|Z}$ stand for the *conditional cross predictability* of Y from Z and X conditioned to X and Z , respectively.

4.2.4 Measurement Framework

In order to apply the definitions formulated in section 4.2.3, let assume that the neighbour electrodes convey the largest amount of the information relevant to the activity sensed by the target electrode under analysis. Accordingly, a joint three-electrode analysis scheme is proposed based on defining the following three processes:

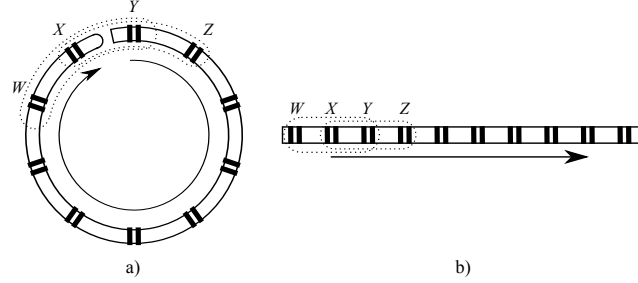


Figure 4.4: Schematic of application of the proposed three-electrode analysis scheme: a) over a circular catheter and b) over a linear catheter. Arrows indicate the movement of the electrode triplet for analysis.

1. Process Y : Target electrode EGM signal under study.
2. Process X : Leftward neighbour electrode EGM signal.
3. Process Z : Rightward neighbour electrode EGM signal.

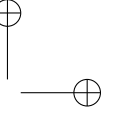
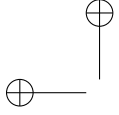
This three-electrode analysis scheme is shifted across the catheter electrode distribution under analysis until its complete coverage is achieved, as illustrated in Fig. 4.4.

All the measures introduced in section 4.2.3 are related with the predictability of the signal under study (process Y) mediated by the influence of the past of the neighbour electrodes (processes X and Z) and/or its own past. The aim is to use these interactions to assess cardiac activity; therefore, the following interpretations for some of the derived measures are provided:

- The predictability P_Y can be interpreted as a general measure of the regularity of the target EGM signal Y that takes into account the possible influences from the neighbour EGM signals X and Z .
- The self-predictability S_Y and the Granger autonomy $G_{Y|XZ}$ can be interpreted as measures of the local regularity of the target EGM signal Y , which arises from the knowledge of its own dynamics, discounting or not the possible effect of the neighbour EGM signals X and Z .
- The conditional Granger causalities $G_{Z \rightarrow Y|X}$ and $G_{X \rightarrow Y|Z}$ assess the information transfer from the adjacent EGM signals X or Z to the target electrode EGM signal Y , after removing the effect of the other adjacent site.

Moreover, the *neighbour connectivity ratio* N_Y can be defined as the relative amount of information carried by the target signal that can be predicted solely from the past of the neighbour processes. This concept is quantified combining autonomy and predictability as follows:

$$N_Y = 1 - \frac{G_{Y|XZ}}{P_Y}, \quad (4.14)$$



so that (4.14) spans from 0 to 1, where lower values show high contribution of the autonomy in predictability, and vice versa. Note that the neighbour connectivity ratio can be formulated equivalently as $N_Y = C_{XZ \rightarrow Y} / P_Y$, which reveals that N_Y reflects how much site Y is connected with sites X and Z , with low values indicating isolation of the target electrode since its activity is predicted mainly by its own dynamics (i.e., autonomy) but not from the dynamics of the adjacent electrodes.

After computing the complete set of GC measures across the catheter electrode distribution, the *propagation direction* can be defined as:

$$D_{X \leftrightarrow Y} = \frac{G_{Y \rightarrow X|W} - G_{X \rightarrow Y|Z}}{G_{Y \rightarrow X|W} + G_{X \rightarrow Y|Z}}, \quad (4.15)$$

where the process W stands for the adjacent electrode to X in the opposite (leftwards) direction, if it is available (see Fig. 4.4). The propagation direction $D_{X \leftrightarrow Y}$ quantifies the dominant direction of the information transfer, i.e., the relative strength of the information transferred in one direction with respect to the information transferred in the opposite direction. This measure spans from -1 to 1 , where negative values indicate a dominant information transfer from X to Y and vice versa. Thus, $D_{X \leftrightarrow Y}$ can be used to track the propagation of the electrical activity throughout the catheter electrode distribution.

4.3 Predictability Analysis of Atrial Fibrillation

4.3.1 Testing Databases

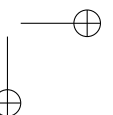
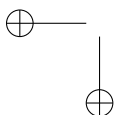
Computer Simulations

The Courtemanche-Ramírez-Nattel ionic model [164] was used as base for generation of the simulation data. This ionic model runs over a simplified human atrial geometry represented as a monolayer sphere with 6 cm diameter, discretised into a triangular mesh of approximately 125000 nodes and a spatial resolution of about 300 μm .

The current source approximation [165] was used to obtain b-EGMs at virtual spherical electrodes of 0.25 mm diameter located at 0.5 mm distance of the simulated anatomy. These electrodes were distributed over the simulated anatomy mimicking a basket catheter with eighteen regularly spaced splines ($\pi/9$ rad angular distance), each one composed by eight regularly spaced bipoles with 2 mm inter-electrode distance, as illustrated in Fig. 4.5(a). Synthetic b-EGM signal length is 10 s with a sampling frequency of 1 kHz.

Different activity pattern scenarios were simulated in this setting in order to cover the most common propagation patterns:

1. Single activation source: Activation comes from a single source located at the sphere pole, firing at a period of 350 ms with random jitters of 6 ms (see Fig. 4.5(b)).



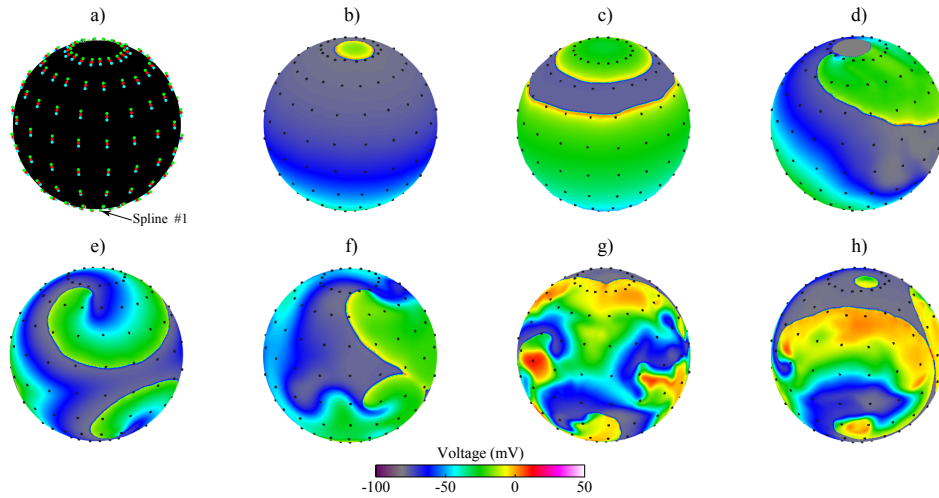


Figure 4.5: Simulation set-up: a) bipolar electrode distribution over the simulated anatomy mimicking a basket catheter. Green and blue dots indicate the measurement electrodes of each bipole, and red dots stand for the geometrical center of the bipole. Arrow point the spline #1 with counterclockwise spline numbering. Panels (b)–(h) show snapshots of the different simulated patterns (coloured using the membrane voltage; black dots indicate the location of the bipoles centres): b) single activation source, c) double activation source, d) anatomical reentry, e) stable functional reentry, f) unstable functional reentry, g) AF and h) AF with focal source.

2. Double activation source: Activation comes from two sources located at the two poles of the sphere. The two sources fire with a different initial phase and present different firing periods. The source at the top fires for the first time at 135 ms, and it subsequently activates with a period of 350 ms with random jitters of 6 ms, while the source at the bottom initially fires at 0 ms, with a period of 360 ms with random jitters of 6 ms (see Fig. 4.5(c)).
3. Anatomical reentry: Reentry anchored to an anatomical obstacle with revolution period of ~ 360 ms located at the top of the sphere combined with a functional reentry pattern (spiral) located at the bottom of the sphere (see Fig. 4.5(d)).
4. Stable functional reentry: Two stable functional reentries (spirals) with revolution period of ~ 200 ms located at each pole of the sphere (see Fig. 4.5(e)).
5. Unstable functional reentry: Unstable meandering spirals with irregular behaviour (see Fig. 4.5(f)).
6. AF: Complex fibrillation pattern with spiral breakups and multiple wavelets (see Fig. 4.5(g)).
7. AF with focal source: Combination of a complex fibrillation pattern with a localized source firing at 275 ms, located at a pole of the sphere, which entrains the surrounding tissue (see Fig. 4.5(h)).

Ionic and diffusion model parameters were modulated to reproduce the different simulation scenarios. Specifically, remodelled versions of the Courtemanche model were used in scenarios 4-5 [166] and 6-7 [165]. Conduction was assumed to be uniform and isotropic, with the diffusion coefficient D ranging between 0.2 and 0.5 cm²/s. ODE-PDE system integration was performed by a fully-adaptive multi-resolution algorithm [167]. Reaction and diffusion were integrated with time step $\Delta t = 0.1$ ms, using the Rush-Larsen non-standard finite difference forward Euler method and explicit node-centred finite difference stencils [168].

Clinical Mapping Data

Mapping data were obtained from a database of selected patients with paroxysmal AF displaying different spatiotemporal patterns of atrial organization [169]. Recordings were acquired using a Constellation “basket” catheter (*Boston Scientific Inc., Natick, MA, USA*) placed in the RA. The basket catheter consisted of eight splines, each carrying eight equally spaced electrodes with 4 mm inter-electrode distance. Therefore, thirty-two b-EGMs, formed by coupling adjacent pairs of electrodes, were acquired at 1 kHz sampling frequency and filtered between 30-500 Hz (*CardioLab System Prucka Engineering Inc., Houston, TX, USA*).

Recordings had different signal lengths depending on the electrophysiological study. Therefore, for analysis purposes, a 10 s length signal excerpt was selected as the one maximizing the global root mean square (RMS) value of the b-EGM amplitude after band-pass filtering between 40-250 Hz. This criterion aims to select a time window with (overall) good electrode contact with the atrium and to objectivize further analysis.

4.3.2 Application of the Predictability Framework on Basket Catheter Data

The measurement framework introduced in section 4.2.4 was applied on the available basket catheter data considering two different configurations: along the catheter splines (spline-wise analysis), or along the electrodes located at each row of the catheter in circular distribution (row-wise analysis). As the introduced measures are dependent on the considered neighbour electrodes, the analysis generally yields different measures when performed on each of the two configurations.

Then, activity maps illustrating the electrical activity measured by the basket catheter were constructed by combining the neighbour connectivity ratio N_Y and the propagation direction $D_{X \leftrightarrow Y}$. In these maps, each electrode of the basket catheter was represented as a node coloured according to the value of N_Y , and pairs of adjacent electrodes were connected according to the values of $D_{X \leftrightarrow Y}$. While $D_{X \leftrightarrow Y}$ could be computed and displayed for both spline- and row-wise analyses, the visualization of N_Y computed through spline- and row-wise analysis in a single graph is not straightforward. Therefore, for simplicity, N_Y values are displayed in the activity maps following the analysis direction (row-wise or spline-wise) where the map has a greater average predictability (denoted as \bar{P}_Y^s and \bar{P}_Y^r for spline- and row-wise analysis, respectively).

Table 4.1: Regularity measurements of each simulated scenario (median [1st quartile,3rd quartile]) obtained at spline-wise and row-wise analyses.

Scenario	Spline-wise analysis			
	P_Y (a.u.)	$G_{Y XZ}$ (a.u.)	N_Y (a.u.)	S_Y (a.u.)
Single source	6.33 [6.01,6.48]*	0.73 [0.68,0.80]*	0.89 [0.87,0.89]*	2.04 [2.01,2.08]*
Double source	3.73 [2.97,5.69]*	1.54 [0.93,1.97]*	0.59 [0.33,0.85]*	2.07 [2.03,2.10]*
Anatomical reentry	3.34 [2.58,4.48]*	1.60 [1.17,1.85]*	0.50 [0.29,0.72]*	2.24 [2.17,2.32]*
Stable functional reentry	3.97 [3.39,4.70]*	1.13 [0.93,1.31]*	0.72 [0.63,0.79]*	2.33 [2.17,2.43]*
Unstable functional reentry	2.13 [2.01,2.24] [§]	1.79 [1.70,1.86] [§]	0.16 [0.12,0.20] [§]	1.88 [1.82,1.92] [§]
AF	2.19 [2.14,2.24]	2.05 [1.97,2.11] [†]	0.06 [0.03,0.08] [†]	2.12 [2.08,2.16] [†]
AF with focal source	2.21 [2.13,2.27]	1.98 [1.88,2.04]	0.09 [0.06,0.15]	2.10 [2.03,2.14]
Scenario	Row-wise analysis			
	P_Y (a.u.)	$G_{Y XZ}$ (a.u.)	N_Y (a.u.)	S_Y (a.u.)
Single source	4.32 [3.65,4.82]*	0.33 [0.12,0.63]*	0.92 [0.85,0.97]*	2.01 [1.97,2.06]*
Double source	3.36 [2.75,4.31]*	0.37 [0.19,0.68]*	0.89 [0.82,0.95]*	2.04 [2.00,2.09]*
Anatomical reentry	3.32 [2.70,4.53]*	1.19 [0.96,1.59]*	0.64 [0.43,0.79]*	2.19 [2.08,2.28]*
Stable functional reentry	4.33 [3.60,5.02]*	0.99 [0.77,1.22]*	0.76 [0.67,0.84]*	2.22 [2.09,2.33]*
Unstable functional reentry	2.17 [2.09,2.29] [§]	1.55 [1.16,1.69] [§]	0.30 [0.21,0.54] [§]	1.86 [1.80,1.91] [§]
AF	2.26 [2.19,2.34]	2.00 [1.91,2.06] [†]	0.10 [0.07,0.19] [†]	2.12 [2.08,2.17] [†]
AF with focal source	2.27 [2.16,2.54]	1.86 [1.70,2.00]	0.17 [0.10,0.32]	2.09 [2.02,2.15]

* statistically significant difference ($p \leq 0.05$) against the three unstable scenarios (5, 6 and 7).

[§] statistically significant difference ($p \leq 0.05$) against scenarios 6 and 7.

[†] statistically significant difference ($p \leq 0.05$) against scenario 7.

4.3.3 Statistical Analysis

The studied GC-based measures are shown as median and interquartile range. The statistical significance of the differences between GC-based measures obtained from pairs of simulated scenarios is assessed, when indicated, using the Wilcoxon-Mann-Whitney test. Moreover, the statistical significance of any GC-based measure is tested against the null hypothesis of zero GC using the test described in [156]. In all the statistical tests, a p -value ≤ 0.05 was set as threshold for rejecting the null hypothesis.

4.3.4 Results

Predictability Analysis of Simulation Data

Table 4.1 and Fig. 4.6 show the distributions of the measures of predictability P_Y , Granger autonomy $G_{Y|XZ}$, neighbour connectivity ratio N_Y and self-predictability S_Y , computed for the seven simulated scenarios.

The predictability presents the highest values for the single source scenario, and its values decrease as the simulated patterns become more complex (see Fig. 4.6(a)).

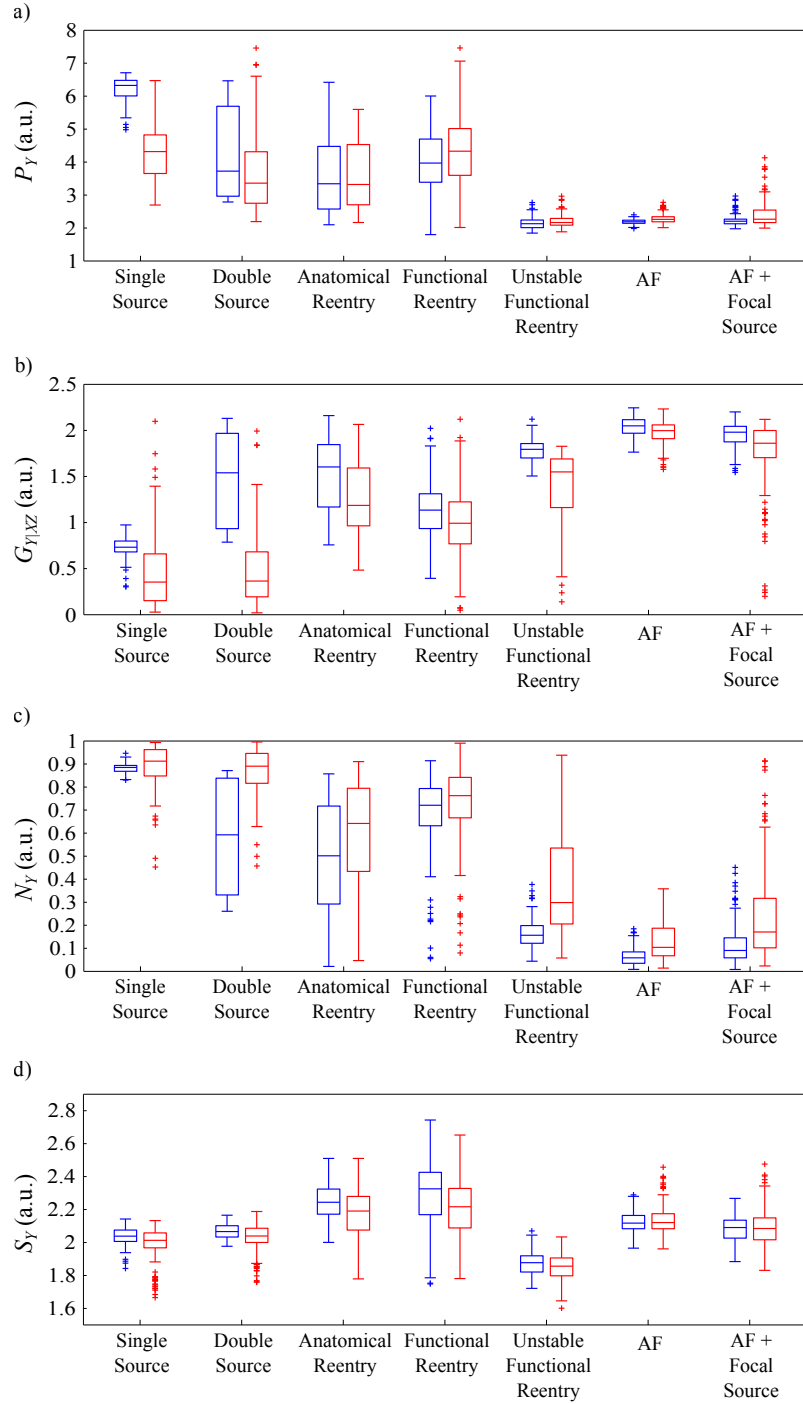


Figure 4.6: Predictability measures obtained by spline-wise (blue boxes) and row-wise (red boxes) analysis of each simulated scenario: a) predictability P_Y , b) Granger autonomy $G_{Y|XZ}$, c) neighbour connectivity ratio N_Y and d) self-predictability S_Y .

On the other hand, the Granger autonomy shows an opposite behaviour (see Fig. 4.6(b)). This suggests that more regular atrial rhythms exhibit high predictability mostly related to the influence of adjacent sites on the target EGM signal. However, such influence vanishes in more complex atrial activity where a significant amount of predictability is due to local activity.

The neighbour connectivity ratio, being related to the ratio of the previous two, measures their relation in normalized units, reflecting the regularity of the patterns resulting from non-isolated atrial activity (Fig. 4.6(c)).

The self-predictability does not seem to characterize well the complexity of the simulated patterns, as it shows similar ranges for the different simulation scenarios with no clear trend with the complexity of the simulated activity (see Fig. 4.6(d)).

As shown in Table. 4.1, all the studied measures are able to distinguish between organized and disorganized simulated activity ($p \leq 0.05$) in both spline-wise and row-wise configuration analysis.

Causality Analysis of Simulation Data

Figure 4.7 exemplifies the capability of the introduced framework to track the propagation of atrial activity through the propagation direction $D_{x \leftrightarrow y}$.

Figure 4.7(a)–(b) illustrate the activity sensed by one of the linear splines of the simulated basket catheter in presence of a single activation source pattern and a double activation source pattern, respectively. In Fig. 4.7(a) activation comes from the top of the spline and propagates downwards, whereas in Fig. 4.7(b) activation comes from both the top and bottom part of the spline and fuses between electrodes 4 and 5 as illustrated in the collision EGM indicated with an asterisk.

Figure 4.7(c)–(d) illustrates the activity sensed by electrode row #1 in presence of an anatomical reentry and a stable functional reentry, respectively. In Fig. 4.7(c), the propagation follows a sequence that indicates a wavefront circulating in the direction of the circular electrode configuration. Figure 4.7(d) shows that electrode 18 is the earliest activated (marked with an asterisk), which suggests the presence of a source of activation at that site. Moreover, the activation linearly propagates across the studied circular configuration, ending at electrode 9.

Activity Mapping of Simulation Data

Figure 4.8 illustrates the activity maps of the full simulated basket catheter.

The activity map for the single source scenario is shown in Fig. 4.8(a). This map was obtained by spline-wise computation of N_Y (as $\bar{P}_Y^s = 6.22$ and $\bar{P}_Y^r = 4.28$). It shows that the wave travels from top to bottom in a very regular fashion indicated by consistently high $D_{x \leftrightarrow y}$ and N_Y values. The activity map for the double source scenario is shown in Fig. 4.8(b). This map was obtained by spline-wise computation of N_Y (as $\bar{P}_Y^s = 4.25$ and $\bar{P}_Y^r = 3.68$). Both the sign of the propagation direction $D_{x \leftrightarrow y}$ and the high values of N_Y indicate that the activation comes from each extreme of the

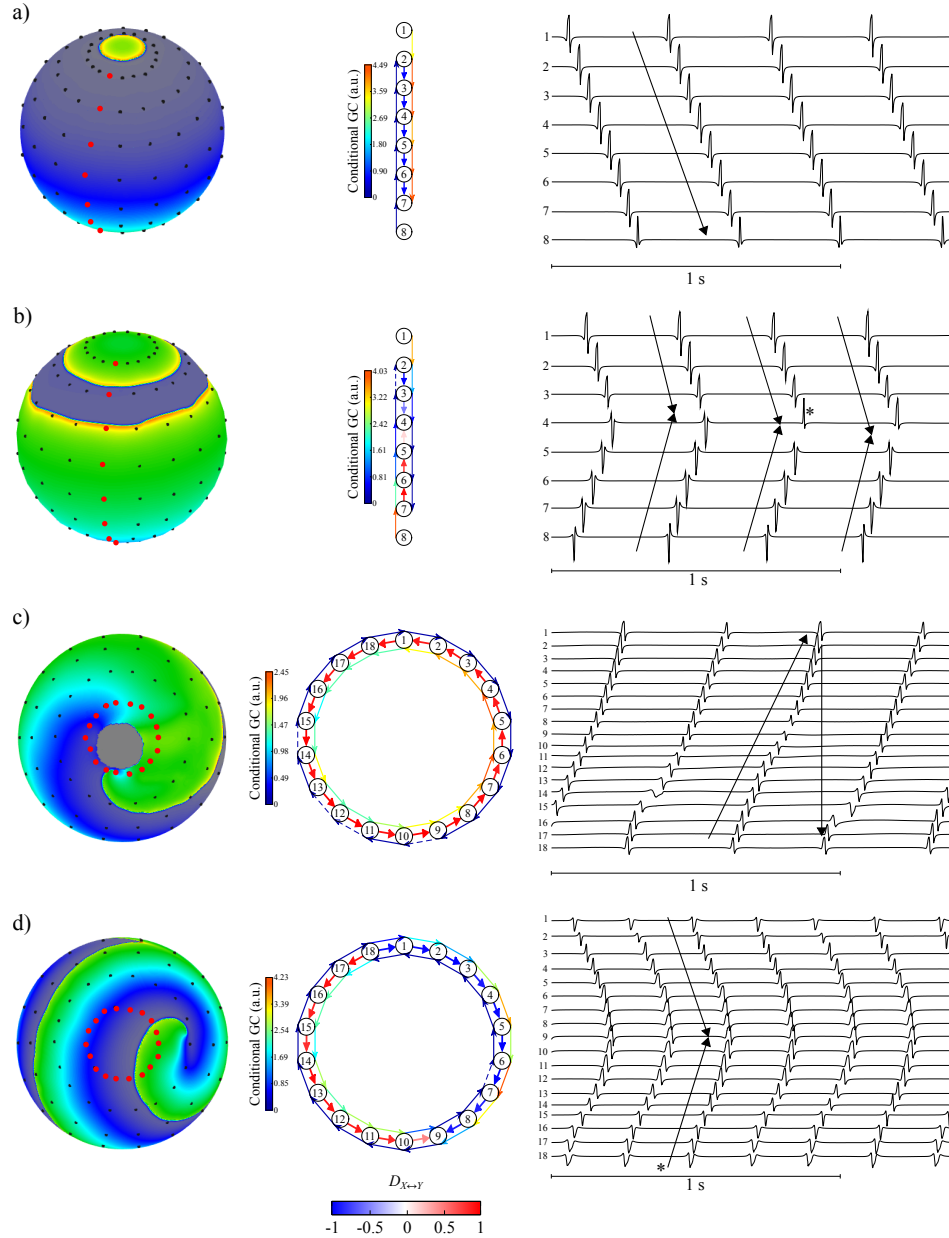


Figure 4.7: Examples of causality analysis maps obtained using the introduced framework during simulation of: a) single source (electrode spline #1), b) double source (electrode spline #1), c) anatomical reentry (electrode row #1) and d) stable functional reentry (electrode row #1). Each panel shows: at the left, a snapshot of the simulated pattern (red dots: electrodes selected for catheter analysis); at the center, a schematic of the catheter used for the causality analysis with electrode connections (numbered circles: corresponding catheter electrodes; lateral coloured arrows: conditional GC, dashed if p -value ≤ 0.05); central tick arrows: propagation direction $D_{X \leftrightarrow Y}$; at the right, the corresponding EGM signals with propagation indicated by black arrows. The meaning of the asterisks in (b) and (d) is explained in text.

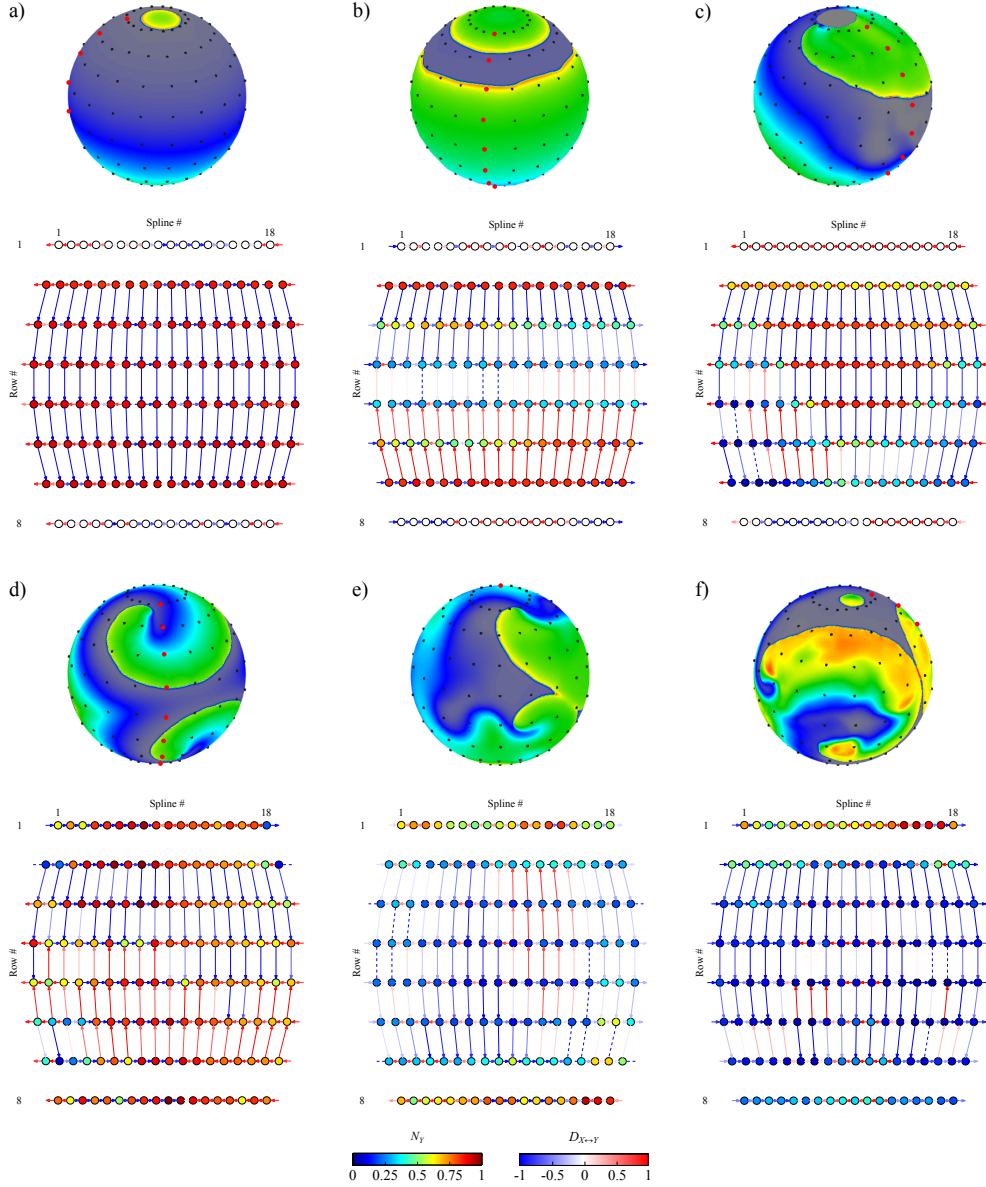


Figure 4.8: Activity maps of the simulated basket catheter for simulations of: a) single source, b) double source, c) anatomical reentry, d) stable functional reentry, e) unstable functional reentry and f) AF with focal source. Each panel shows: at the top, a snapshot of the simulated scenario (red dots indicate the electrode spline #1 with counterclockwise spline numbering) and at the bottom, the corresponding schematic of the simulated basket catheter whose electrodes are represented by nodes coloured corresponding to the values of N_Y (non-colored nodes: N_Y could not be obtained) and connected following the values of the propagation direction $D_{X \leftrightarrow Y}$ (dashed connections: no dominant direction, i.e., $|D_{X \leftrightarrow Y}| \leq 0.05$). N_Y is computed through spline-wise analysis in panels (a)–(c) and through row-wise analysis in panels (d)–(f). Note that due to geometry constraints, connections between rows 1-2 and rows 7-8 could not be obtained.

catheter. Moreover, N_Y values decrease towards the collision area at the center part of the catheter.

Figure 4.8(c) shows the activity map of the anatomical reentry scenario. This map was obtained by spline-wise computation of N_Y (as $\bar{P}_Y^s = 3.63$ and $\bar{P}_Y^r = 3.60$). The different values of N_Y and $D_{x \leftrightarrow y}$ observed between the top and bottom parts of the catheter suggest the presence of a stable and regular pattern located at the top, with revolution direction going from spline 18 to 1 and the presence of a more unstable pattern at the bottom.

Figure 4.8(d) shows the activity map of the functional reentry simulation scenario. This map was obtained by row-wise computation of N_Y (as $\bar{P}_Y^s = 3.98$ and $\bar{P}_Y^r = 4.29$). The low N_Y values suggest two sources of instability, the first located around the top part of splines 1-18 and the second around the bottom part of splines 2-3. These two sources of instability are surrounded by a stable propagation observed throughout the rest of the catheter.

The activity map of the unstable functional reentry simulation scenario is shown in Fig. 4.8(e). This map was obtained by row-wise computation of N_Y (as $\bar{P}_Y^s = 2.14$ and $\bar{P}_Y^r = 2.21$). The homogeneously low values of N_Y suggest a high complexity of the activation throughout the catheter, related to low predictability and/or high autonomy of the atrial activity. However, a reentrant path is suggested around splines 7-13.

The activity map of the AF with focal source scenario is shown in Fig. 4.8(f). This map was obtained by row-wise computation of N_Y (as $\bar{P}_Y^s = 2.24$ and $\bar{P}_Y^r = 2.39$). A predominant up-to-bottom propagation is identified with low N_Y values for almost all electrode locations except for those upper rows where a source of regularity is present. Moreover, high values of N_Y are shown for splines 13-17, suggesting the location of a regularity source slightly towards this direction.

Causality Analysis of Mapping Data

EGMs obtained using a basket catheter were studied from two patients with paroxysmal AF, showing different spatiotemporal organization patterns. In particular, two complete rows of the basket catheter from each patient are shown and analysed.

In Fig. 4.9(a) the framework tracks the complete activity, suggesting an early propagation from the posterior RA wall (electrode CD1 indicated by an asterisk) at the cranial row that shifts towards the RA septum (electrodes EF3-6 indicated by an asterisk) at the medial row. In Fig. 4.9(b), the framework identifies some electrode connections (CD5 to GH1 for the cranial row and AB7 to GH2 in the caudal row) even in the presence of a complex propagation pattern with multiple wavefront blocks.

The values of N_Y obtained for the two circular electrode configurations of Fig. 4.9(a) (presented as mean \pm SD over all electrodes) indicate a degree of regularity higher than that observed for the circular configurations of Fig. 4.9(b). These higher values are in agreement with the clear propagation observed in Fig. 4.9(a) looking at the causality analysis maps.

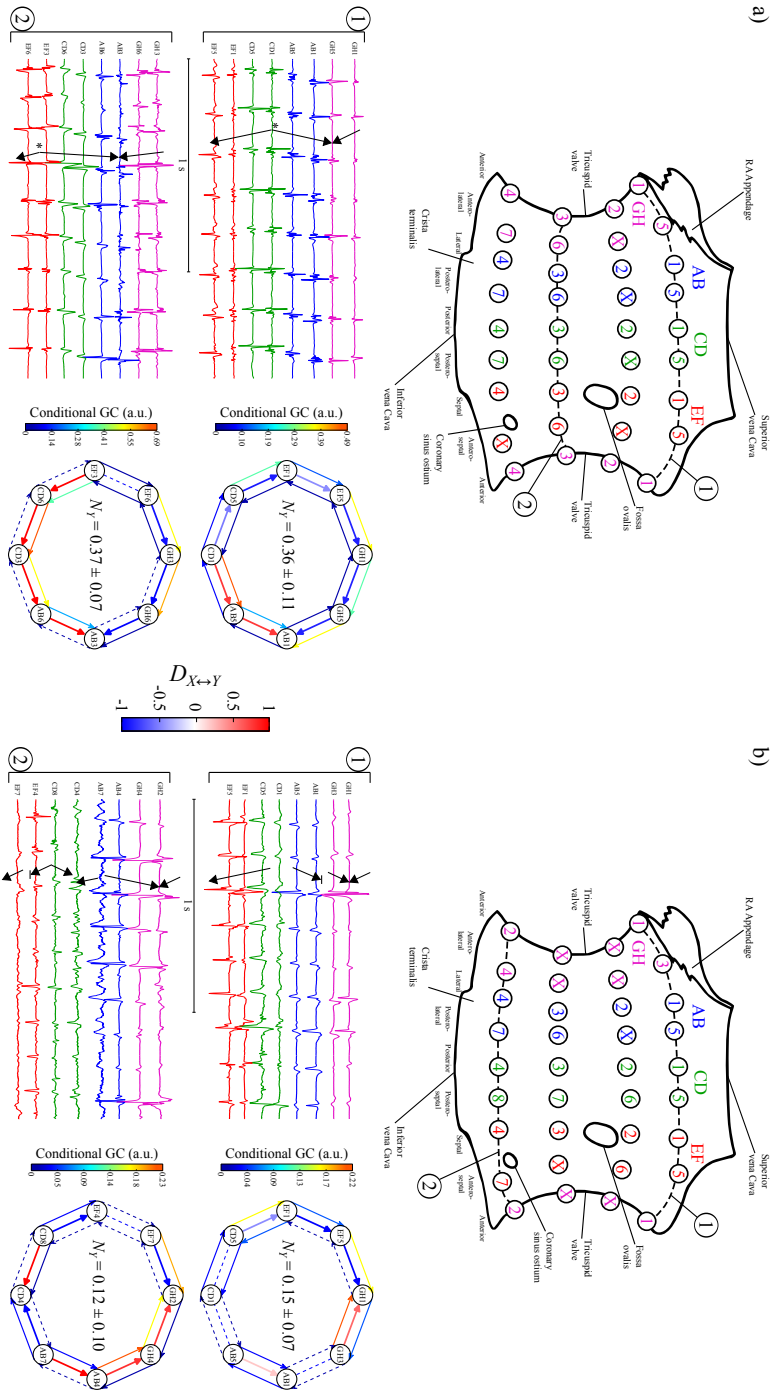


Figure 4.9: Application of the proposed framework to RA basket mapping data in two patients with spatiotemporal AF patterns exhibiting different levels of complexity. Each panel shows: at the top, a schematic representation of the open RA with the position of the recording electrodes (unavailable electrodes due to miss-contact are indicated with X; electrode connected with a dashed line indicate the analysed configuration); at the bottom left, the corresponding b-EGM signals of the analysed circular configurations (numbered 1 and 2); at the bottom right, the corresponding causality map (named circles: corresponding catheter electrodes; lateral coloured arrows: conditional Granger causality, dashed if p -value ≤ 0.05 ; central tick arrows: propagation direction $D_{X↔Y}$, dashed if no dominant direction is present, i.e., $|D_{X↔Y}| \leq 0.05$) including at the centre the average \pm SD value of N_y . The meaning of the asterisks in (a) is explained in text.

4.4 Discussion

In this chapter, a framework based on the concept of GC is introduced in order to quantify the predictability of intracardiac signals and to assess both the regularity of the activity of individual cardiac sites and the interactions among spatially separated sites. The GC is a measure of prediction and precedence, which is assessed within the context of a linear analysis framework. Accordingly, MVAR models of the pre-processed b-EGMs were used for computing the GC-related measures based on the residuals variance of different process regressions [156, 159].

In this context, GC analysis is formalized for atrial signals in a unified framework by providing a set of prediction measures, which are used and interpreted within the physiology of AF. Note that not all GC-based measurements presented in section 4.2.3 are relevant for this objective (e.g. the conditioned decompositions of the joint cross-predictability), but they have been defined to achieve completeness in the presentation of the predictability framework.

With the aim of providing a detailed view of the potential usefulness of the methodology, the evaluation of the proposed framework was conducted using both simulations of different AF mechanisms and clinical mapping data. The simulation study employed seven different simulation scenarios, covering a wide range of conditions of atrial patterns from regular to irregular activity. Moreover, the derived EGM signals were obtained mimicking a basket catheter configuration, which provides a realistic situation found in an electrophysiology lab. This basket catheter configuration allowed also to test the framework employing different electrode distributions (i.e., circular and linear) and to prove the generality of the proposed three-electrode analysis scheme.

4.4.1 Quantification of the Regularity of Simulated Atrial Activity

The predictability and its conditioned decompositions, the self-predictability and the Granger autonomy, allow to measure different aspects of the regularity of the signal and the underlying activity. Predictability and Granger autonomy show an opposite behaviour with respect to the complexity of the simulated activity. On the other hand, the self-predictability does not show a clear trend that differentiates regular from irregular rhythms, in contrast with Granger autonomy, as shown in Table 4.1 and Fig. 4.6. This raises the importance of spatiotemporal analysis because the self-predictability was mainly affected by the surrounding signals in organized or regular rhythms and this effect was removed by definition in the computation of the Granger autonomy measure.

The neighbour connectivity ratio combines predictability and Granger autonomy, providing a normalized descriptive measure of the atrial rhythms that accounts for both the global regularity and the degree of connectivity. The low values of the neighbour connectivity ratio found for the unstable simulated scenarios (unstable functional reentry, AF and AF with focal source), compared to the organized scenarios (p -value

≤ 0.05 for all comparisons) reflect the ability of this index to quantify isolation. Hence, the more irregular the propagation is, the less predictable the signal is from the adjacent electrodes, and lower values are attained for the neighbour connectivity ratio.

All these measures are dependent on the direction of the propagation with respect to the orientation of the three-electrode analysis scheme used for rhythm analysis and characterization (see Fig. 4.6). Important differences appear in scenarios where the propagation direction follows the direction of one of the two electrode distributions (i.e., spline-wise or row-wise). In particular, in scenarios with one/two sources at the “poles” present high/low values during row-wise analysis. In these cases, the activation wavefront passes simultaneously through all electrodes, allowing the adjacent electrodes to explain the activity of the target electrode. On the other hand, spline-wise analysis of anatomical reentry and functional reentry show lower regularity, compared to row-wise analysis, due to the differential behaviours of each hemisphere.

4.4.2 Activity Tracking Capability

The analysis of the conditional Granger causality by means of the propagation direction $D_{X \leftrightarrow Y}$ illustrates the sequence of activation sensed by the catheter. The sign and the values of $D_{X \leftrightarrow Y}$ quantify the predominant direction and the relative strength of information transfer between two electrodes and track the propagation through the catheter, as is illustrated in the examples from simulations shown in Figs. 4.7 and 4.8. Moreover, Fig. 4.9 shows examples of the application of the proposed methodology, when atrial activity was mapped using the propagation direction in paroxysmal AF patients showing different organization patterns. The good tracking capability observed in these illustrative cases, suggests the usefulness of the proposed measure of propagation direction.

Methodologically, the propagation direction is defined using the conditional Granger causality $G_{X \rightarrow Y|Z}$ and $G_{Y \rightarrow X|W}$ in order to discount the interaction between electrodes X and Y from its other neighbours (W and Z , respectively). In the case of $L = 3$, $D_{X \leftrightarrow Y}$ could have been equivalently defined in terms of the Granger causalities between X and Y (i.e. $G_{X \rightarrow Y}$ and $G_{Y \rightarrow X}$). However, the latter definition would be limited within an extended framework with $L > 3$, where additional conditioning terms would be needed to avoid over-estimation of the existing interactions between close neighbour electrodes with the target electrode.

Moreover, combining the propagation direction $D_{X \leftrightarrow Y}$ and the neighbour connectivity ratio N_Y , it is possible to obtain comprehensive activity maps that include, within the same picture, information about the direction of propagation and the areas of stability of such propagation, as illustrated in Fig. 4.8. These activity maps allow to observe the underlying cardiac activity in detail. For instance, Fig. 4.8(a) shows a stable map (high N_Y values) reflecting the presence of a single source of activation, while Fig. 4.8(b) shows decreasing values of N_Y while approaching the central area of the sphere, where the wavefronts from the two sources collide. This last result reflects the instability of the collision, and explains the wide range of regularity observed in Fig. 4.6.

Figure 4.8(c) shows different behaviour between hemispheres, with an organized propagation at the top of the sphere due to the anatomical reentry and less organized propagation at the bottom due to the collision of the “tail” and the “head” of the reentrant wavefront. Figure 4.8(d) shows medium-to-high regularity in the whole catheter except for those locations where the tips of the functional reentries (spirals) are localized. Figure 4.8(e) shows a preferential reentry path from top-to-bottom around splines 6-9 and from bottom-to-top around splines 9-13, whereas unstable patterns occur in the rest of the simulated sphere. Finally, Fig. 4.8(f) shows that the top of the sphere, where the focal source of activation entrains the tissue during AF, is the most regular part of the simulation scenario.

While the activity maps have been chosen to be obtained following the analysis direction that maximizes the average predictability value, both spline- and row-wise analysis are needed for their construction using the proposed three-electrode analysis scheme. Therefore, although this maximization criterion can be considered as a guideline for default visualization in case the framework was applied to clinical practice, it is flexible enough to allow displaying the results of both analyses.

4.4.3 Comparison with Other Methods

The framework introduced in this chapter extends several methodologies already proposed in this context. For instance, frequency domain causality analysis of AF was performed in [148, 149] via partial directed coherence (PDC). Compared to PDC, the introduced framework provides causality indices that are easier to interpret, as the method does not require identifying a frequency band to analyse interactions. Moreover, the introduced approach explores a wide range of dynamical properties of the atrial signals besides causality, such as overall predictability, self-predictability, the proposed neighbourhood connectivity ratio and the propagation direction considering not only pairs of electrodes, but also their adjacent electrodes.

On the other hand, the approaches in [150–153] also proposed time-domain GC-based measures, but are limited in that they define bi-variate measures, which are sensitive to spurious connectivity induced by a common driver or cascade effects of other neighbour signals. The introduced framework implements a multivariate formulation of GC measures that allows a more precise identification of propagation patterns. It may be extended to take any number of neighbouring atrial sites into account, just by considering Z as a multi-variate process that includes all the $L - 2$ remaining neighbour electrodes under analysis.

In addition to the multi-variate formulation, the proposed framework extends measures of spatial organization such as cross-correlation or cross-spectral measures (proposed, e.g., in [132, 136, 137]) also by providing the information about the direction of the interactions, which is closely related to the atrial wavefront propagation. Also, compared with activation sequence-based approaches (e.g. in [77, 81, 82, 119, 128, 129, 131, 136, 138]), where the main advantage of the proposed framework is that the activation detection step is not necessary and, therefore, the analysis outcomes are not limited by the activation detection accuracy during complex activity.

4.4.4 Limitations

The proposed framework characterizes atrial activity by implementing a linear MVAR modelling analysis of the dynamics and interactions between nearby cardiac sites. While the presence of nonlinear dynamics may limit the descriptive capability of the framework, the linear assumption appears to be sufficient to track most of the activity in both simulations and clinical mapping data. Nevertheless, it may be interesting to consider extensions of our approach to nonlinear models, although not many examples can be found in the analysis of AF intracardiac signals [170].

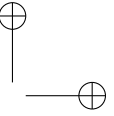
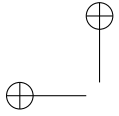
The proposed three-electrode analysis scheme assumes one-electrode neighbourhood and one-dimensional interaction. This topology is applicable to any multi-electrode catheter, but this assumption may not always be accomplished due to electrode sparsity. Other limitations of the proposed scheme are related to the number of available electrodes, especially for extremal electrodes in linear catheter configurations, and the need of achieving complete contact for all electrodes in order to perform a continuous analysis of the cardiac activity. This was especially noticed in real data analysis, which was limited by the lack of contact for some electrodes (see Fig. 4.9). Nevertheless, the proposed three-electrode analysis scheme aims to be general and applicable on any multi-electrode catheter without being tailored to a particular catheter type or electrode distribution. Moreover, linear and circular catheters are still the most commonly used in clinical practice. Some of the limitations described above may be alleviated by choosing other neighbourhood electrode topologies, as allowed by the flexibility of the framework.

4.4.5 Clinical Relevance

The proposed activity maps provide a global visualization of a multi-electrode catheter that may be potentially useful for identifying fibrillation sources and guiding catheter ablation interventions. For that purpose, further evaluation is needed in additional clinical scenarios of AF.

4.5 Conclusion

This chapter presents a linear predictability framework for analysing cardiac activity and interactions during AF based on GC definitions. The method provides regularity measures able to distinguish the complexity between different atrial rhythms. Moreover, it can be applied to track and map the underlying cardiac activity in any simultaneous multi-electrode catheter, not requiring activation detection or post-processing algorithms. The proposed global mapping of regularity and connectivity of the activity acquired from multi-electrode catheters, simultaneously showing signal propagation and stability, can be useful for interpreting such activity and supporting clinicians during ablation interventions.



“Wherever you go, go with all your heart.”

Confucius

Chapter 5

Final Discussion and Conclusion

5.1 Summary and Discussion

5.1.1 Electroanatomical Activation Mapping of Focal Ventricular Arrhythmias

5.1.2 Spatiotemporal High-Density Activation Mapping during Atrial Fibrillation

5.1.3 Analysis of Causal Interactions during Atrial Fibrillation

5.2 Main Limitations

5.3 Conclusion

5.4 Clinical Implications

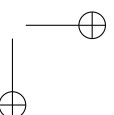
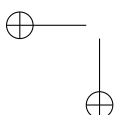
5.5 Future Work

5.1 Summary and Discussion

This thesis proposes intracardiac electrogram (EGM) signal processing approaches to help in the decision process of physicians and companion technicians during ablation interventions and electrophysiological testing of cardiac arrhythmias.

5.1.1 Electroanatomical Activation Mapping of Focal Ventricular Arrhythmias

Electroanatomical mapping (EAM) systems are useful tools for mapping cardiac arrhythmias since they help to visualize their complexity, overcoming classical fluoroscopy catheter ablation procedures. However, these systems do not include nowadays appropriate software for robust detection of local activation times (LATs) for activation mapping (AM), therefore requiring the system operator to manually check each mapping point during the procedure. Chapter 2 introduces a wavelet-envelope-based bipolar electrogram (b-EGM) detector and delineator for automatic ventricular AM



using an EAM system, aiming to provide fast, observer-independent and reproducible LAT detection.

The proposed algorithm uses the surface electrocardiogram (ECG) as a searching window for identifying the onset of the b-EGM signal by means of the wavelet decomposition of the b-EGM signal envelope. The algorithm also exploits the spatial information of close mapping points with morphologically similar b-EGM signal in order to improve map quality.

Validation has been conducted by means of two different studies. First, a detection performance evaluation using a controlled database of patients with focal ventricular tachycardias (VTs). In this database, off-procedure manual annotations from two different experts have been used for validation of the automatic annotations as well as the manual annotations performed during the intervention (on-procedure annotations), which were used to guide ablation decision. In this context, automatic AM shows slightly lower performance than manual on-procedure LAT identification compared with the off-procedure annotation reference. However, automatic LAT annotation correlation and error with respect to the reference annotations were appropriate for identifying the area of interest (AOI) for ablation purposes. This fact and the low computational times of the algorithm can potentially overcome manual LAT identification. This is of especial importance when using high-density multi-electrode catheters where manual identification of LATs over tenths of simultaneously acquired EGM signals becomes unaffordable without automatic or semi-automatic signal processing approaches.

The second study illustrates a clinical evaluation of the automatic activation mapping algorithm. The evaluation consists of quantifying the automatic activation map quality in dealing with two objectives: 1) to correctly identify the early activation site (EAS) isochronal area which becomes in the AOI for ablation purposes and 2) to determine the site of origin (SOO) of the clinical arrhythmia through the measurement of map descriptors based on the size and shape of the 10 ms EAS isochronal area. For this purpose, the used database consists of patients with idiopathic outflow tract ventricular arrhythmias (OTVAs) and septal activation in the right ventricle electro-anatomical map which yields in a SOO uncertainty due to complex 3-D anatomical relationships between the right and the left ventricle outflow tracts. For comparison, manual activation maps created during the intervention were used as reference. The results show that automatic activation maps have similar accuracy in identifying the EAS isochronal area for ablation and a slightly superior SOO identification performance than the manual activation maps, in the studied patient sample.

These two studies provide insights about the performance of the proposed wavelet-envelope-based detector and delineator algorithm. Their results indicate that the algorithm may be useful to reduce map acquisition times (especially when using multi-electrode catheters) as well as to reduce the duration of ablation interventions, minimize uncertainties due to system operator variability and increase ablation outcomes if included within current EAM system software.

5.1.2 Spatiotemporal High-Density Activation Mapping during Atrial Fibrillation

Atrial fibrillation (AF) is a complex arrhythmia in which sequential mapping using EAM systems have limited utility during ablation procedures and therefore, continuous multi-electrode mapping is desirable. However, multi-electrode catheters lack spatial resolution due to electrode sparsity. Thus, high-density multi-electrode array (MEA) sensors are more suitable to provide insights on the mechanisms underlying the fibrillation process. Automatic classic LAT detection in unipolar electrogram (u-EGM) signals simplifies the detection process to just a sequence of time occurrences, rejecting the remaining spatiotemporal information contained in the signal shape and its relation with the surrounding electrodes. Chapter 3 introduces an integrated solution for spatiotemporal high-density AM of the atrium that exploits the relations between close electrodes.

The proposed approach assumes that the complete activation under the MEA can be obtained by combining contributions of simple (isotropic) propagation pattern models whose parameters are iteratively adapted to small areas of the total acquired cardiac activity.

Evaluation was conducted on experimental data obtained from the right atrium (RA) of a single patient during sinus rhythm (SR) and AF. Audited automatic LAT annotations were performed by an expert electrophysiologist and used as “*gold standard*”. In this setting, activation patterns were analysed using a complexity scale showing low LAT error and high agreement of LAT detections compared with the reference, up to the two more complex levels of the scale (where line of blocks (LBs) and complex atrial fibrillation (CAF) are present). Additionally, the isotropic propagation model used for detection allows to represent the estimated focus location for each section of the activation map (i.e., *loci maps*). These *loci maps* provide additional information about the direction, number of concomitant wavefronts circulating behind the MEA sensor and the substrate properties.

The proposed spatiotemporal approach provides accurate, smooth and comprehensive high-density activation maps which also include extra information about the existing wavefront underpassing the MEA sensor. Therefore, this spatiotemporal algorithm can help in the development of systems based on minimally invasive MEA catheters that will increase mapping density during AF ablation interventions or electrophysiological studies

5.1.3 Analysis of Causal Interactions during Atrial Fibrillation

Multi-electrode catheters are used to guide ablation interventions during AF. Therefore, multiple EGM-based quantitative methods have been proposed to aid in the interpretation of the increasing amount of signals acquired during the mapping procedure. However, most of these approaches depend on the outcomes of an activation detection algorithm or/and do not take into consideration the spatiotemporal relation between electrodes. Chapter 4 introduces a linear predictability framework based on

the concept of the Granger causality (GC) for the analysis of the interactions between EGM signals during AF.

The introduced framework considers each EGM signal acquired with a multi-electrode catheter as an stochastic process whose information transfer is driven by the fibrillation activity. Hence, the framework analyses a complete multi-electrode catheter using a three-electrode analysis scheme where the interactions between EGM signals (in the sense of the GC) were quantified using a multi-variate auto-regressive (MVAR) representation of the preprocessed b-EGM signal.

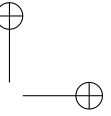
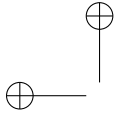
Evaluation and validation of the framework has been conducted by means of a extensive AF simulation database, with 7 different propagation scenarios covering the most common situations found in an electrophysiology lab. Additionally, the framework capabilities were illustrated in examples of patients with paroxysmal AF and different spatiotemporal fibrillation patterns. The framework provides predictability measures that are able to distinguish the regularity of each simulated pattern and track the propagation within the catheter scope using the information transfer between electrode sites. Both concepts can be used together to construct activity maps providing global view of the fibrillation process. Moreover, in real data, the framework is able to track propagation and provide useful information about the fibrillation process.

The introduced predictability framework provides a tool for assessing cardiac activity and interactions during AF using multi-electrode catheters. It provides measures about the regularity and propagation throughout the catheter that is able to distinguish the complexity of the fibrillation activity, flexible enough to be applicable to any multi-electrode catheter electrode configuration and without the need of activation detection or post/processing steps. Moreover, it allows to obtain a global view of the fibrillation activity under the catheter sight, which can be potentially useful in the guidance of AF catheter ablation interventions.

5.2 Main Limitations

The complexity of the diseased cardiac substrate that promotes a certain arrhythmia and the subject variability in heart anatomy may yield to different manoeuvres for electrophysiological testing or catheter ablation procedures. In addition, many different mapping and ablation catheters are used during these procedures depending on the mechanisms and type of the arrhythmia. Therefore, the lack of standard databases with systematic EGM signal acquisition difficult validation efforts and represents one of the main limitations of the introduced approaches in this thesis.

This thesis is focussed on providing EGM-based quantitative solutions for the treatment of different cardiac arrhythmias. On the one hand, the used databases for validation are limited in the number of patients, either due to data singularity, homogeneous patient sample availability or lack of consensus on the measurements. Therefore, further evaluation in different datasets is needed in order to remove the possible bias of the evaluation process of the introduced approaches in this thesis.



Finally, the increasing popularity of EAM systems boosts the usage of radiographic anatomy data and their integration with the electrical information of the cardiac substrate, as mentioned in section 1.5.4. Therefore, radiographic anatomy can provide complementary information which was not exploited during the research presented in this thesis.

5.3 Conclusion

This thesis explores signal intracardiac processing techniques in order to solve common technical and clinical issues in the field of cardiac electrophysiology and arrhythmias. Each particular problem presented in this thesis has been oriented within a spatiotemporal approach, hence providing solutions that take into consideration both the specific problem and the complexity of cardiac arrhythmias.

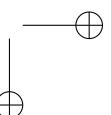
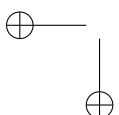
5.4 Clinical Implications

The quantitative EGM-based methods introduced in this thesis are oriented to solve a practical technical problem in the field of cardiac electrophysiology, providing global tools for mapping or characterising a specific arrhythmia. Therefore, they may potentially have a direct impact in daily practice of electrophysiologists and companion technicians.

Especially, the method for automatic AM using EAM systems introduced in chapter 2, represents the more practical-oriented method, as it is designed to solve a common problem in daily clinical routine during cardiac mapping using EAM systems. The introduction of the proposed method into EAM system software would yield into a reduction of map acquisition time, especially of high-density maps using multi-electrode catheters, thanks to the low computational times. Also it may contribute to reduce observer variability and workload during ablation interventions which may yield into safer and faster ablation procedures.

The spatiotemporal method for high-density AM during AF, introduced in chapter 3, represents a novel approach to resolve cardiac activation, developed and tested using MEA sensors in an invasive clinical scenario. The recent developments in omnipolar mapping [171, 172] can take profit of the introduced algorithm and thus be already available for the clinical practice and provide insights in the activation complexity of diverse arrhythmias.

Finally, the analysis of causal interactions between different electrodes placed in the atrium (or in any other part of the heart) introduced in chapter 4, aims to analyse and map cardiac activity using the most common electrode arrangements found in multi-electrode catheters. Within the proposed GC-based predictability framework, the introduced activity maps allow to have comprehensive information of the activation sequence and substrate stability, which may help in the guidance of the ablation approach.



5.5 Future Work

Some of the possible straightforward future research lines derived from the developments presented in this thesis are:

1. To extend the automatic delineation of b-EGM signals using EAM systems in order to identify other waves and features of the signal.
2. To investigate new measurements focussed within the delineated b-EGM signal characteristics in order to emphasize properties of the proarrhythmic cardiac substrate.
3. To complement the quantitative EGM-based methods applicable to EAM systems with the radiographic anatomy information, developing specific signal processing methods focussing on certain special structures in order to increase the sensitivity of the automatic mapping strategy in these critical areas, yielding more proactive mapping strategies.
4. To design a new framework for the application of high-density spatiotemporal detection to the newly developed omnipolar mapping catheters during minimally invasive procedures using EAM systems. Therefore testing the feasibility of the method to provide high-density activation maps into a clinical set-up
5. To extend the causal analysis framework to high-density mapping catheters and omnipolar mapping catheters, in order to complement EAM system mapping strategies providing extra information of the propagation and stability of cardiac activity for arrhythmia assessment.



Bibliography

- [1] R. Lozano, M. Naghavi, K. Foreman, S. Lim, K. Shibuya et al., “Global and Regional Mortality from 235 Causes of Death for 20 Age Groups in 1990 and 2010: A Systematic Analysis for the Global Burden of Disease Study 2010,” *Lancet*, vol. 380, no. 9859, pp. 2095–2128, 2012.
- [2] D. Mozaffarian, E. J. Benjamin, A. S. Go, D. K. Arnett, M. J. Blaha et al., “Heart Disease and Stroke Statistics - 2016 Update: A Report From the American Heart Association,” *Circulation*, pp. e1–e323, 2016.
- [3] N. Townsend, L. Wilson, P. Bhatnagar, K. Wickramasinghe, M. Rayner et al., “Cardiovascular Disease in Europe: Epidemiological Update 2016,” *European Heart Journal*, pp. 1–14, 2016.
- [4] A. C. Guyton and J. E. Hall, *Textbook of Medical Physiology*. W.B. Saunders, 11 ed., 2006.
- [5] L. Gaztañaga, F. E. Marchlinski, and B. P. Betensky, “Mechanisms of Cardiac Arrhythmias,” *Revista Española de Cardiología (English Edition)*, vol. 65, no. 2, pp. 174–185, 2012.
- [6] Z. F. Issa, J. M. Miller, and D. P. Zipes, *Clinical Arrhythmology and Electrophysiology: A Companion to Braunwald’s Heart Disease*. Saunders, 2 ed., 2012.
- [7] L. Sörnmo and P. Laguna, *Bioelectrical Signal Processing in Cardiac and Neurological Applications*. Elsevier Science, 2005.
- [8] S. A. Jones, *ECG Notes: Interpretation and Management Guide*. F. A. Davis Company, 2 ed., 2010.
- [9] A. Bayes de Luna, *Clinical Electrocardiography: A Textbook*. Wiley, 1998.
- [10] G. S. Wagner, *Marriott’s Practical Electrocardiography*. Lippincott Williams & Wilkins, 2001.
- [11] C. Antzelevitch and B. Alexander, “Overview of Basic Mechanism of Cardiac Arrhythmia,” *Cardiac Electrophysiology Clinics*, vol. 3, no. 1, pp. 23–45, 2011.

- [12] M. E. Mangoni and J. Nargeot, "Genesis and Regulation of The Heart Automaticity," *Physiological Reviews*, vol. 88, no. 3, pp. 919–982, 2008.
- [13] E. G. Lakatta, Y. Yaniv, and V. A. Maltsev, "Cardiac Impulse is Initiated by a Coupled System of Membrane Ion Channels and Ca²⁺ Cycling Proteins," in *Cardiac Electrophysiology: From Cell to Bedside* (D. P. Zipes and J. Jalife, eds.), ch. 25, pp. 243–252, Saunders Elsevier, 6 ed., 2014.
- [14] D. P. Zipes, "Mechanisms of Clinical Arrhythmias," *Journal of Cardiovascular Electrophysiology*, vol. 14, no. 8, pp. 902–912, 2003.
- [15] H. E. ter Keurs and P. A. Boyden, "Calcium and Arrhythmogenesis," *Physiological Reviews*, vol. 87, no. 2, pp. 457–506, 2007.
- [16] A. G. Kléber and Y. Rudy, "Basic mechanisms of cardiac impulse propagation and associated arrhythmias.," *Physiological Reviews*, vol. 84, no. 2, pp. 431–488, 2004.
- [17] A. G. Mayer, *Rhythmical Pulsation in Scyphomedusæ*. Washington, D.C.: Carnegie Institution of Washington, 1906.
- [18] G. R. Mines, "On Circulating Excitations in Heart Muscles and their Possible Relations to Tachycardia and Fibrillation," *Transactions of the Royal Society of Canada*, vol. IV, pp. 43–52, 1914.
- [19] W. E. Garrey, "The Nature of Fibrillary Contraction of the Heart - Its Relation to Tissue Mass and Form," *American Journal of Physiology - Heart and Circulatory Physiology*, vol. 33, pp. 397–414, 1914.
- [20] M. A. Allesie, F. I. M. Bonke, and F. J. Schopman, "Circus Movement in Rabbit Atrial Muscle as a Mechanism of Tachycardia. III. The "Leading Circle" Concept: A New Model of Circus Movement in Cardiac Tissue Without the Involvement of an Anatomical Obstacle," *Circulation Research*, vol. 41, no. 1, pp. 9–18, 1977.
- [21] N. El-Sherif, R. Mehra, W. B. Gough, and R. H. Zeiler, "Reentrant Ventricular Arrhythmias in the Late Myocardial Infarction Period. Interruption of Reentrant Circuits by Cryothermal Techniques," *Circulation*, vol. 68, no. 3, pp. 644–656, 1983.
- [22] J. Jalife, O. Berenfeld, and M. Mansour, "Mother Rotors and Fibrillatory Conduction: A Mechanism of Atrial Fibrillation," *Cardiovascular Research*, vol. 54, pp. 204–216, may 2002.
- [23] P. F. Cranefield, A. L. Wit, and B. F. Hoffman, "Genesis of Cardiac Arrhythmias," *Circulation*, vol. 47, no. 1, pp. 190–204, 1973.
- [24] N. El-Sherif, R. A. Smith, and K. Evans, "Canine Ventricular Arrhythmias in the Late Myocardial Infarction Period. 8. Epicardial Mapping of Reentrant Circuits," *Circulation Research*, vol. 49, pp. 255–265, jul 1981.

- [25] M. Valderrábano, Y. H. Kim, M. Yashima, T. J. Wu, H. S. Karagueuzian et al., “Obstacle-Induced Transition from Ventricular Fibrillation to Tachycardia in Isolated Swine Right Ventricles: Insights Into the Transition Dynamics and Implications for the Critical Mass,” *Journal of the American College of Cardiology*, vol. 36, pp. 2000–2008, nov 2000.
- [26] P. S. Chen, P. D. Wolf, E. G. Dixon, N. D. Danieleley, D. W. Frazier et al., “Mechanism of Ventricular Vulnerability to Single Premature Stimuli in Open-Chest Dogs,” *Circulation Research*, vol. 62, pp. 1191–209, jun 1988.
- [27] N. Wiener and A. Rosenblueth, “The Mathematical Formulation of the Problem of Conduction of Impulses in a Network of Connected Excitable Elements, Specifically in Cardiac Muscle,” *Archivos del Instituto de Cardiología de México*, vol. 16, no. 3, pp. 205–265, 1946.
- [28] S. M. Dillon, M. A. Alessie, P. C. Ursell, and A. L. Wit, “Influences of Anisotropic Tissue Structure on Reentrant Circuits in the Epicardial Border Zone of Subacute Canine Infarcts,” *Circulation Research*, vol. 63, no. 1, pp. 182–206, 1988.
- [29] M. Valderrábano, “Influence of Anisotropic Conduction Properties in the Propagation of the Cardiac Action Potential,” *Progress in Biophysics and Molecular Biology*, vol. 94, no. 1-2, pp. 144–168, 2007.
- [30] J. M. Mangrum and J. P. DiMarco, “The Evaluation and Management of Bradycardia,” *New England Journal of Medicine*, vol. 342, no. 10, pp. 703–709, 2000.
- [31] A. E. Epstein, J. P. DiMarco, K. A. Ellenbogen, N. A. M. Estes, R. A. Freedman et al., “ACC/AHA/HRS 2008 Guidelines for Device-Based Therapy of Cardiac Rhythm Abnormalities,” *Journal of the American College of Cardiology*, vol. 51, no. 21, pp. e1–e62, 2008.
- [32] C. M. Tracy, A. E. Epstein, D. Darbar, J. P. DiMarco, S. B. Dunbar et al., “2012 ACCF/AHA/HRS Focused Update Incorporated Into the ACCF/AHA/HRS 2008 Guidelines for Device-Based Therapy of Cardiac Rhythm Abnormalities,” *Journal of the American College of Cardiology*, vol. 61, no. 3, pp. e6–e75, 2013.
- [33] D. J. Fox, A. Tischenko, A. D. Krahn, A. C. Skanes, L. J. Gula et al., “Supraventricular Tachycardia: Diagnosis and Management,” *Mayo Clinic Proceedings*, vol. 83, no. 12, pp. 1400–1411, 2008.
- [34] N. Saoudi, F. García-Cosío, A. Waldo, S. A. Chen, Y. Iesaka et al., “A Classification of Atrial Flutter and Regular Atrial Tachycardia According to Electrophysiological Mechanisms and Anatomical Bases,” *European Heart Journal*, vol. 22, no. 14, pp. 1162–1182, 2001.
- [35] F. García-Cosío, A. Pastor Fuentes, and A. Núñez Angulo, “Clinical Approach to Atrial Tachycardia and Atrial Flutter From an Understanding of the Mechanisms. Electrophysiology Based on Anatomy,” *Revista Española de Cardiología (English Edition)*, vol. 65, no. 4, pp. 363–375, 2012.

- [36] P. M. Kistler, K. C. Roberts-Thomson, H. M. Haqqani, S. P. Fynn, S. Singarayyar et al., “P-wave Morphology in Focal Atrial Tachycardia: Development of an Algorithm to Predict the Anatomic Site of Origin,” *Journal of the American College of Cardiology*, vol. 48, no. 5, pp. 1010–1017, 2006.
- [37] F. García-Cosío, F. Arribas, M. López-Gil, and J. Palacios, “Atrial Flutter Mapping and Ablation. I. Studying Atrial Flutter Mechanisms by Mapping and Entrainment,” *Pacing and Clinical Electrophysiology : PACE*, vol. 19, no. 5, pp. 841–853, 1996.
- [38] C. T. January, L. S. Wann, J. S. Alpert, C. H. Calkins, J. C. Cleveland et al., “2014 AHA/ACC/HRS Guideline for the Management of Patients With Atrial Fibrillation: Executive Summary: A Report of the American College of Cardiology/American Heart Association Task Force on Practice Guidelines and the Heart Rhythm Society,” *Journal of the American College of Cardiology*, vol. 64, no. 21, pp. 2246–2280, 2014.
- [39] G. K. Moe and J. A. Abildskov, “Atrial Fibrillation as a Self-Sustaining Arrhythmia Independent of Focal Discharge,” *American Heart Journal*, vol. 58, no. 1, pp. 59–70, 1959.
- [40] M. A. Allesie, W. J. E. P. Lammers, F. I. M. Bonke, and J. Hollen, “Experimental Evaluation of Moe’s Multiple Wavelet Hypothesis of Atrial Fibrillation,” in *Cardiac Electrophysiology and Arrhythmias* (D. P. Zipes and J. Jalife, eds.), pp. 265–276, Grune & Stratton, 1985.
- [41] K. T. Konings, C. J. Kirchhof, J. L. R. M. Smeets, H. J. Wellens, O. C. Penn et al., “High-Density Mapping of Electrically Induced Atrial Fibrillation in Humans,” *Circulation*, vol. 89, no. 4, pp. 1665–1680, 1994.
- [42] M. Haïssaguerre, P. Jaïs, D. C. Shah, A. Takahashi, M. Hocini et al., “Spontaneous Initiation of Atrial Fibrillation by Ectopic Beats Originating in the Pulmonary Veins,” *The New England Journal of Medicine*, vol. 339, no. 10, pp. 659–666, 1998.
- [43] J. Eckstein, M. Kühne, S. Osswald, and U. Schotten, “Mapping of Atrial Fibrillation - Basic Research and Clinical Applications,” *Swiss medical weekly*, vol. 139, no. 35-36, pp. 496–504, 2009.
- [44] G. Lee, S. Kumar, A. Teh, A. Madry, S. Spence et al., “Epicardial Wave Mapping in Human Long-Lasting Persistent Atrial Fibrillation: Transient Rotational Circuits, Complex Wavefronts, and Disorganized Activity,” *European Heart Journal*, vol. 35, no. 2, pp. 86–97, 2014.
- [45] N. M. S. de Groot, R. P. M. Houben, J. L. R. M. Smeets, E. Boersma, U. Schotten et al., “Electropathological Substrate of Longstanding Persistent Atrial Fibrillation in Patients with Structural Heart Disease: Epicardial Breakthrough,” *Circulation*, vol. 122, no. 17, pp. 1674–1682, 2010.

- [46] M. A. Allesie, N. M. S. de Groot, R. P. M. Houben, U. Schotten, E. Boersma et al., “Electropathological Substrate of Long-Standing Persistent Atrial Fibrillation in Patients with Structural Heart Disease: Longitudinal Dissociation,” *Circulation: Arrhythmia and Electrophysiology*, vol. 3, no. 6, pp. 606–615, 2010.
- [47] H. Tada, K. Tadokoro, S. Ito, S. Naito, T. Hashimoto et al., “Idiopathic Ventricular Arrhythmias Originating From the Tricuspid Annulus: Prevalence, Electrocardiographic Characteristics, and Results of Radiofrequency Catheter Ablation,” *Heart Rhythm*, vol. 4, no. 1, pp. 7–16, 2007.
- [48] B. B. Lerman, “Mechanism of Outflow Tract Tachycardia,” *Heart Rhythm*, vol. 4, no. 7, pp. 973–976, 2007.
- [49] E. M. Aliot, W. G. Stevenson, J. M. Almendral-Garrote, F. Bogun, C. H. Calkins et al., “EHRA/HRS Expert Consensus on Catheter Ablation of Ventricular Arrhythmias,” *Heart Rhythm*, vol. 6, no. 6, pp. 886–933, 2009.
- [50] F. Gaita, C. Giustetto, P. Di Donna, E. Richiardi, L. Libero et al., “Long-Term Follow-Up of Right Ventricular Monomorphic Extrasystoles,” *Journal of the American College of Cardiology*, vol. 38, no. 2, pp. 364–370, 2001.
- [51] J. V. Wylie, T. W. Smith, and M. E. Josephson, “Substrate Mapping for Ablation of Ventricular Tachycardia in Coronary Artery Disease,” in *Cardiac Mapping* (M. Shenasa, G. Hindricks, M. Borggreffe, and G. Breithardt, eds.), ch. 23, pp. 301–309, John Wiley & Sons, Inc., 3 ed., 2009.
- [52] J. Farré, R. H. Anderson, J. A. Cabrera, D. Sánchez-quintana, and J. Benezet-Mazuecos, “Cardiac Anatomy for Catheter Mapping and Ablation of Arrhythmias,” in *Catheter Ablation of Cardiac Arrhythmias* (S. K. S. Huang and M. A. Wood, eds.), ch. 6, pp. 74–102, Elsevier Saunders, 2 ed., 2011.
- [53] R. Arora and A. H. Kadish, “Fundamentals of Intracardiac Mapping,” in *Catheter Ablation of Cardiac Arrhythmias* (S. K. S. Huang and M. A. Wood, eds.), ch. 7, pp. 107–134, Elsevier Saunders, 2 ed., 2011.
- [54] U. B. Tedrow and W. G. Stevenson, “Recording and Interpreting Unipolar Electrograms to Guide Catheter Ablation,” *Heart Rhythm*, vol. 8, no. 5, pp. 791–796, 2011.
- [55] T. Paul, J. P. Moak, C. Morris, and A. Garson, “Epicardial Mapping: How to Measure Local Activation?,” *Pacing and Clinical Electrophysiology : PACE*, vol. 13, no. 3, pp. 285–292, 1990.
- [56] M. S. Spach, W. T. Miller, E. Miller-Jones, R. B. Warren, and R. C. Barr, “Extracellular Potentials Related to Intracellular Action Potentials During Impulse Conduction in Anisotropic Canine Cardiac Muscle,” *Circulation Research*, vol. 45, no. 2, pp. 188–204, 1979.

- [57] L. Eckardt and G. Breithardt, "Construction and Interpretation of Endocardial Maps: From Basic Electrophysiology to 3D Mapping," in *Cardiac Mapping* (M. Shenasa, G. Hindricks, M. Borggrefe, and G. Breithardt, eds.), ch. 2, pp. 13–26, John Wiley & Sons, Inc., 3 ed., 2009.
- [58] R. Deo and R. D. Berger, "The Clinical Utility of Entrainment Pacing," *Journal of Cardiovascular Electrophysiology*, vol. 20, no. 4, pp. 466–470, 2009.
- [59] A. J. Camm, P. Kirchhof, G. Y. H. Lip, U. Schotten, I. Savelieva et al., "Guidelines for the Management of Atrial Fibrillation: The Task Force for the Management of Atrial Fibrillation of the European Society of Cardiology (ESC)," *European Heart Journal*, vol. 31, no. 19, pp. 2369–2429, 2010.
- [60] K. Soejima, "Advanced Catheter Tree-Dimensional Mapping Systems," in *Catheter Ablation of Cardiac Arrhythmias* (S. K. S. Huang and M. A. Wood, eds.), ch. 8, pp. 127–136, Elsevier Saunders, 2 ed., 2011.
- [61] L. Gepstein, G. Hayam, and S. A. Ben-Haim, "A Novel Method for Nonfluoroscopic Catheter-Based Electroanatomical Mapping of the Heart. In Vitro and In Vivo Accuracy Results," *Circulation*, vol. 95, no. 6, pp. 1611–1622, 1997.
- [62] S. A. Ben-Haim, D. Osadchy, I. Scnuster, L. Gepstein, G. Hayam et al., "Non-fluoroscopic, In Vivo Navigation and Mapping Technology," *Nature Medicine*, vol. 2, no. 12, pp. 1393–1395, 1996.
- [63] S. Shpun, L. Gepstein, G. Hayam, and S. A. Ben-Haim, "Guidance of Radiofrequency Endocardial Ablation With Real-time Three-dimensional Magnetic Navigation System," *Circulation*, vol. 96, no. 6, pp. 2016–2021, 1997.
- [64] F. H. Wittkampf, E. F. Wever, R. Derksen, A. A. Wilde, H. Ramanna et al., "LocaLisa: New Technique for Real-Time 3-Dimensional Localization of Regular Intracardiac Electrodes," *Circulation*, vol. 99, no. 10, pp. 1312–7, 1999.
- [65] R. Schilling, N. S. Peters, and D. W. Davies, "Simultaneous Endocardial Mapping in the Human Left Ventricle using a Noncontact Catheter: Comparison of Contact and Reconstructed Electrograms during Sinus Rhythm," *Circulation*, vol. 98, no. 9, pp. 887–898, 1998.
- [66] L. Mantziari, C. Butcher, A. Kontogeorgis, S. Panikker, K. Roy et al., "Utility of a Novel Rapid High-Resolution Mapping System in the Catheter Ablation of Arrhythmias An Initial Human Experience of Mapping the Atria and the Left Ventricle," *JACC: Clinical Electrophysiology*, vol. 1, no. 5, pp. 411–420, 2015.
- [67] L. M. Ptaszek, F. Chalhoub, F. Perna, R. Beinart, C. D. Barrett et al., "Rapid Acquisition of High-Resolution Electroanatomical Maps using a Novel Multielectrode Mapping System," *Journal of Interventional Cardiac Electrophysiology*, vol. 36, no. 3, pp. 233–242, 2013.

- [68] Y. Rudy, C. Ramanathan, and S. Ghosh, “Noninvasive Electrocardiographic Imaging: Methodology and Excitation of the Normal Human Heart,” in *Cardiac Electrophysiology: From Cell to Bedside* (D. P. Zipes and J. Jalife, eds.), ch. 44, pp. 467–472, Saunders Elsevier, 5 ed., 2009.
- [69] D. E. Haines, “Biophysics of Radiofrequency Lesion Formation,” in *Catheter Ablation of Cardiac Arrhythmias* (S. K. S. Huang and M. A. Wood, eds.), ch. 1, pp. 2–19, Elsevier Saunders, 2 ed., 2011.
- [70] E. Buch and K. Shivkumar, “Guiding Lesion Formation during Radiofrequency Energy Catheter Ablation,” in *Catheter Ablation of Cardiac Arrhythmias* (S. K. S. Huang and M. A. Wood, eds.), ch. 2, pp. 20–31, Elsevier Saunders, 2 ed., 2011.
- [71] T. Taneja, K.-H. Lin, and S. K. S. Huang, “Irrigated and Cooled-Tip Radiofrequency Catheter Ablation,” in *Catheter Ablation of Cardiac Arrhythmias* (S. K. S. Huang and M. A. Wood, eds.), ch. 3, pp. 32–42, Elsevier Saunders, 2 ed., 2011.
- [72] A. Alcaine, D. Soto-Iglesias, D. Andreu, J. Fernández-Armenta, A. Berruezo et al., “Wavelet-Based Electrogram Onset Identification for Ventricular Electroanatomical Mapping,” in *Proc. Computing in Cardiology*, vol. 40, (Zaragoza, Spain), pp. 615–618, 2013.
- [73] A. Alcaine, D. Soto-Iglesias, M. Calvo, E. Guiu, D. Andreu et al., “A Wavelet-Based Electrogram Onset Delineator for Automatic Ventricular Activation Mapping,” *IEEE Transactions on Biomedical Engineering*, vol. 61, no. 12, pp. 2830–2839, 2014.
- [74] A. Alcaine, D. Soto-Iglesias, M. Calvo, E. Guiu, D. Andreu et al., “Evaluation of an Automatic Delineation Algorithm for Activation Mapping of Focal Ventricular Tachycardias,” in *European Heart Journal*, vol. 35 (Sup.1), (Barcelona, Spain), p. 598 (P3357), 2014.
- [75] A. Alcaine, D. Soto-Iglesias, D. Andreu, J. Acosta, A. Berruezo et al., “A Morphology-Based Spatial Consistency Algorithm to Improve EGM Delineation in Ventricular Electroanatomical Mapping,” in *Proc. Computing in Cardiology*, vol. 41, (Cambridge, MA (USA)), pp. 125–128, 2014.
- [76] A. Alcaine, N. M. S. de Groot, P. Laguna, J. P. Martínez, and R. P. M. Houben, “Estimation of High-Density Activation Maps During Atrial Fibrillation,” in *Proc. Computing in Cardiology*, vol. 42, (Nice, France), pp. 825–828, 2015.
- [77] A. Alcaine, N. M. S. de Groot, P. Laguna, J. P. Martínez, and R. P. M. Houben, “Spatiotemporal Model-Based Estimation of High-Density Atrial Fibrillation Activation Maps,” *Digital Signal Processing*, vol. 54, pp. 64–74, 2016.

- [78] A. Alcaine, M. Masè, A. Cristoforetti, F. Ravelli, G. Nollo et al., “A Multi-Variate Predictability Framework to Assess Invasive Cardiac Activity and Interactions during Atrial Fibrillation,” *IEEE Transactions on Biomedical Engineering*, DOI: 10.1109/TBME.2016.2592953, 2016.
- [79] V. Y. Reddy, “Mapping and Imaging,” in *Cardiac Electrophysiology: From Cell to Bedside* (D. P. Zipes and J. Jalife, eds.), ch. 60, pp. 581–593, Saunders Elsevier, 6 ed., 2014.
- [80] C. Weiss, S. Willems, R. Rueppel, M. Hoffmann, and T. Meinertz, “Electroanatomical Mapping (CARTO) of Ectopic Atrial Tachycardia: Impact of Bipolar and Unipolar Local Electrogram Annotation for Localization the Focal Origin,” *Journal of Interventional Cardiac Electrophysiology*, vol. 5, no. 1, pp. 101–107, 2001.
- [81] M. El Haddad, R. P. M. Houben, R. Stroobandt, F. Van Heuverswyn, R. Tavernier et al., “Algorithmic Detection of the Beginning and End of Bipolar Electrograms: Implications for Novel Methods to Assess Local Activation Time During Atrial Tachycardia,” *Biomedical Signal Processing and Control*, vol. 8, no. 6, pp. 981–991, 2013.
- [82] M. El Haddad, R. P. M. Houben, R. Stroobandt, F. Van Heuverswyn, R. Tavernier et al., “Novel Algorithmic Methods in Mapping of Atrial and Ventricular Tachycardia,” *Circulation. Arrhythmia and Electrophysiology*, vol. 7, no. 3, pp. 463–472, 2014.
- [83] T. G. Oesterlein, M. W. Keller, S. Schuler, A. Luik, M. Krüger et al., “Determination of Local Activation Time in Bipolar Endocardial Electrograms: A Comparison of Clinical Criteria and a New Method Based on the Non-Linear Energy Operator,” *Journal of Electrocardiology*, vol. 46, no. 4, p. e18, 2013.
- [84] J. M. Hsing, P. Zei, H. H. Hsia, P. J. Wang, and A. Al-Ahmad, “Challenges and Limitations of Electroanatomical Mapping Technologies,” in *Cardiac Mapping* (M. Shenasa, G. Hindricks, M. Borggrefe, and G. Breithardt, eds.), ch. 10, pp. 117–126, John Wiley & Sons, Inc., 3 ed., 2009.
- [85] J. L. Wells, R. B. Karp, N. T. Kouchoukos, W. A. MacLean, T. N. James et al., “Characterization of Atrial Fibrillation in Man: Studies Following Open Heart Surgery,” *Pacing and Clinical Electrophysiology : PACE*, vol. 1, no. 4, pp. 426–438, 1978.
- [86] K. T. Konings, J. L. R. M. Smeets, O. C. Penn, H. J. Wellens, and M. A. Allesie, “Configuration of Unipolar Atrial Electrograms During Electrically Induced Atrial Fibrillation in Humans,” *Circulation*, vol. 95, no. 5, pp. 1231–1241, 1997.
- [87] J. G. Proakis, *Digital Communications*. Prentice-Hall, 4 ed., 2000.
- [88] S. Mallat, *A Wavelet Tour of Signal Processing*. Academic Press, 2 ed., 1999.

- [89] S. Mallat and S. Zhong, "Characterization of Signals From Multiscale Edges," *IEEE Transactions on Pattern Analysis and Machine Intelligence*, vol. 14, no. 7, pp. 710–732, 1992.
- [90] A. Cohen and J. Kovačević, "Wavelets: The Mathematical Background," in *Proceedings of the IEEE*, vol. 84, pp. 514–522, 1996.
- [91] J. P. Martínez, R. Almeida, S. Olmos, A. P. Rocha, and P. Laguna, "A Wavelet-Based ECG Delineator: Evaluation on Standard Databases," *IEEE Transactions on Biomedical Engineering*, vol. 51, no. 4, pp. 570–581, 2004.
- [92] M. Akay, *Detection and Estimation Methods for Biomedical Signals*. Academic Press, 1996.
- [93] P. Laguna, R. Jané, and P. Caminal, "Automatic Detection of Wave Boundaries in Multilead ECG Signals: Validation With the CSE Database," *Computers and Biomedical Research*, vol. 27, no. 1, pp. 45–60, 1994.
- [94] C. Li, C. Zheng, and C. Tai, "Detection of ECG Characteristic Points Using Wavelet Transforms," *IEEE Transactions on Biomedical Engineering*, vol. 42, no. 1, pp. 21–28, 1995.
- [95] L. Lin, A. S. Hedayat, B. Sinha, and M. Yang, "Statistical Methods in Assessing Agreement: Models, Issues, and Tools," *Journal of the American Statistical Association*, vol. 97, no. 457, pp. 257–270, 2002.
- [96] D. G. Altman and J. M. Bland, "Measurement in Medicine: the Analysis of Method Comparison Studies," *The statistician*, vol. 32, pp. 307–317, 1983.
- [97] C. Movsowitz, D. Schwartzman, D. J. Callans, M. Preminger, E. Zado et al., "Idiopathic Right Ventricular Outflow Tract Tachycardia: Narrowing the Anatomic Location for Successful Ablation," *American Heart Journal*, vol. 131, no. 5, pp. 930–936, 1996.
- [98] B. B. Lerman, K. M. Stein, and S. M. Markowitz, "Mechanisms of Idiopathic Left Ventricular Tachycardia," *Journal of Cardiovascular Electrophysiology*, vol. 8, no. 5, pp. 571–583, 1997.
- [99] C. Herczku, A. Berruezo, D. Andreu, J. Fernández-Armenta, L. Mont, "Mapping Data Predictors of a Left Ventricular Outflow Tract Origin of Idiopathic Ventricular Tachycardia With V3 Transition and Septal Earliest Activation," *Circulation: Arrhythmia and Electrophysiology*, vol. 5, no. 3, pp. 484–491, 2012.
- [100] B. B. Lerman, "Outflow Tract Ventricular Arrhythmias: An Update," *Trends in Cardiovascular Medicine*, vol. 25, no. 6, pp. 550–558, 2015.
- [101] S. J. Asirvatham, "Correlative Anatomy for the Invasive Electrophysiologist: Outflow Tract and Supravalvar Arrhythmia," *Journal of Cardiovascular Electrophysiology*, vol. 20, no. 8, pp. 955–968, 2009.

- [102] E. N. Prystowsky, B. J. Padanilam, S. Joshi, and R. I. Fogel, "Ventricular Arrhythmias in the Absence of Structural Heart Disease," *Journal of the American College of Cardiology*, vol. 59, no. 20, pp. 1733–1744, 2012.
- [103] J. Acosta, D. Penela, C. Herczku, Y. Macías, D. Andreu et al., "Impact of Earliest Activation Site Location in the Septal Right Ventricular Outflow Tract for Identification of Left vs Right Outflow Tract Origin of Idiopathic Ventricular Arrhythmias," *Heart Rhythm*, vol. 12, no. 4, pp. 726–734, 2015.
- [104] T. Lewis, "Auricular Fibrillation: A Common Clinical Condition," *British Medical Journal*, vol. 2, p. 1528, 1909.
- [105] C. H. Calkins, K. H. Kuck, R. Cappato, J. Brugada, A. J. Camm et al., "2012 HRS/EHRA/ECAS Expert Consensus Statement on Catheter and Surgical Ablation of Atrial Fibrillation: Recommendations for Patient Selection, Procedural Techniques, Patient Management and Follow-Up, Definitions, Endpoints, and Research Trial Design," *Journal of Interventional Cardiac Electrophysiology*, vol. 33, no. 2, pp. 171–257, 2012.
- [106] F. Morady and D. P. Zipes, "Atrial Fibrillation: Clinical Features, Mechanisms, and Management," in *Brainwald's Heart Disease: A Textbook of Cardiovascular Medicine* (R. O. Bonow, D. L. Mann, D. P. Zipes, and P. Libby, eds.), ch. 40, pp. 825–844, Elsevier Saunders, 9 ed., 2012.
- [107] V. E. Hagens, A. V. Ranchor, E. Van Sonderen, H. A. Bosker, O. Kamp et al., "Effect of Rate or Rhythm Control on Quality of Life in Persistent Atrial Fibrillation. Results From the Rate Control Versus Electrical Cardioversion (RACE) Study," *Journal of the American College of Cardiology*, vol. 43, no. 2, pp. 241–247, 2004.
- [108] G. Thrall, D. Lane, D. Carroll, and G. Y. H. Lip, "Quality of Life in Patients With Atrial Fibrillation: A Systematic Review," *The American Journal of Medicine*, vol. 119, no. 5, pp. 448.e1–e19, 2006.
- [109] G. Boriani, "The Epidemiologic Threat of Atrial Fibrillation: Need for Secondary, Primary, and Primordial Prevention," *CHEST Journal*, vol. 147, no. 1, pp. 109–119, 2015.
- [110] A. Yaksh, C. Kik, P. Knops, J. W. Roos-Hesselink, A. J. J. C. Bogers et al., "Atrial Fibrillation: To Map or Not to Map?," *Netherlands Heart Journal*, vol. 22, no. 6, pp. 259–266, 2014.
- [111] M. A. Allesie and N. M. S. de Groot, "CrossTalk Opposing View: Rotors Have Not Been Demonstrated to be the Drivers of Atrial Fibrillation," *The Journal of Physiology*, vol. 592, no. 15, pp. 3167–3170, 2014.
- [112] A. van Oosterom, "Solidifying the Solid Angle," *Journal of Electrocardiology*, vol. 35 Suppl, no. 4, Part B, pp. 181–192, 2002.

- [113] D. Harrild and C. Henriquez, "A Computer Model of Normal Conduction in the Human Atria.," *Circulation Research*, vol. 87, no. 7, pp. E25–E36, 2000.
- [114] R. P. M. Houben, N. M. S. de Groot, J. L. R. M. Smeets, A. E. Becker, F. W. Lindemans et al., "S-wave Predominance of Epicardial Electrograms During Atrial Fibrillation in Humans: Indirect Evidence for a Role of the Thin Subepicardial Layer," *Heart Rhythm*, vol. 1, no. 6, pp. 639–647, 2004.
- [115] A. van Oosterom and J. Strackee, "The Solid Angle of a Plane Triangle," *IEEE Transactions on Biomedical Engineering*, vol. BME-30, no. 2, pp. 125–126, 1983.
- [116] P. V. Bayly, B. H. KenKnight, J. M. Rogers, R. E. Hillsley, R. E. Ideker et al., "Estimation of Conduction Velocity Vector Fields From Epicardial Mapping Data," *IEEE Transactions on Biomedical Engineering*, vol. 45, no. 5, pp. 563–571, 1998.
- [117] T. N. Fitzgerald, E. K. Rhee, D. H. Brooks, and J. K. Triedman, "Estimation of Cardiac Conduction Velocities Using Small Data Sets," *Annals of Biomedical Engineering*, vol. 31, no. 3, pp. 250–261, 2003.
- [118] N. Mazeh, D. E. Haines, M. W. Kay, and B. J. Roth, "A Simplified Approach for Simultaneous Measurements of Wavefront Velocity and Curvature in the Heart Using Activation Times," *Cardiovascular Engineering and Technology*, vol. 4, no. 4, pp. 520–534, 2013.
- [119] R. P. M. Houben, N. M. S. de Groot, and M. A. Allesie, "Analysis of Fractionated Atrial Fibrillation Electrograms by Wavelet Decomposition," *IEEE Transactions on Biomedical Engineering*, vol. 57, no. 6, pp. 1388–1398, 2010.
- [120] P. Kuklik, D. H. Lau, A. N. Ganesan, A. G. Brooks, and P. Sanders, "High-Density Mapping of Atrial Fibrillation in a Chronic Substrate: Evidence for Distinct Modes of Repetitive Wavefront Propagation," *International Journal of Cardiology*, vol. 199, pp. 407–414, 2015.
- [121] O. Dössel, M. W. Krueger, F. M. Weber, M. Wilhelms, and G. Seemann, "Computational Modeling of the Human Atrial Anatomy and Electrophysiology," *Medical & Biological Engineering & Computing*, vol. 50, no. 8, pp. 773–799, 2012.
- [122] K. Nademanee, J. McKenzie, E. Kosar, M. Schwab, B. Sunsaneewitayakul et al., "A New Approach for Catheter Ablation of Atrial Fibrillation: Mapping of the Electrophysiologic Substrate," *Journal of the American College of Cardiology*, vol. 43, no. 11, pp. 2044–2053, 2004.
- [123] K. Nademanee, E. Lockwood, N. Oketani, and B. Gidney, "Catheter Ablation of Atrial Fibrillation Guided by Complex Fractionated Atrial Electrogram Mapping of Atrial Fibrillation Substrate," *Journal of Cardiology*, vol. 55, no. 1, pp. 1–12, 2010.

- [124] F. Ravelli and M. Masè, “Computational Mapping in Atrial Fibrillation: How the Integration of Signal-Derived Maps may Guide the Localization of Critical Sources,” *Europace*, vol. 16, pp. 714–723, may 2014.
- [125] M. Baumert, P. Sanders, and A. Ganesan, “Quantitative-Electrogram-Based Methods for Guiding Catheter Ablation in Atrial Fibrillation,” *Proceedings of the IEEE*, vol. 104, no. 2, pp. 416–431, 2016.
- [126] J. G. Quintanilla, J. Pérez-Villacastín, N. Pérez-Castellano, S. V. Pandit, O. Berenfeld et al., “Mechanistic approaches to detect, target, and ablate the drivers of atrial fibrillation,” *Circulation. Arrhythmia and Electrophysiology*, vol. 9, no. 1, p. e002481, 2016.
- [127] V. Barbaro, P. Bartolini, G. Calcagnini, F. Censi, and A. Michelucci, “Measure of Synchronisation of Right Atrial Depolarisation Wavefronts During Atrial Fibrillation,” *Medical & Biological Engineering & Computing*, vol. 40, no. 1, pp. 56–62, 2002.
- [128] R. P. M. Houben, N. M. S. de Groot, F. W. Lindemans, and M. A. Allessie, “Automatic Mapping of Human Atrial Fibrillation by Template Matching,” *Heart Rhythm*, vol. 3, no. 10, pp. 1221–1228, 2006.
- [129] A. Alcaine, F. Simón, A. Arenal, P. Laguna, and J. P. Martínez, “A Wavelet-Based Activation Detector for Bipolar Electrogram Analysis During Atrial Fibrillation,” in *Proc. Computing in Cardiology*, vol. 39, (Krakow, Poland), pp. 717–720, 2012.
- [130] S. Lee, K. Ryu, A. L. Waldo, C. M. Khrestian, D. M. Durand et al., “An Algorithm to Measure Beat-to-Beat Cycle Lengths for Assessment of Atrial Electrogram Rate and Regularity During Atrial Fibrillation,” *Journal of Cardiovascular Electrophysiology*, vol. 24, no. 2, pp. 199–206, 2013.
- [131] J. Ng, V. Sehgal, J. K. Ng, D. Gordon, and J. J. Goldberger, “Iterative Method to Detect Atrial Activations and Measure Cycle Length From Electrograms During Atrial Fibrillation,” *IEEE Transactions on Biomedical Engineering*, vol. 61, no. 2, pp. 273–278, 2014.
- [132] P. Sanders, O. Berenfeld, M. Hocini, P. Jaïs, R. Vaidyanathan et al., “Spectral Analysis Identifies Sites of High-Frequency Activity Maintaining Atrial Fibrillation in Humans,” *Circulation*, vol. 112, no. 6, pp. 789–797, 2005.
- [133] Y.-J. Lin, C.-T. Tai, T. Kao, H.-W. Tso, S. Higa et al., “Frequency Analysis in Different Types of Paroxysmal Atrial Fibrillation,” *Journal of the American College of Cardiology*, vol. 47, no. 7, pp. 1401–1407, 2006.
- [134] J. Ng, A. H. Kadish, and J. J. Goldberger, “Effect of Electrogram Characteristics on the Relationship of Dominant Frequency to Atrial Activation Rate in Atrial Fibrillation,” *Heart Rhythm*, vol. 3, no. 11, pp. 1295–1305, 2006.

- [135] J. Ng and J. J. Goldberger, "Understanding and Interpreting Dominant Frequency Analysis of AF Electrograms," *Journal of Cardiovascular Electrophysiology*, vol. 18, no. 6, pp. 680–685, 2007.
- [136] G. W. Botteron and J. M. Smith, "A Technique for Measurement of the Extent of Spatial Organization of Atrial Activation During Atrial Fibrillation in the Intact Human Heart," *IEEE Transactions on Biomedical Engineering*, vol. 42, no. 6, pp. 579–586, 1995.
- [137] T. H. Everett, L. C. Kok, R. H. Vaughn, J. R. Moorman, and D. E. Haines, "Frequency Domain Algorithm for Quantifying Atrial Fibrillation Organization to Increase Defibrillation Efficacy," *IEEE Transactions on Biomedical Engineering*, vol. 48, no. 9, pp. 969–978, 2001.
- [138] L. Faes, G. Nollo, R. Antolini, F. Gaita, and F. Ravelli, "A Method for Quantifying Atrial Fibrillation Organization Based on Wave-Morphology Similarity," *IEEE Transactions on Biomedical Engineering*, vol. 49, no. 12, pp. 1504–1513, 2002.
- [139] U. Richter, A. Bollmann, D. Husser, and M. Stridh, "Right Atrial Organization and Wavefront Analysis in Atrial Fibrillation," *Medical & Biological Engineering & Computing*, vol. 47, no. 12, pp. 1237–1246, 2009.
- [140] Ó. Barquero-Pérez, J. L. Rojo-Álvarez, A. J. Caamaño, R. Goya-Esteban, E. Everss et al., "Fundamental frequency and regularity of cardiac electrograms with Fourier organization analysis," *IEEE Transactions on Biomedical Engineering*, vol. 57, no. 9, pp. 2168–2177, 2010.
- [141] F. Ravelli, M. Masè, A. Cristoforetti, M. Marini, and M. Disertori, "The Logical Operator Map Identifies Novel Candidate Markers for Critical Sites in Patients with Atrial Fibrillation," *Progress in Biophysics and Molecular Biology*, vol. 115, no. 2-3, pp. 186–197, 2014.
- [142] D. Scherr, D. Dalal, A. Cheema, A. Cheng, C. A. Henrikson et al., "Automated Detection and Characterization of Complex Fractionated Atrial Electrograms in Human Left Atrium During Atrial Fibrillation," *Heart Rhythm*, vol. 4, no. 8, pp. 1013–1020, 2007.
- [143] A. Verma, P. Novak, L. Macle, B. Whaley, M. Beardsall et al., "A Prospective, Multicenter Evaluation of Ablating Complex Fractionated Electrograms (CFEs) During Atrial Fibrillation (AF) Identified by an Automated Mapping Algorithm: Acute Effects on AF and Efficacy as an Adjuvant Strategy," *Heart Rhythm*, vol. 5, no. 2, pp. 198–205, 2008.
- [144] G. Monir and S. J. Pollak, "Consistency of the CFAE Phenomena Using Custom Software for Automated Detection of Complex Fractionated Atrial Electrograms (CFAEs) in the Left Atrium During Atrial Fibrillation," *Journal of Cardiovascular Electrophysiology*, vol. 19, no. 9, pp. 915–919, 2008.

- [145] R. A. Gray, A. M. Pertsov, and J. Jalife, "Spatial and Temporal Organization During Cardiac Fibrillation," *Nature*, vol. 392, no. 6671, pp. 75–78, 1998.
- [146] S. M. Narayan, D. E. Krummen, M. W. Enyeart, and W. J. Rappel, "Computational Mapping Identifies Localized Mechanisms for Ablation of Atrial Fibrillation," *PLoS ONE*, vol. 7, no. 9, p. e46034, 2012.
- [147] P. Kuklik, S. Zeemering, B. Maesen, J. Maessen, H. J. G. M. Crijns et al., "Reconstruction of Instantaneous Phase of Unipolar Atrial Contact Electrogram Using a Concept of Sinusoidal Recomposition and Hilbert Transform," *IEEE Transactions on Biomedical Engineering*, vol. 62, no. 1, pp. 296–302, 2015.
- [148] U. Richter, L. Faes, A. Cristoforetti, M. Masè, F. Ravelli et al., "A Novel Approach to Propagation Pattern Analysis in Intracardiac Atrial Fibrillation Signals," *Annals of Biomedical Engineering*, vol. 39, no. 1, pp. 310–323, 2011.
- [149] U. Richter, L. Faes, F. Ravelli, and L. Sörnmo, "Propagation Pattern Analysis During Atrial Fibrillation Based on Sparse Modeling," *IEEE Transactions on Biomedical Engineering*, vol. 59, no. 5, pp. 1319–1328, 2012.
- [150] M. Rodrigo, A. Liberos, M. S. Guillem, J. Millet, and A. M. Climent, "Causality Relation Map: A Novel Methodology for the Identification of Hierarchical Fibrillatory Processes," in *Proc. Computing in Cardiology*, vol. 38, (Hangzhou, China), pp. 173–176, 2011.
- [151] M. Rodrigo, M. S. Guillem, A. Liberos, J. Millet, O. Berenfeld et al., "Identification of Fibrillatory Sources by Measuring Causal Relationships," in *Proc. Computing in Cardiology*, vol. 39, (Krakow, Poland), pp. 705–708, 2012.
- [152] M. Rodrigo, A. Liberos, A. M. Climent, and M. S. Guillem, "Identification of Ablation Sites in Atrial Flutter by Causal Method," in *Proc. Computing in Cardiology*, vol. 40, (Zaragoza, Spain), pp. 707–710, 2013.
- [153] M. Rodrigo, A. M. Climent, A. Liberos, D. Calvo, F. Fernández-Avilés et al., "Identification of Dominant Excitation Patterns and Sources of Atrial Fibrillation by Causality Analysis," *Annals of Biomedical Engineering*, vol. 44, no. 8, pp. 2364–2376, 2016.
- [154] H. Lütkepohl, *New Introduction to Multiple Time Series Analysis*. Berlin, Heidelberg: Springer Berlin Heidelberg, 2005.
- [155] G. Schwarz, "Estimating the Dimension of a Model," *The Annals of Statistics*, vol. 6, no. 2, pp. 461–464, 1978.
- [156] L. Barnett and A. K. Seth, "The MVGC Multivariate Granger Causality Toolbox: A New Approach to Granger-Causal Inference," *Journal of Neuroscience Methods*, vol. 223, pp. 50–68, 2014.
- [157] C. W. J. Granger, "Investigating Causal Relations by Econometric Models and Cross-Spectral Methods," *Econometrica*, vol. 37, no. 3, pp. 424–438, 1969.

- [158] L. Faes, D. Kugiumtzis, G. Nollo, F. Jurysta, and D. Marinazzo, “Estimating the Decomposition of Predictive Information in Multivariate Systems,” *Physical Review. E*, vol. 91, no. 3, pp. 032904–1 – 032904–16, 2015.
- [159] D. Chicharro, “On the Spectral Formulation of Granger Causality,” *Biological Cybernetics*, vol. 105, no. 5-6, pp. 331–347, 2011.
- [160] A. Porta and L. Faes, “Wiener-Granger Causality in Network Physiology With Applications to Cardiovascular Control and Neuroscience,” *Proceedings of the IEEE*, vol. 104, no. 2, pp. 282–309, 2016.
- [161] L. Faes, D. Marinazzo, S. Stramaglia, F. Jurysta, A. Porta et al., “Predictability Decomposition Detects the Impairment of Brain-Heart Dynamical Networks During Sleep Disorders and Their Recovery with Treatment,” *Philosophical transactions. Series A, Mathematical, physical, and engineering sciences*, vol. 374, no. 2067, 2016.
- [162] L. Faes, A. Porta, and G. Nollo, “Information Decomposition in Bivariate Systems: Theory and Application to Cardiorespiratory Dynamics,” *Entropy*, vol. 17, no. 1, pp. 277–303, 2015.
- [163] A. K. Seth, “Measuring Autonomy and Emergence via Granger Causality,” *Artificial Life*, vol. 16, no. 2, pp. 179–196, 2010.
- [164] M. Courtemanche, R. J. Ramírez, and S. Nattel, “Ionic Mechanisms Underlying Human Atrial Action Potential Properties: Insights From a Mathematical Model,” *American Journal of Physiology - Heart and Circulatory Physiology*, vol. 275, pp. H301–H321, jul 1998.
- [165] V. Jacquemet, N. Virag, Z. Ihara, L. Dang, O. Blanc et al., “Study of Unipolar Electrogram Morphology in a Computer Model of Atrial Fibrillation,” *Journal of Cardiovascular Electrophysiology*, vol. 14, no. s10, pp. S172–S179, 2003.
- [166] M. Courtemanche, R. J. Ramírez, and S. Nattel, “Ionic Targets for Drug Therapy and Atrial Fibrillation-Induced Electrical Remodeling: Insights From a Mathematical Model,” *Cardiovascular Research*, vol. 42, no. 2, pp. 477–489, 1999.
- [167] A. Cristoforetti, M. Masè, and F. Ravelli, “A Fully Adaptive Multiresolution Algorithm for Atrial Arrhythmia Simulation on Anatomically Realistic Unstructured Meshes,” *IEEE Transactions on Biomedical Engineering*, vol. 60, no. 9, pp. 2585–2593, 2013.
- [168] V. Jacquemet and C. S. Henriquez, “Finite Volume Stiffness Matrix for Solving Anisotropic Cardiac Propagation in 2-D and 3-D Unstructured Meshes,” *IEEE Transactions on Biomedical Engineering*, vol. 52, no. 8, pp. 1490–1492, 2005.

- [169] F. Ravelli, L. Faes, L. Sandrini, F. Gaita, R. Antolini et al., “Wave Similarity Mapping Shows the Spatiotemporal Distribution of Fibrillatory Wave Complexity in the Human Right Atrium During Paroxysmal and Chronic Atrial Fibrillation,” *Journal of Cardiovascular Electrophysiology*, vol. 16, no. 10, pp. 1071–1076, 2005.
- [170] B. P. Hoekstra, C. G. Diks, M. A. Allesie, and J. DeGoede, “Non-Linear Time Series Analysis: Methods and Applications to Atrial Fibrillation,” *Annali dell’Istituto superiore di sanita*, vol. 37, no. 3, pp. 325–333, 2001.
- [171] S. Massé, K. Magtibay, N. Jackson, J. Asta, M. Kusha et al., “Resolving Myocardial Activation With Novel Omnipolar Electrograms,” *Circulation: Arrhythmia and Electrophysiology*, vol. 9, p. e004107, jul 2016.
- [172] D. C. Deno, R. Balachandran, D. Morgan, F. Ahmad, S. Massé et al., “Orientation Independent Catheter-Based Characterization of Myocardial Activation,” *IEEE Transactions on Biomedical Engineering*, DOI: 10.1109/TBME.2016.2589158, 2016.



List of Publications

Publications in Journal Articles

- **A. Alcaine**, D. Soto-Iglesias, M. Calvo, E. Guiu, D. Andreu, J. Fernández-Armenta, A. Berruezo, P. Laguna, O. Camara and J. P. Martínez, “*A Wavelet-Based Electrogram Onset Delineator for Automatic Ventricular Activation Mapping*,” IEEE Transactions on Biomedical Engineering, vol. 61(12), pp. 2830–2839, 2014.
- **A. Alcaine**, N. M. S. de Groot, P. Laguna, J. P. Martínez and R. P. M. Houben, “*Spatiotemporal Model-Based Estimation of High-Density Atrial Fibrillation Activation Maps*,” Digital Signal Processing, vol. 54, pp. 64–74, 2016.
- **A. Alcaine**, M. Masè, A. Cristoforetti, F. Ravelli, G. Nollo, P. Laguna, J. P. Martínez and L. Faes . “*A Multi-Variate Predictability Framework to Assess Invasive Cardiac Activity and Interactions during Atrial Fibrillation*,” IEEE Transactions on Biomedical Engineering, DOI: 10.1109/TBME.2016.2592953, 2016.
- **A. Alcaine**, D. Soto-Iglesias, J. Acosta, V. Korshunov, D. Penela, D. Andreu, J. Fernández-Armenta, P. Laguna, J. P. Martínez, O. Camara, and A. Berruezo. “*Automatic Activation Mapping and Origin Identification of Idiopathic Outflow Tract Ventricular Arrhythmias*,” Circulation: Arrhythmia and Electrophysiology, 2016. (Submitted).

Publications in Conferences Proceedings and Abstracts

- **A. Alcaine**, F. Simón, Á. Arenal, P. Laguna and J. P. Martínez, “*A Wavelet-Based Activation Detector for Bipolar Electrogram Analysis During Atrial Fibrillation*,” Proc. of the XXXIX International Conference on Computing in Cardiology. Krakow, Poland, pp. 717–720, 2012.
- **A. Alcaine**, D. Soto-Iglesias, D. Andreu, J. Fernández-Armenta, A. Berruezo, P. Laguna, O. Camara and J. P. Martínez, “*Wavelet-Based Electrogram Onset Identification for Ventricular Electroanatomical Mapping*,” Proc. of the XL

International Conference on Computing in Cardiology. Zaragoza, Spain, pp. 615–618, 2013.

- **A. Alcaine**, Á. Arenal, P. Laguna and J. P. Martínez, “*Study of Electrogram Organization and Synchronization in Paroxysmal and Persistent/Permanent Atrial Fibrillation*,” Proc. of the 8th Conference of the European Study Group on Cardiovascular Oscillations (ESGCO), Trento, Italy, pp. 93–94, 2014.
- **A. Alcaine**, D. Soto-Iglesias, M. Calvo, E. Guiu, D. Andreu, J. Fernández-Armenta, P. Laguna, O. Camara, J. P. Martínez and A. Berruezo, “*Evaluation of an Automatic Delineation Algorithm for Activation Mapping of Focal Ventricular Tachycardias*,” European Heart Journal, vol. 35 (suppl. 1: Abstracts of the ESC Congress 2014, Barcelona, Spain), 598, P3357, 2014.
- **A. Alcaine**, D. Soto-Iglesias, D. Andreu, J. Acosta, A. Berruezo, P. Laguna, O. Camara and J. P. Martínez, “*A Morphology-Based Spatial Consistency Algorithm to Improve EGM Delineation in Ventricular Electroanatomical Mapping*,” Proc. of the XLI International Conference on Computing in Cardiology. Cambridge, MA, USA, pp. 125–128, 2014.
- **A. Alcaine**, N. M. S. de Groot, P. Laguna, J. P. Martínez and R. P. M. Houben, “*A High-Density Activation Map Estimation During Atrial Fibrillation*,” Proc. of the XLII International Conference on Computing in Cardiology. Nize, France, pp. 825–829, 2015.

Ongoing Research Derived From the Thesis

- **A. Alcaine**, D. Soto-Iglesias, J. Acosta, D. Penela, D. Andreu, J. Fernández-Armenta, P. Laguna, O. Camara, J. P. Martínez and A. Berruezo. “*Automatic Conducting Channel Delineation in Post-Myocardial Infarction Patients with Scar-related Ventricular Tachycardia*,” 2017. (In preparation)

Patent Applications Derived From the Thesis

- **Alejandro Alcaine**, Antonio Berruezo, Oscar Camara, Pablo Laguna, Juan Pablo Martínez, David Soto-Iglesias, “*A computer implemented method to identify the ventricular arrhythmogenic substrate in myocardial scar or fibrotic tissue and computer programs thereof*,” Application number: EP16002222, 2016.

Publications Not Related With the Thesis

- J. Lázaro, **A. Alcaine**, D. Romero, E. Gil, P. Laguna, E. Pueyo and R. Bailón, “*Electrocardiogram Derived Respiratory Rate from QRS Slopes and R-Wave An-*

gle,” *Annals of Biomedical Engineering*, vol. 42 (10), pp. 2072–2083, 2014.

- **A. Alcaine**, R. Bailón, D. Romero, E. Pueyo and P. Laguna “*Very-Low-Frequency Modulation of QRS Slopes in Patients with Angina Pectoris*,” Proc. of the XXXVIII International Conference on Computing in Cardiology. Hangzhou, China, pp. 757–760, 2011.
- J. Lázaro, **A. Alcaine**, E. Gil, P. Laguna and R. Bailón, “*Electrocardiogram Derived Respiration from QRS Slopes*,” Proc. of the 35th Annual International Conference of the IEEE EMBS. Osaka, Japan, pp. 3913–3916, 2013.
- D. Hernando, **A. Alcaine**, P. Laguna, E. Pueyo and R. Bailón, “*Very Low Frequency Modulation in QRS Slopes and its Relation with Respiration and Heart Rate Variability During Hemodialysis*,” Proc. of the 35th Annual International Conference of the IEEE EMBS. Osaka, Japan, pp. 5365–5368, 2013.
- J. Lázaro, **A. Alcaine**, D. Romero, E. Gil, P. Laguna, L. Sörnmo and R. Bailón, “*Electrocardiogram Derived Respiration from QRS Slopes: Evaluation with Stress Testing Recordings*,” Proc. of the XL International Conference on Computing in Cardiology. Zaragoza, Spain, pp. 655–658, 2013.
- D. Hernando, **A. Alcaine**, E. Pueyo, P. Laguna, M. Orini, A. Arcentales, B. Giraldo, A. Voss, A. Bayés-Genís and R. Bailón, “*Influence of Respiration in the Very Low Frequency Modulation of QRS slopes and Heart Rate Variability in Cardiomyopathy Patients*,” Proc. of the XL International Conference on Computing in Cardiology. Zaragoza, Spain, pp. 117-120, 2013.

